Graduate Theses and Dissertations   Graduate School

April 2020

Laser Micropatterning Effects on Corrosion Resistance of Pure Magnesium Surfaces

Yahya Efe Yayoglu
University of South Florida

Laser Micropatterning Effects on

Corrosion Resistance of Pure Magnesium Surfaces

by

Yahya Efe Yayoglu

A dissertation submitted in partial fulfillment
of the requirements for the degree of
Doctor of Philosophy in Mechanical Engineering
Department of Mechanical Engineering
College of Engineering
University of South Florida

Co-Major Professor: Nathan B. Crane, Ph.D.
Co-Major Professor: Nathan D. Gallant, Ph.D.
Ryan Toomey, Ph.D.
Alberto A. Sagüés, Ph.D.
Matthias Batzill, Ph.D.

Date of Approval:
October 19, 2019

Keywords: degradation, medical, implant, micromachining,
ablation, wetting, picosecond, EIS, electrochemical

Acknowledgments

Table of Contents

List of Tables

List of Figures

Abstract

Magnesium and its alloys are good candidates to manufacture medical implants. They have excellent biocompatibility and because they biodegrade secondary surgical operation to remove the implant could be eliminated. However, in aqueous environments, magnesium alloys rapidly corrode, resulting in premature degradation of the implant along with biologically intolerable hydrogen gas generation. In literature, there are multiple studies focused on creating water repelling hydrophobic magnesium surfaces in order to decrease corrosion rates. Hydrophobic properties can be achieved by creation of a roughness profile on an initially smooth surface combined with a treatment that reduces the free surface energy. In theory, hydrophobic surfaces yield an undisturbed gas layer over the surface which acts as a protective barrier against corrosion in submerged conditions. However, studies in literature have not investigated the mechanism behind increased corrosion protection that comes with hydrophobic surfaces nor the influence of series of processes used to create hydrophobic surfaces on corrosion behavior. In this study, pillar shaped microstructure patterns were fabricated on smooth pure magnesium surfaces by picosecond laser ablation. Some micropatterned samples were further processed by stearic acid modification (SAM). Micropatterned surfaces with SAM had hydrophobic properties with water droplet contact angles higher than 130°, while the micropatterned surfaces without SAM remained hydrophilic. Corrosion properties of all hydrophobic and hydrophilic magnesium surfaces were investigated using electrochemical impedance spectroscopy (EIS) in saline solution. Compared to smooth unmodified surfaces, significantly improved and

similar corrosion resistances were observed on both hydrophobic and hydrophilic surfaces. Corrosion rate reduction on micropatterned hydrophilic/phobic surfaces was also verified by prolonged submersion tests in saline solution. Unexpected corrosion inhibition on hydrophilic surfaces was investigated and evidence of local alkalization near microstructures was found. It was concluded that corrosion inhibiting mechanism for hydrophilic surfaces is possibly being caused by local alkalization and the resulting stabilization of $Mg(OH)_2$ layer. This is different than the mechanism behind hydrophobic surfaces' corrosion resistance, which makes use of gas adhesion at the liquid solid interface as once more verified in this study along with previous studies in literature.

Chapter 1: Introduction

1.1 Magnesium in Medical Field

Medical applications have been positively affected by the implementation of the biodegradable materials since the ancient times starting with the Catgut sutures made of sheep intestine [1] that dissolve in applied tissue after complete healing is achieved. Biodegradable materials used as temporary implants inside living subjects, eliminate the need for additional surgical removal operations by dissolving and joining the metabolism after remaining intact and keeping their physical properties until the connected tissue is healed completely [2, 3]. Since the ancient times up to modern day, biodegradable material technology has improved significantly. Currently several biodegradable material alternatives are in use including but not limited to; iron, iron alloys and polymers like poly glycolic acid (PGA), polylactic acid (PLA), poly ε-caprolactone(PCL), poly ortho esters (POEs), poly 3-hydroxybutyrate (PHB), polyanhydrates, poly propylene fumarates (PPF), poly ethylene glycol (PEG), tyrosine derived polycarbonates [4]. Furthermore, ongoing research on the topic are focused on allowing the use of several metals, alloys, composites and polymers which will provide wide selection of medical solutions for different situations that require diversified needs such as strength, lightweight, elasticity and porosity.

Today, one promising material that is being researched in biodegradable applications is magnesium. Seventy years after its first production by Sir Humphry Davy in 1808, magnesium was documented to be used in the medical field for the first time as a ligature

wire in pure form[5]. Following that breakthrough, along with its pure form, several different types of magnesium alloys and treated magnesium have been serving the medical field. Magnesium is beneficial due to its biodegradability and relatively better mechanical properties such as high strength to density ratio compared to the alternatives like steel and aluminum [6, 7]. During and after the oxidation, the resultant magnesium ions can be resorbed within the body to support and even promote growth in the bone tissue [8]. Potential applications of medical magnesium as biodegradable implants include cardiovascular stents, wires, connectors, musculoskeletal applications and sutures [5].

1.2 Challenges

Along with the great benefits of magnesium implants, there are drawbacks that require further research and improvement in order to develop effective implant solutions using magnesium. The major issue with subcutaneously implanted magnesium degradation is the rapidness of corrosion and the evolved hydrogen gas generated as magnesium dissolves within the body environment. Lespinasse indicated that at 0°C temperature for 24 milligrams of pure magnesium, 22.4 cm^3 of hydrogen is generated. In the warmer body environment, each milligram of magnesium will liberate 1 cm^3 of hydrogen gas [9]. Even though moderate hydrogen gas evolution is tolerable within the body by adsorption of the gas up to a certain rate [10], rapid hydrogen evolution in body environment results in undesirable situations such as internal gas bubbles under the skin around the healing area [11]. Additionally, the implant may lose its mechanical integrity prematurely due to fast corrosion before the tissue healing is complete. This phenomenon sums up the major obstacle that keeps the applications of biodegradable implants made of magnesium and its

alloys below a certain level, especially for the relatively large volume orthopedic implant applications.

1.3 Hypothesis and Dissertation Outline

Several studies have been performed in order to resolve the rapid degradation rates of magnesium within the human body causing intolerable hydrogen gas evolution, premature loss of implant's mechanical integrity and unwanted local alkalization hindering the proper healing of bone tissue. Various methods have been adopted by multiple research groups to solve this problem and a summary of these methods are documented in Section 2.3. Dissimilar to the current ongoing studies, the objective of this research is to test whether slower Mg corrosion rates can be achieved by micro-patterning the surface of polished pure magnesium plates via laser ablation. The optimal surface texture is hypothesized to entrap hydrogen gas within the surface features, hence building a hydrogen gas layer over the surface, evolved from the oxidizing Mg substrate itself (Figure 1.1). The gas layer would act as a buffer, inhibiting extremely rapid in-vitro degradation seen on polished magnesium surfaces. Ideally, altering the 3D micro-texture dimensions machined via laser ablation would make it possible to fine tune a micro-textured surface's corrosion rate. Desired surface texture yielding desired corrosion properties should be easily generated on any magnesium implant surface in a fast manner using cutting edge laser ablation technology.
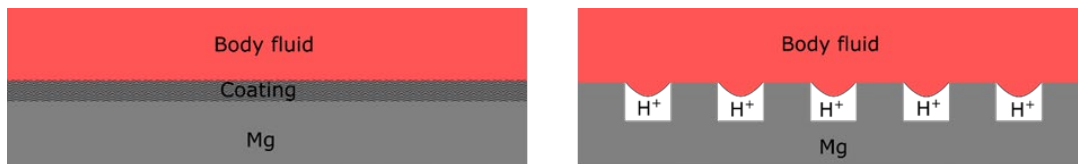
Figure 1.1 Not to scale illustration of (a) polymer coating method (b) bubble entrapment hypothesis to slow down the corrosion.

In this research, ultra-pure magnesium (99.9999% Mg or 1 ppm impurity) substrate material was used since magnesium alloys are known to corrode faster than ultra-pure Mg due to present secondary phases causing microgalvanic acceleration [12, 13]. Also, because of the same reason, the mechanism behind magnesium alloys' corrosion is highly complicated and not well studied [14, 15] to enable confidently adopting electrochemical measurement methodology which is one of the few fast and reliable quantifying methods to assess corrosion behavior.

The key to achieve hydrogen entrapment on the patterned pure magnesium surfaces is believed to be highly correlated to wetting properties of the surface in question [16]. In Section 2.4.1.1, the relationship between wetting properties and submerged in-vitro corrosion behavior is discussed based on prior studies in the literature.

Chapter 2 summarizes the current literature on magnesium's corrosion mechanism. Previously adopted methods to influence corrosion behavior of Mg were summarized. Relationship between wetting behavior and corrosion behavior along with methods used to assess the corrosion properties of Mg in literature is also covered in this chapter.

Chapter 3 is dedicated to explanation of laser machining setup used to create micro-textures on polished magnesium surfaces. The effects of average laser power, partial laser beam overlap and number of laser scans on the height, steepness, and roughness of the ablated micro-structures are documented. Information documented on this chapter was useful in creating the desired micro-patterned surfaces tested in in-vitro submersion and electrochemical experiments to assess their corrosion behavior. The results of these corrosion assessment experiments are documented and discussed in Chapter 4:.

4

Comprehensive discussion was made in Chapter 5, incorporating the hypothesized expected and unexpected results observed from experimentations documented in Chapter 4 as a method to achieve tunable corrosion rates on magnesium substrates.

Finally, Chapter 6 is devoted to conclusions of all the work covered in this study and proposal of future work.

Chapter 2: Background

2.1 Corrosion Mechanism of Magnesium

Since the focus of this research is on subcutaneous medical applications of magnesium, the oxidation behavior of submerged magnesium in an aqueous medium is a crucial parameter. Magnesium in an aqueous environment is highly reactive hence prone to oxidation. The magnesium oxide and/or magnesium hydroxide layer formed on top of the surfaces are soluble in most pH neutral and acidic environments and less soluble in alkaline (basic) environments [17]. Because of this phenomenon, the corrosion inhibiting effect of self-formed hydroxide layer seen on other lightweight metals such as aluminum and titanium is not observed on magnesium surfaces in neutral or acidic medium [17, 18]. Curioni et al. also concludes, the increase in pH (causing alkalinity) locally near the magnesium surfaces due to hydrogen evolution allows a stable magnesium oxide/hydroxide film, which results in momentary corrosion inhibition until the pH levels drop in medium [18].

2.1.1 Negative Difference Effect

The total corrosion reaction of magnesium in aqueous (H_2O) environment is stated with the following overall corrosion reaction equation [15]:

$$Mg + 2H_2O \rightarrow Mg(OH)_2 + H_2 \qquad (1)$$
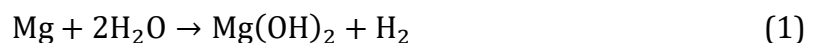
which is the result of the following anodic, cathodic and corrosion byproduct formation reactions (Equations (2), (3) and (4) respectively) [15].

$$Mg \rightarrow Mg^{++} + 2e^- \qquad (2)$$

$$2H_2O + 2e^- \rightarrow H_2 + 2OH^- \qquad (3)$$

$$Mg^{++} + 2OH^- \rightarrow Mg(OH)_2 \qquad (4)$$

According to equation (1, each corroded Mg atom produces one molecule of evolved hydrogen. However, in practical applications, the evolved hydrogen volume is measured to be larger than the predicted amounts through Faradaic conversions based on equations above. In other words, increasing anodic polarization (Mg dissolution) also causes an increase in total cathodic polarization (hydrogen evolution) happening during corrosion. This is contrary to what electrochemical theory suggests in which the rate of the anodic reaction is inversely proportional to the rate of cathodic reaction [14].

On Figure 2.1, expected partial cathodic reaction curve (I_c) that is responsible for hydrogen evolution is shown. Actual evolved hydrogen was measured via gas entrapment methods at an applied external potential (E_{appl}) and corresponding polarization current ($I_{H,m}$) was calculated using Faradaic conversions. However, this calculated current does not fall on the expected cathodic curve at any applied potential above the corrosion potential (E_{corr}). The new measured hydrogen evolution curve was denoted by a dashed line (I_H). Which shows that all polarization current values related to actual hydrogen evolution ($I_{H,m}$) fall on the right hand side of the corrosion current (I_0). Consequently, the difference between I_0 and $I_{H,m}$ is always found to be negative above the corrosion potential. Hence, this unique behavior observed during magnesium's oxidation process is named "negative difference effect" (NDE) [15, 18]. There are three mechanisms suggested to explain this phenomenon observed with high purity magnesium [19].
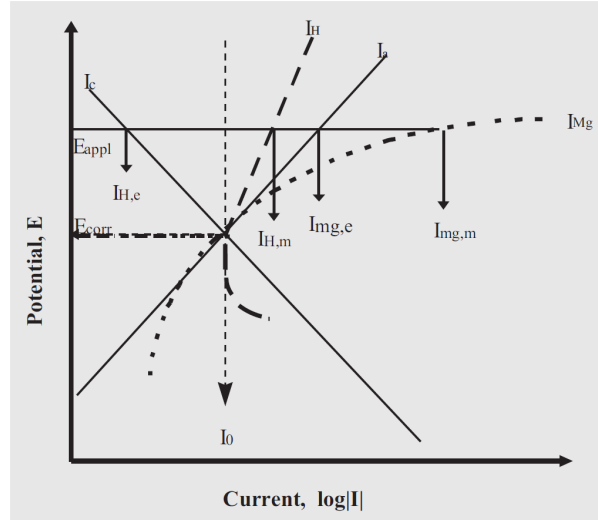
Figure 2.1 Negative difference effect seen on magnesium [15]. I_c: expected partial cathodic reaction (hydrogen evolution) curve. I_H: measured hydrogen evolution. I_a: expected partial anodic reaction (Mg dissolution) curve. I_{Mg}: Measured Mg dissolution.

First explanation for NDE assumes an intermediary anodic reaction that generates unipolar magnesium ions (Mg^+) that keep oxidizing further in the corrosive medium (Equation (5)) and ramp up the hydrogen evolution through a secondary cathodic reaction (Equation (6) in addition to the expected cathodic reaction stated on equation (3.

$$Mg \rightarrow Mg^+ + e \tag{5}$$

$$2Mg^+ + 2H^+ \rightarrow 2Mg^{++} + H_2 \tag{6}$$
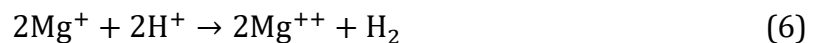
Second mechanism suggests reduction of magnesium to magnesium hydride (MgH_2) through equation (7. Magnesium hydride is not stable in aqueous medium therefore it chemically reacts with water and generates hydrogen gas (Equation (8).

$$Mg + 2H^+ + 2e \rightarrow MgH_2 \tag{7}$$

$$MgH_2 + 2H_2O \rightarrow Mg^{++} + 2OH^- + 2H_2 \tag{8}$$
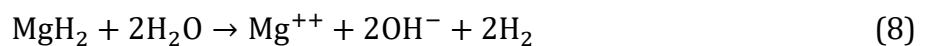
Third mechanism ties the unexpected hydrogen evolution to dissolution of the protective film (composed of MgO or Mg(OH)2) on the magnesium surfaces during anodic polarization. Increased externally applied currents or potentials during electrochemical

measurements may cause this dissolution. Curioni et al. also mentions this third interpretation of NDE which attributes it to the increased cathodic activity at the regions on the surface that are going through corrosion (due to anodic activity) regardless of the water reducing effect of dissolved magnesium ions. The increased hydrogen evolution is thought to be caused by the cathodically active regions generated on the magnesium surface as the corrosion proceeds. Williams et al. have recently conducted experiments that verify this theory [20].

Because of NDE, solely relying on electrochemical polarization data to assess corrosion behavior of magnesium is questionable [12]. Nevertheless, the rate of evolved hydrogen volume is a qualitative metric of rate of corrosion happening on the surfaces through correlation, even though exact quantification (in terms of mm/year) through electrochemical theory is a convoluted process.

2.1.2 Surface Dynamics During Mg Corrosion

Magnesium's corrosion is driven by the stability of formed protective film over the surface. The film is mainly composed of $Mg(OH)_2$ molecules and its formation is governed by the reaction shown on equation (1. Stability of this film highly depends on the environment that is in contact. According to Pourbaix diagram for magnesium in aqueous solutions (showing the relation between pH and thermodynamic stability domains), it is not thermodynamically feasible for a $Mg(OH)_2$ layer to exist at pH levels lower than 10.5 as the layer renders unstable and dissolves in the medium [21, 22]. As mentioned earlier, the dissolution of protective layer causes an increase in the corrosion rate of magnesium. However, in practice, dissolution rate of the protective layer is slower than the new film formation rate, allowing partial protection against corrosion. This phenomenon is thought

to be caused by local alkalinity due to the hydrogen evolution reaction defined by equation (3— where reaction byproduct hydroxide ions (OH⁻) cause an increase in pH [23]. Local alkalization on polished magnesium surfaces has been experimentally proven by Simaranov et. al [24]. Near the corroding magnesium surface, a pH value of 10 was measured even though the bulk solution was highly acidic at pH 4. Hence, stability of the protective $Mg(OH)_2$ film was promoted by higher pH values in vicinity of the corroding area even though the overall environment in bulk (pH < 10) does not theoretically allow presence of a stable protective film.

Another important property of the corrosive solution is its temperature. It is known that for pure magnesium, increasing temperature of liquid environment is directly proportional to increasing corrosion rates [15]. This fact should be considered when predicting in-vivo behavior of a metal based on in-vitro experiments. Ideally all in-vitro tests should be conducted in a medium at human body temperature for biomedical implant research purposes.

2.1.3 Effect of Solutes in Medium

Many studies including this one, use an aqueous corrosive medium containing several salts and dissolved carbon dioxide to closely simulate the human body environment at varying levels of fidelity (if not 100%, which is achieved through in-vivo testing). However, the immersed corrosion mechanism of magnesium discussed so far only considered the solvent as the corrosive medium which is water. Internal human body environment (i.e. blood plasma) contains electrolytes such as Na^+, Ca^{2+}, Mg^{2+}, HCO^{3-} and Cl^- ions [25], hence it is important to understand the effects of ion presence on corrosion behavior.

Song et al. [14] have investigated the effects of NaCl, Na$_2$SO$_4$ and NaOH solutions separately on natively formed protective film over magnesium surfaces. Presence of especially Cl$^-$ ions has shown to have an activating effect on the on the Mg(OH)$_2$ film, causing increased corrosion as the film dissolves/breaks and reveals the corrosion prone regions underneath. The involvement of intermediate Mg$^+$ species during anodic reaction steps also has been verified. As the protective layer oxidized due to Cl$^-$ ions, Mg+ ions have been released. Mg$^+$ ions then reacted with electrolyte to produce hydrogen gas and Mg^{2+} supporting one of the theories causing NDE discussed in section 2.1.1. Zhao et al. [23] have also confirmed higher concentrations of chloride causing protective film breakdown ramping up corrosion rates.

2.2 Corrosion Assessment Methods

There are a variety of techniques to study corrosion. Each has its advantages and limitations. They are summarized below.

2.2.1 Simulating In Vivo Conditions

A study done in 2005 by Witte et al. [26] investigated the correlation of in vivo and in vitro corrosion measurements. Immersion tests were conducted using AZ91D and LAE442 alloys along with in vivo experiments in animal tissue. The resultant corrosion characteristics did not correlate between in vivo and vitro setups. However, the in vitro setup environment used to simulate bio organism was based on ASTM-D1141-98 protocol which is a substitute for ocean water instead of a biological fluid. Hence it was expected to observe a lack of correlation. Systems that simulate a biological environment more accurately were introduced later with the adoption of SBF (simulated body fluid) and control systems that

regulate pH and temperature that became more and more commercially available in time like Schinhammer's setup explained below.

Schinhammer et al. have introduced a fully automated in vitro setup that simulates the body environment implementing the SBF solution. The system consists of temperature and pH regulation with the use of CO_2 diffusion into the in vitro tank instead of using the traditional pH buffering methods such as using Tris, PBS or α-MEM buffered SBF solutions as medium. Their tests with WZ21 magnesium implant alloy have shown a corrosion behavior very similar to an in vivo testing, which suggests that CO_2 infused pH buffering is the closest possible testing method to animal testing also given the fact that it is the same buffering system present in human blood. The comparative corrosion behaviors of WZ21 alloy in Tris, PBS, α-MEM and CO_2 buffered SBF solution along with in vivo testing can be seen in Figure 2.2 [27].

It should be noted that on PBS and Tris buffered systems the pH of the system is adjusted by dripping the corresponding buffering agents into the system which yields unstable pH characteristics between the intervening time points. Automated CO_2 buffering allowed precise pH regulation that is always kept within the tolerance limits (pH 7.40 ±0.05) [27].
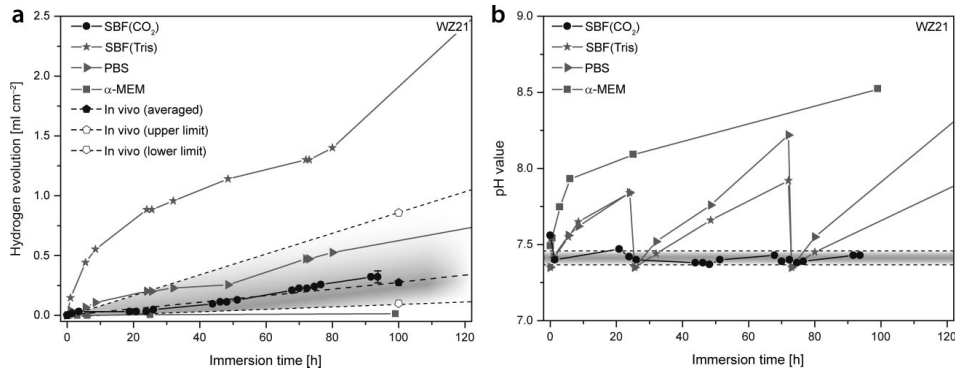
Figure 2.2 (a) Hydrogen volume evolution comparison of in vivo environment to various buffered in vitro setups (b) pH variance in differently pH regulated in vitro corrosive media over time. [27]

Wang and Li et. al, for their immersion test in NaCl solution, the rates of corrosion in the corrosive medium was quantified by observing the pH change of the solution since the pH is expected to increase with the degradation of magnesium and release of hydrogen ions. Another measure of corrosion rate was to observe the concentration of dissolved Mg in the NaCl solution [28].

2.2.2 Corrosion Characterization Methods

2.2.2.1 Gas Evolution

Once the corrosive medium is accurately selected and conditioned according to needs, in-vitro submersion tests are more direct and unconvoluted corrosion assessment methods. In addition to pH change measurements and quantification of dissolved substrate material (Mg ions in this case) inside the liquid, the hydrogen gas volume generated by corrosion is a useful metric to assess corrosion rate.

2.2.2.2 Mass Loss

Gravimetric mass loss data is also another metric. Mass measurements are taken from a sample before and after submersion into corrosive medium. Lost mass amount after certain duration of submersion gives direct metric in terms of amount of material per a unit area

13

after simple arithmetic conversions involving material's density and volume. It is important to clean any corrosion byproducts (oxide/hydroxide layer) off the surface post submersion using a material specific ASTM cleaning procedure [29] in order to accurately quantify actual mass lost due to corrosion.

2.2.2.3 Electrochemical Testing

In-vitro immersion setups like Schinhammer's setup combined with gravimetric and hydrogen evolution measurements are reliable tools to predict a material's degradation behavior inside a living organism. A replica of Schinhammer's setup was used in previous work by the author [30] with success. However, operation and maintenance of such setups are relatively involved processes. In addition, getting definitive degradation data of the material in scope usually requires significant amount of testing time that can take up to several months. Electrochemical measurements are still reliable (as long as their accuracy is verified through preliminary secondary tests) and practical methods that give definitive results in shorter time and require much less maintenance and setup time.

Lucas et al. [31] investigated the accuracy of in-vitro electrochemical measurements compared to in-vivo experimentations. They compared in-vitro and in-vivo corrosion performances using Co-Cr-Mo and Ni-Cr-Mo alloys as test specimens. In-vitro electrochemical measurements were performed using 0.9w% saline solution at 37°C temperature as the electrolyte. In-vivo experiments were conducted by placing cylindrical samples with the same properties into rear leg muscles of rabbits and polarization data was collected from internal body of the animal for as long as six weeks. Corrosion rate data gathered from both experiment setups were statistically not different from each other which is an indication of accurate representation of in-vitro electrochemical experimentation data

14

to real life implant application. Even though Lucas et al.'s study proves the accuracy of electrochemical measurements on non-magnesium-based metal alloys, it is accepted as an assuring result for the method's applicability for magnesium alloys' corrosion behavior.

2.2.2.3.1 <u>Potentiodynamic Polarization</u>

Potentiodynamic (PD) polarization test is one of the most common electrochemical analysis methods to directly determine polarization resistance of a material. Using a potentiostat, varying electrical potential within a range (usually around known corrosion potential 'E$_{CORR}$' of the corroding system) is applied to the tested specimen. In galvanostatic tests, applied potential is usually controlled by changing the applied current as a variable. Following the potential/current sweep, the outcome is plotted showing the change of current with varying potential or vice versa. The resultant curve usually plotted with a logarithmic scale is called "polarization curve" (Figure 2.3). Polarization resistance (R$_p$) is defined as the slope of the linear segment of the polarization curve near corrosion potential when plotted in a linear scale. It is possible to calculate corrosion rate through Tafel slopes in accordance to ASTM G59 standard once the Rp is obtained.

In this work, potentiodynamic polarization measurement method was not adopted since corrosion mechanism of magnesium is highly time dependent and complex in terms of electrochemical interactions. PD polarization is also a destructive test since external current/potential is introduced to the system, restricting consecutive testing of the same specimen surface.
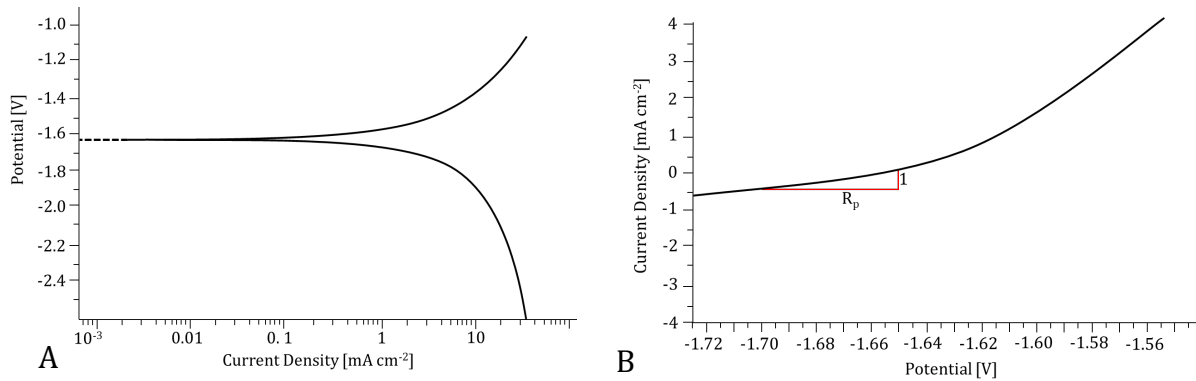
Figure 2.3 Logarithmic scale (A) and linear scale (B) polarization curves for pure magnesium in 3.5% NaCl solution. Images reproduced from reference [18].

2.2.2.3.2 Electrochemical Impedance Spectroscopy (EIS) Method

EIS is a non-destructive electrochemical method used to determine polarization resistance (R_p) hence the corrosion rate of a material in an electrolyte. Besides determination of Rp, EIS is useful to detect localized corrosion as well as in obtaining interfacial capacitance corrosion rates, reaction kinetics, mass transport and dielectric properties [32]. It is also possible to collect time dependent data with EIS due to faster data collection and capability of repeated measurements in the same region in a nondestructive way.

Using a potentiostat, a small-amplitude sinusoidal potential is applied (resulting an alternating current) to the tested specimen at varying frequencies. Impedance spectrum of the sample is then represented as either Nyquist or Bode plots. On the Nyquist plot, applied potential's frequency increases in counterclockwise direction along the semi-circle shaped curve. For a simple corroding system (Figure 2.4-A), impedance at the highest frequency gives the solution resistance (Rs) and the lowest frequency impedance will give the sum of solution and polarization resistances (Rs + Rp).

This ideal simple system can be represented as an equivalent circuit containing a capacitor in addition to resistors representing polarization and solution resistances. Capacitor (C) represents the interfacial capacitance for an ideal system behavior since metal-electrolyte interface can store electrical charge as well as transporting it. However, in complex systems such as magnesium corrosion, the interfacial capacitance is substituted with a constant phase element (CPE) to better fit the impedance of a double layer behavior caused by the protective hydroxide layer present on magnesium surfaces. Double layer impedance is usually apparent on a Nyquist curve when a vertically depressed semi-circular curve is observed (Figure 2.4-B). When the surface properties get more complex (i.e. surface patterning or roughness), more adjustments and component additions are needed on the equivalent circuit in order to fit the data accurately. Determination of an equivalent circuit requires a good understanding of the corrosion mechanics happening on the surface in order to interpret the results of EIS measurements. Correspondingly, by identifying an equivalent circuit that properly fits the collected impedance spectra, meaningful insight on detailed corrosion mechanisms happening on the magnesium surfaces can be obtained.
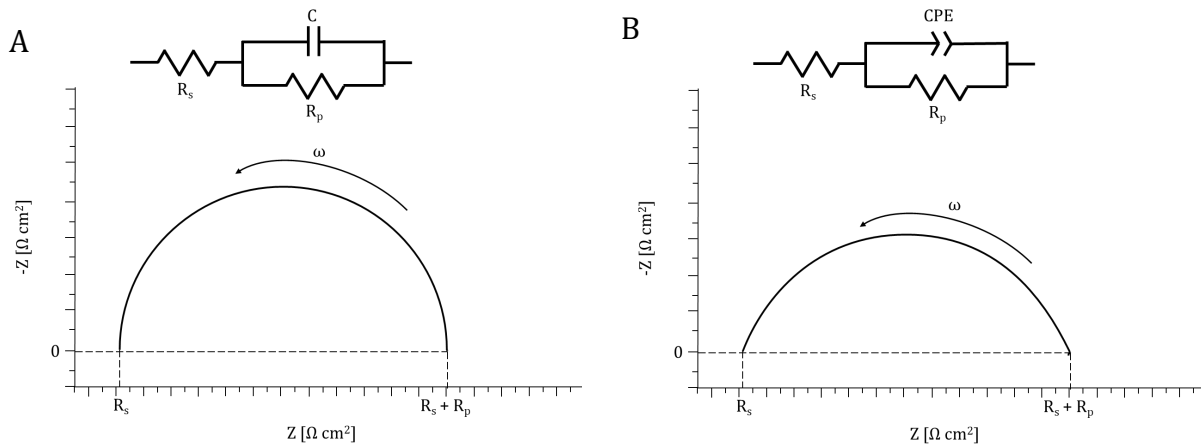
Figure 2.4 Nyquist curves along with equivalent circuits denoted on top. Simple ideal system (A) and CPE behavior caused by double layer capacitance (B). ($\omega = 2\pi f$, f: frequency of applied potential)

Ishizaki et. al [33] have used EIS to assess the corrosion performance of a rough magnesium alloy (AZ31) surface coated by nanostructured cerium oxide and fluoroalkyslsilane molecules rendering super-hydrophobicity. Three different equivalent circuit models were used representing unmodified flat Mg alloy surface, superhydrophobic Mg alloy surface and hydrophilic Mg alloy surface respectively (Figure 2.5). There was a need for a third model representing hydrophilicity since 1440 minutes of submersion in electrolyte solution deteriorated the hydrophobic properties.
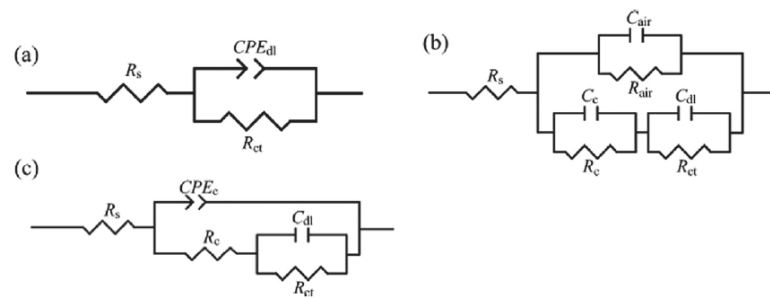
Figure 2.5 Equivalent circuits used for untreated flat Mg alloy (a), super-hydrophilic Mg alloy (b) and hydrophilic Mg alloy (c). [33]

First equivalent circuit—as also explained above in detail—represents the corrosion behavior of untreated smooth AZ31 alloy. Circuit components include, solution resistance (R_s), charge transfer resistance (R_{ct}) indicating the total corrosion resistance performance (used interchangeably with R_p in this dissertation) and the CPE element in parallel representing the double layer behavior (Figure 2.5a). Second equivalent circuit (Figure 2.5b) is representing the superhydrophilic surface with many minute pores that comes with hydrophobic coating and presumed gas bubble entrapment within these pores. Instead of a CPE, the double layer mechanism is split into two subsystems in series (assuming defects in the protective film), each composed of a capacitor and a resistor. $R_c||C_c$ subsystem represents

18

the interface reaction between the electrolyte and the protective film. $R_{ct}||C_{dl}$ subsystem represents the interface reaction between the protective film and the substrate. In parallel to these two subsystems in series, subsystem of $R_{air}||C_{air}$ is placed representing the entrapped air and the nano-pores that encapsulate the air. Finally, the third equivalent circuit representing the hydrophilic case (Figure 2.5c) assumes a defect free protective layer that is promoted by full contact of the substrate with the electrolyte. Hence, the C_c component that stores charge at the electrolyte-protective film interface is not present due to lack of imperfections. Since the air layer is not present anymore, the $R_{air}||C_{air}$ subsystem in parallel is again substituted with CPE representing protective layer's overall behavior. Finally, the R_{ct} values from all stages of experiments incorporating three equivalent circuits were compared. Decreasing corrosion resistance trend over prolonged immersion durations (> 200 minutes) was observed even though initially super-hydrophobic samples have shown superior corrosion resistance. However, since Ishizaki et. al's study is done on a Mg alloy, the effect of secondary phases in the material matrix must be considered. Since, EIS is the sole quantification method for corrosion resistance, the results are questionable for a Mg alloy due to reasons mentioned in section 1.3. However, the proven good fit of proposed electrochemical circuit models to experimental data is a promising reference for the purposes of this dissertation.

Curioni et. al have defined an equivalent circuit model for smooth pure Mg surfaces. Their equivalent circuit model overlapped with corrosion mechanism schematic of Mg surfaces is shown on Figure 2.6. Elements of the equivalent circuit are picked based on real life qualitatively defined electrochemical interactions. Air formed and corrosion byproduct oxide/hydroxide films are represented by capacitors C_{AF} and C_{OX} respectively. Since these

19

two capacitors are connected in parallel, they cannot be distinguished when fitting the impedance spectrum. Therefore, C_{AF} and C_{OX} are grouped in a single capacitor representation named C_{ox}. On the diagram, air formed film is named "silvery" and corrosion byproduct film is named as "dark" referring to their distinct colors observed during corrosion. Since corrosion byproduct films drive the corrosion mechanism (section 2.1.2), the decreased charge separation behavior at thin or defective film areas are represented by capacitor C_{DL}. Connected in parallel to C_{DL}, electron transfer is represented by a resistor R_{CT}. Precipitated magnesium oxide/hydroxide gels due to locally increased pH near the anodic and cathodic regions are represented by resistors R_A (in series with an inductor L_A) and R_{CP} respectively. Further technical details on the necessity of an inductor in anodic region is available in the cited reference [18].
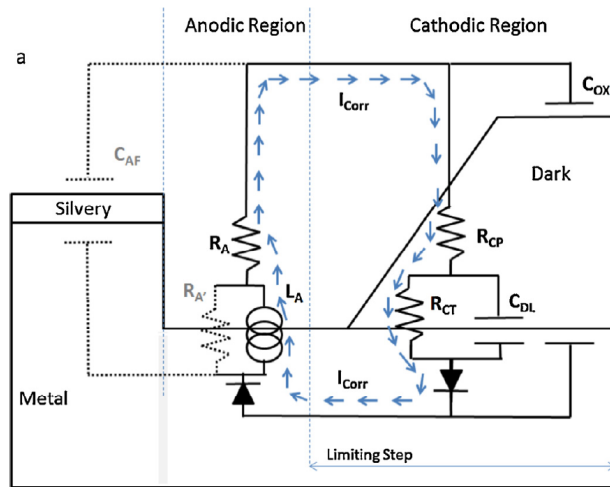
Figure 2.6 Curioni et. al's equivalent circuit for polished pure magnesium surfaces. Solution resistance is not shown on the schematic. [18] (This figure is taken from an open access article distributed under the terms of the Creative Commons CC-BY license)

2.3 Alternative Methods to Influence Corrosion Resistance of Magnesium

The focus of this research is to investigate the laser ablated surface geometry profiles' effect on the corrosion rate of pure magnesium. To have an idea of other factors that might

influence the corrosion behavior of the samples, a review is conducted on the effects of alloying, coating and heat treatment.

2.3.1 Alloying

Magnesium has good mechanical properties such as high strength and low density which makes it desirable for the industry of aerospace and automotive. However, the biggest problem is the high reactiveness of magnesium in corrosive environments and atmospheric air also. Corrosion resistance of magnesium is improved by alloying with other less reactant (passive or inert) metals such as Ni, Ti, Al and Cr. However, there is a challenge in keeping the high strength to weight ratio that magnesium offers. Since magnesium is highly chemically active, to compensate for the reactiveness, large portions of less reactant metals needed to be used in the alloy and this deteriorates the mechanical advantages [34].

On the other hand, there is a possibility of a large tradeoff between corrosion rate and mechanical properties in biomedical applications unlike the aircraft and automotive industry which can't afford to have corrosion vulnerability. Song et al. [35] mention the need of high ratio of non-reactant metals is needed in the Mg alloy to have inert overall corrosion properties. In biomedical applications the alloy does not needed to be highly inert, as it is desirable to degrade over time. Hence it is possible to have improved corrosion resistance up to a certain level by keeping good mechanical properties for biomedical applications with using low percentages (<5%) of alloying metals.

The use of rare earth elements in magnesium alloys for biodegradable implant applications is common. Even though rare earth elements are highly reactive by themselves, in compound form with other noble elements such as Al, Mn, Zn, Fe, Cu and Ni their corrosion characteristics are stable due to the compounds' low electrode potentials. Hence, those

21

compounds are good candidates to be alloyed with magnesium to lower the overall corrosion response. There are 17 rare earth elements that include scandium, yttrium, and lanthanum which are the most common ones used in alloying. Those 17 elements are divided into two groups named as cerium and yttrium groups. Cerium group is composed of light rare elements and yttrium group is relatively heavier. Overall it is possible to create alloys with improved mechanical and anticorrosion properties such as WE43 magnesium alloy which is a rare earth element alloy consists of yttrium (RE) compound with zirconium [36].

Chen et al. compared the biocompatibility and biodegradability properties of Mg-Zn alloys to PLLA which is a polymer that is also widely used in biodegradable applications. Materials' in vivo degradation comparisons showed that Mg-Zn alloy degraded faster with improved bone formation around the material compared to the PLLA polymer. This proves the inclusion of Zn in Mg alloys modulating biodegradation while keeping the implant biocompatible since both Mg and Zn can be metabolized without causing any toxicity effects. Inclusion of Zn also relatively slows down the corrosion rates relative to high purity magnesium. It was observed that on Mg-Zn alloy, cell attachments were also superior to PLLA as a result of animal testing which is desirable for biocompatibility [37].

2.3.2 Heat Treatment

Another area of interest on corrosion resistance of magnesium and its alloys is heat treatment. Li et al. [38] investigated the "effect of heat treatment on corrosion behavior of AZ63 magnesium alloy in 3.5 wt% sodium chloride solution". To observe the corrosion rate, gas collection method is used by placing funnels above the samples and trapping the evolved gas during corrosion. The samples were prepared starting by manual alloying of AZ63 by melting pure metal ingots of Mg, Al, Zn an Mn together in a furnace at 720°C, then pouring

22

them into a preheated steel mold resulting a solid AZ63 alloy with composition of 5.7 wt% Al, 2.7 wt% Zn and 0.3 wt% Mn with remainder Mg. After pouring into the mold, the alloy is cooled by water. Subsequently one group was heated up to 385°C for 20 hours and quenched in water (referred as homogenized group - T4) while another group was heated up to 260°C for four hours and quenched in water (referred as peak aged group - T5). Untreated as cast samples corroded more slowly than both T4 and T5 samples which correlates with the statement of Wang et al. [39] that claims precipitates within the alloy decrease the corrosion rate.
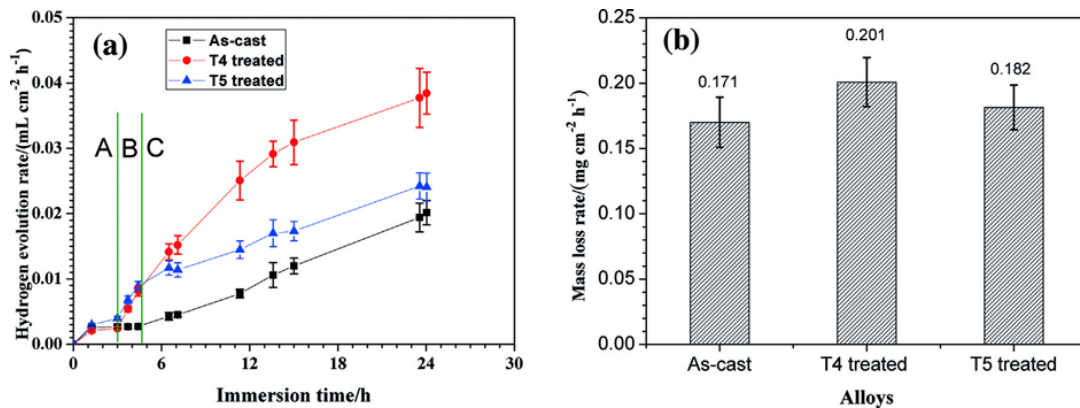
Figure 2.7 (a) Evolved hydrogen and (b) mass loss in NaCl solution for different heat treated samples. [38]

2.3.3 Coating

Magnesium coating technologies to bring down the corrosion rate include; electrochemical plating, conversion coatings, hydride coating, anodizing, gas phase deposition, laser surface alloying/cladding, organic/polymer coatings [40]. Gray et al. reviewed these several types of coating methods applied on magnesium for use of large-scale implementations like automotive and aerospace applications. However, since Gray's review paper does not include coating methods applied for biomedical applications, the details of large-scale application specific methods are not included in this review.

When it comes to coating types that is used for biomedical/biodegradable applications of magnesium, there is a lack of scientific sources in literature since it is a relatively new area of interest and there are several currently ongoing investigations related to it. Once the studies are complete and patents on coating alternatives are secured, scientific documentations are expected to increase in number [41]. So far today, Ca-phosphate and hydroxyapatite coatings' performance in biologic medium have been investigated in literature.

Waterman et al. [42] investigated the effects of calcium phosphate coatings on pure magnesium for biomedical applications. The coating is applied in two steps. First, 15 x 15 mm^2 squares of pure magnesium were electroplated in a 2M $Ca(NO_3)_2$ solution with a Pt plate as counter electrode. Samples were plated under 3.2V of voltage for 10 minutes resulting with a coating layer of calcium hydroxide ($Ca(OH)_2$). Subsequently as a second coating step, electroplated (ECAD) samples were coated with biomimetic method which involves dipping the ECAD samples into a high concentration (5x) SBF solution at 37°C and pH 6 (achieved by diffusing CO_2 gas into the SBF once before the experiment). The immersion resulted in a CaP (calcium phosphate) coating on top of the ECAD calcium hydroxide coating. The reasoning behind the selection of SBF immersion for coating was explained with the method being a non-toxic and biocompatible method that does not involve any chemical that is not present in a living body. Finally, the corrosion resistance of uncoated, biomimetic coated and ECAD + biomimetic coated samples were tested in a Hank's balanced salt solution (HBSS) at 37°C and pH of 7.4 buffered with 25mM HEPES acid. Hydrogen evolution was observed over the course of 14 days. ECAD + biomimetic coated samples demonstrated the

24

most resistance to corrosion. The comparison between three sample groups' evolved hydrogen amounts at the end of 14 days can be seen below on Table 2.1.

Table 2.1 Comparison of Hydrogen volume. [42]

Sample	H_2 at 14 days
ECAD + biomimetic	2.9 mL
Biomimetic	23.9 mL
Uncoated	35.6 mL

The superior corrosion resistance of ECAD coated samples is tied to the self-healing properties of the calcium hydroxide sub-layer where it fills in the eroded layers of the top CaP layer with calcium as it wears out [42].

Dunne et al. [43] studied the corrosion behavior of hydroxyapatite-coated magnesium alloys. Hydroxyapatite is known for its biocompatibility. Blast coating deposition method has been used to coat three types of alloys (WE43, EW62, EW10X04) since conventional high temperature techniques are not compatible with magnesium due to its low melting temperature of 600°C. Spraying was done with a jet pressure of 0.55 MPa 50 mm above the alloy surface at ambient temperature. The resultant surface roughness (R_a) after the spray coating was higher (~1.6 μm) than the uncoated specimens (~0.5 μm). In vitro immersion test was conducted to compare corrosion behaviors of the coated and uncoated specimens. PBS (Phosphate buffered saline) solution was used as a medium and samples were immersed for 10 days at 37°C temperature. Evolved hydrogen data yielded the data below. It was observed that EW62 alloy (6.03wt% Nd, 0.42 wt% Zr, 1.95wt% Y) with hydroxyapatite coating had the highest resistance to corrosion followed by the uncoated EW62. This also proves the importance of alloying in corrosion behavior. EW62 and

EW10X04 are fairly new developed alloys that have shown good corrosion resistance relative to the conventional WE43 biodegradable magnesium alloy.
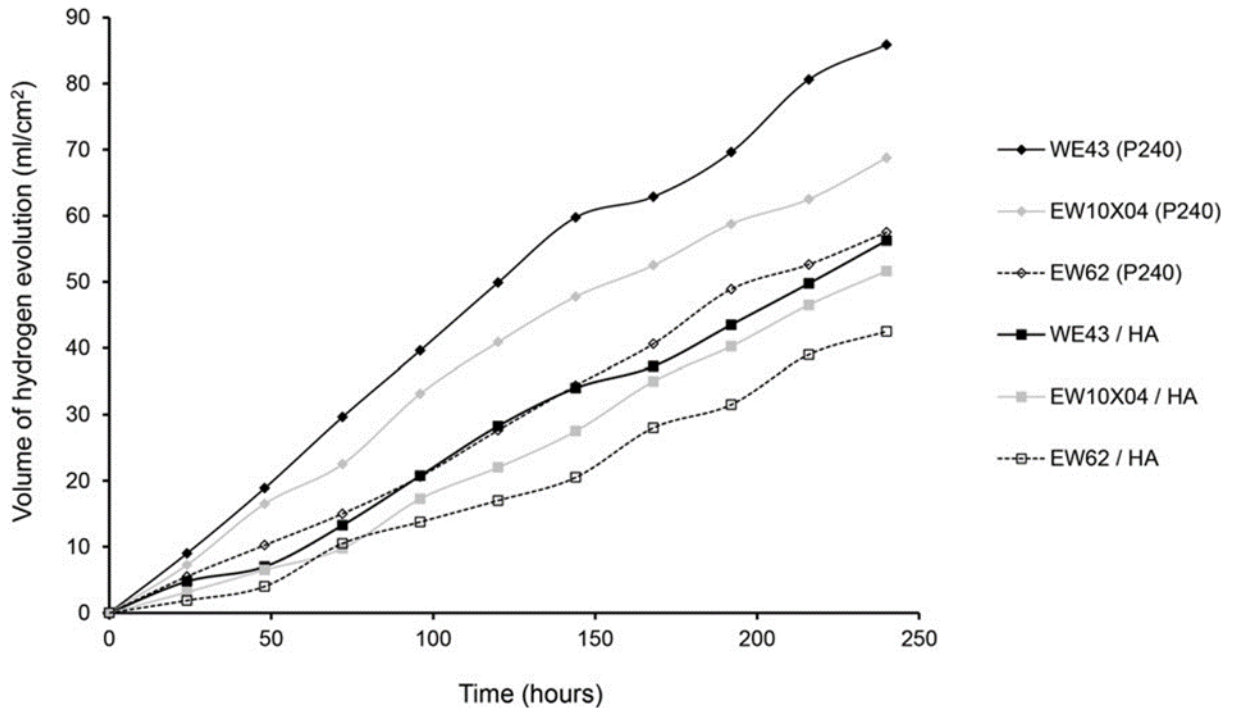
Figure 2.8 Evolved hydrogen volume in PBS solution. [43]

Ng et. al [44] have tested the corrosion protective properties of stearic acid modification applied on polished high purity magnesium. Since stearic acid has poor adhesion properties, a two-step approach was employed. Polished Mg samples were first treated hydrothermally in order to generate a stable $Mg(OH)_2$ layer with adequate thickness on the surface that would promote adhesion of stearic acid molecules. Samples were placed in a Teflon container filled with deionized water and left for 24 hours at 120° C temperature. At the end of hydrothermal treatment, a 170 μm thick $Mg(OH)2$ layer was formed. Following the film generation, three different conditions were tested to apply stearic acid. First method involved immersion in 1.5M stearic acid solution chloroform at 50° C for two hours. Second method involved immersion in 100° C liquid stearic acid for two hours. Last method involved

26

immersion in 150° C liquid stearic acid for two hours. It was observed that liquid stearic acid had a higher viscosity than chloroform solution. No contact angle measurements were taken since the purpose of the study was to create a barrier in between the substrate and the electrolyte composed of stearic acid molecules, magnesium stearate and $Mg(OH)_2$ only. Formed magnesium stearate enhanced the bonding of stearic acid on all immersion groups. Corrosion performance of all three types of coatings were tested through potentiodynamic polarization and EIS tests in Hank's solution. Highest corrosion resistance was observed on second coating group that was immersed in 100° C liquid SA. Chloroform solution and 150° C liquid SA groups had similar corrosion resistances. Corrosion behaviors of all three groups have shown correlation with the viscosity levels of the mediums that they were dipped in during coating procedure. Lower viscosity coating medium is believed to yield thicker and higher quality coating layer hence improving corrosion resistance. In the long term all samples' corrosion resistances were deteriorated significantly due to increasing electrolyte pH and defect propagation on the coating layer.

2.4 Wetting Behavior and Corrosion Resistance Relation

2.4.1 Wetting Physics

Superhydrophobic surfaces are created by entrapping air between solid-liquid interfaces, hence creating an apparent contact angles of larger than 150 degrees when a water droplet is placed on top of the surface in question [45]. In other words, hydrophobic and superhydrophobic surfaces have increased non-wetting properties. The theory behind this behavior was first studied by Wenzel in 1936 [46] and then expanded by Cassie and Baxter in 1944 [47]. They have studied the physics behind water repelling properties of non-

wetting clothing and have found a physical relationship showing that a roughened surface combined with a low surface energy coating will exhibit this behavior.

Wenzel and Cassie-Baxter models are derived from Young's equation [48] shown on equation (9 below.

$$\cos\theta = \frac{\gamma_{SG} - \gamma_{SL}}{\gamma_{LG}} \tag{9}$$

Interfacial surface energies between solid-gas, solid-liquid and liquid-gas phases are denoted as γ_{SG}, γ_{SL} and γ_{LG} respectively. Measured contact angle of a droplet on an ideally flat (polished) surface is referred to as θ or Young's angle. Surfaces in contact with water droplets showing contact angles larger than 90° are defined as hydrophobic. Otherwise, surfaces exhibiting droplet contact angles smaller than 90° are defined as hydrophilic. According to Young's relation, higher contact angles imply large solid-liquid interfacial surface energy (γ_{SL}) meaning wetting is unfavorable on the solid surface.

Dynamic measurements are employed to determine wetting characteristics of a roughened surface. In order to take a dynamic contact angle measurement, droplet is placed on the surface by increasing its volume gradually that yields the advancing contact angle. Consecutively, droplet is gradually removed by retracting it back into the application nozzle hence allowing the observation of a receding contact angle. Another common alternative method to measure dynamic contact angles involves gradually tilting the surface of interest after placing a static water droplet. Advancing and receding contact angles are observed as soon as the placed droplet starts sliding down the surface at a certain tilt angle. Static contact angle on a rough surface (apparent contact angle or θ^*) always falls between advancing and receding contact angles. Dynamic contact angle measurements give a better idea of the favorability of a roughened surface towards wetting. The parameter representing this

28

favorability is the contact angle hysteresis, which is the arithmetic difference between advancing and receding contact angles. Higher hysteresis values imply pinning of the droplet which is a sign of favorable wetting on the surface.

Wetting relationship influenced by Young's angle and surface roughness is explained by two models. Wenzel model assumes a single phase (solid) under the applied water droplet (i.e. water droplet infiltrates into the crevices of the roughness features). The model follows the relation that obeys equation 10.

$$\cos\theta^* = r\cos\theta \tag{10}$$

Roughness coefficient (r) is defined as the total surface area of the solid substrate in contact with the droplet. For a square pillared roughness structure, r value would be calculated using the equation shown on Figure 2.9.

Cassie-Baxter model assumes presence of two phases (solid and gas) under the applied water droplet (i.e. droplet "floats" on tips of the roughness features). The model follows the relation that obeys the equation below.

$$\cos\theta = f(1 + \cos\theta) - 1 \tag{11}$$

Solid fraction at the droplet interface (ƒ) is defined as the total surface area fraction of the solid substrate that is only in contact with the droplet which is supported by the solid and gas phases underneath. For a square pillared ideal roughness structure, f value would be calculated using the equation shown on Figure 2.6.
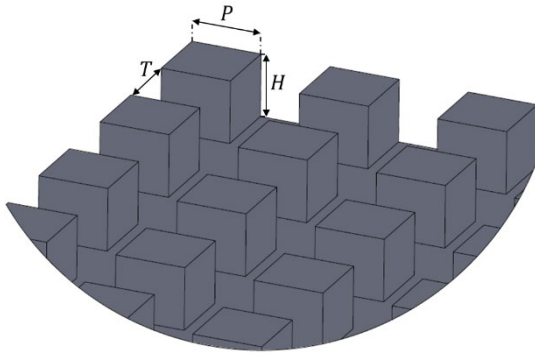
$$r = \frac{(P+T)^2 + 4PH}{(P+T)^2}$$

$$f = \frac{P^2}{(P+T)^2}$$

Figure 2.9 Roughness coefficient (r) and solid area fraction (*f*) calculation for an equally spaced square micro-pillar structure.

In theory, it is possible to calculate an ideal surface roughness structure that yields superhydrophobic behavior. Superhydrophobic behavior ($\theta^* > 150°$) is theoretically better understood through Cassie-Wenzel state as gas entrapment within the roughness grooves contribute to the non-wetting behavior the most. With Cassie-Wenzel formulation the key geometry features for a square pillared microstructure would be independent of the pillar height theoretically (Figure 2.6).
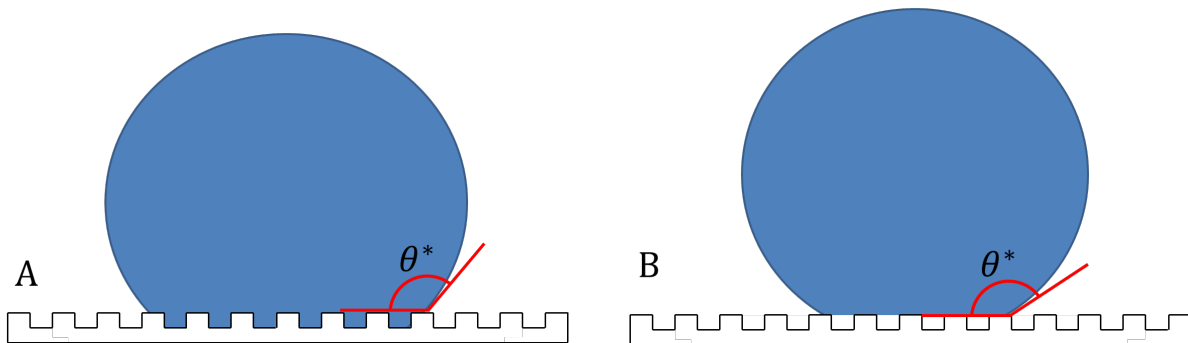
Figure 2.10 Wenzel (A) and Cassie-Baxter (B) wetting models.

2.4.1.1 Submerged Conditions

Both Wenzel and Cassie-Baxter models adopt droplet-based formulations observed in a dry setting. Even though it is possible to confirm validity of Cassie-Baxter super-hydrophobicity through cutting edge manufacturing methods allowing complete control

over surface roughness profiles, the entrapped gas stability on a superhydrophobic surface in submerged conditions is unclear. Entrapped gas stability is thought to be a key factor to create a gaseous protective layer against corrosion inside a liquid. Several research groups have empirically assessed the stability of the immobilized gas on superhydrophobic surfaces in submerged conditions [45].

Poetes et al. [49] have prepared roughened aluminum samples with Teflon coating. Roughness structure was geometrically random due to the bead blasting method used to roughen the Al surfaces. Following the Teflon coating treatment, apparent contact angles were measured to be around 160° (no contact angle hysteresis information) pointing superhydrophobic properties. Prepared samples were mounted inside a transparent stagnant deionized water tank with a 45° tilt allowing the observation of sample surfaces with a horizontally mounted camera. Present air within the roughness grooves pre-submersion were referred to as "plastron". Visual plastron layer stability at different submersion depths over time was captured and quantified through processing the images of the plastron digitally. Plastron layers were distinctively visible thanks to their silver colored appearance to the camera. It has been concluded that increasing submersion depth decreases the lifetime of a stable plastron layer due to increased hydrostatic pressures. The longest achieved plastron lifetime was approximately 400 hours at the shallowest submersion depth of 35 cm. Through microscope imaging, presence of an initial 100 μm thick stable homogeneous air layer contained within the surface roughness protrusions was detected. However, as the air kept dissolving into the water, the substrate protrusions contacted water. This disrupted the homogeneity of the air layer and split the gas volume into bubbles residing on the roughness profile randomly. With the influence of increasing

Laplace pressure, those bubbles rapidly dissolved into the water leaving a very thin layer of plastron within secondary (hierarchical) surface structures. Combined with prior findings in literature Poetes et. al have concluded; keeping a stable gas layer on a super-hydrophobic surface is not thermodynamically feasible due to gas dissolution and Laplace pressures. However, the work covered so far only studied environments with no gas generation and hydrophobic texture profiles that are created randomly. Hydrogen evolution that comes with magnesium corrosion in addition to specifically designed and manufactured roughness patterns can possibly further improve the lifetime of a stable plastron layer.

Panchanathan [16], in their dissertation have dealt with similar gas entrapment phenomenon to serve a different functionality (drag reduction). In their work, plastron stability and recovery behavior are formulated based on Young, Cassie-Baxter and Wenzel models. It is concluded that; in order to keep a gas layer within the surface micro-texture, the change in the energy of the system (dE) caused by water-gas displacement at a small area (ldx) should be negative. Change in the energy of system is defined as:

$$dE = \gamma_{LG}(1-f)ldx + \gamma_{SG}(r-f)ldx - \gamma_{SL}(r-f)ldx \tag{12}$$

where r and f represent roughness coefficient and solid area fraction (Figure 2.9) respectively. By setting dE < 0 and combining equation (12) with equation (9), plastron recovery and stability condition is derived as:

$$cos\theta < -\frac{1-f}{r-f} \tag{13}$$

According to equation (13, as right hand side of the equation is always negative, the Young's contact angle (θ) always has to be larger than 90° in order to preserve and recover plastron within a roughness profile defined with r and f parameters. Young's contact angle is a

material property and very challenging to experimentally determine for certain materials due to surface imperfections and material heterogeneity [50]. Panchanathan have substituted the Young's contact angle (θ) with the receding contact angle measured on a smooth surface (θ$_{rec}$) to work around this issue while also claiming receding contact angle being a better representative for a plastron recovery mechanism that involves liquid being replaced by gas. Hence, following this substitution and rearrangement, equation (13 becomes:

$$r > 1 - \left(\frac{1}{cos\theta_{rec}} + 1\right)(1 - f) \qquad \forall\, \theta_{rec} > 90° \qquad (14)$$

Based on these formulations, Panchanathan has manufactured micro-pillared patterns on silicon wafer using photolithography followed by platinum coating that generates oxygen when contacts hydrogen peroxide. Finally, the micro-textures are coated with Teflon to render them hydrophobic. Si-Pt-Teflon surfaces were dipped into 4.5w% aqueous hydrogen peroxide solution to enable oxygen evolution off the surfaces. The micro texture with 150 μm trench depth, 50 μm pillar width and 100 μm trench width (f = 0.196, r = 3.356) have shown successful plastron generation and stability in submerged conditions. θ_{rec} angle was measured approximately 111° on a smooth Teflon coated silicon. Given all these parameters obeying equation (14 is very promising for a generalized plastron stability condition valid for any material. In conclusion, plastron (entrapped gas layer within roughness grooves) stability and recovery behavior are formulated based on Young, Cassie-Baxter and Wenzel models. They have found that in submerged conditions, surfaces with higher static contact angle and Young's angle tend to promote gas adhesion within the surface grooves (Figure 2.11). In other words, it is possible to tailor superhydrophobic rough surfaces based on

Cassie-Baxter formulations and stabilize and even regenerate a gas formation that acts as a barrier between the solid substrate and the liquid medium.
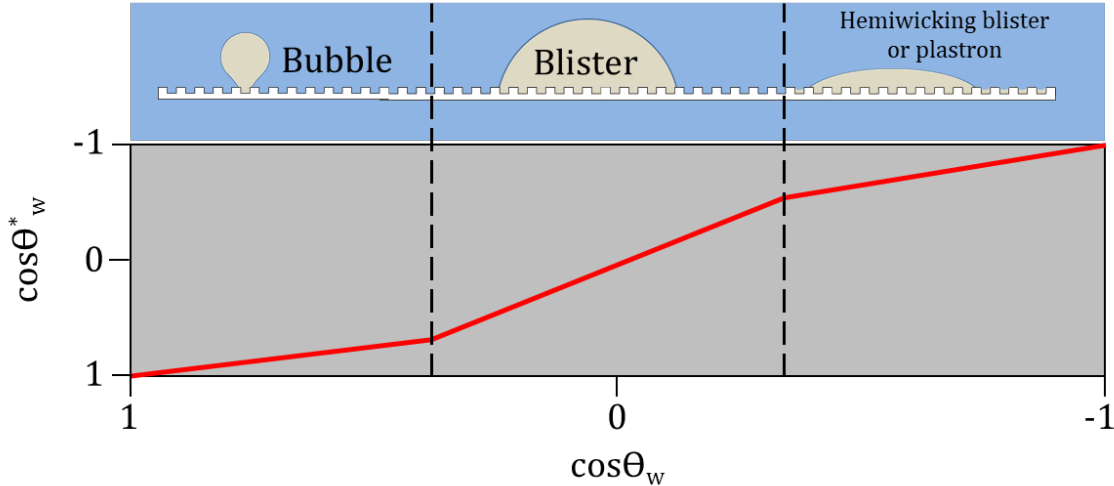
Figure 2.11 Panchanathan's [16] predicted state of gas bubble spreading on submerged textured surfaces based on the surfaces' static water droplet contact angle (θ^*_w) and Young's contact angle (θ_w) values. Surface wetting properties that fall on or below the plotted curve conforms the corresponding gas bubble state depicted above the plot. Hemiwicking blister or plastron state is preferred for corrosion buffering purposes.

2.4.2 Fabrication Methods to Influence Wetting Behavior of Solid Surfaces

Zhao et al. investigated ways of creating superhydrophobic textures by generating highly uniform pillar geometries on a solid surface. Silicon wafers were used as a substrate and dense pillared structures with 7 μm height and 2.7 μm diameter were created with the help of a photo resistive polymer and etching away the exposed areas with an etching agent. The resultant geometry yielded a superhydrophobic behavior without applying any coating which is an interesting improvement area that could be applied on metals [51].

Wang et al. investigated a two-step approach to generate superhydrophobic surfaces on copper. Copper foils were first dipped into a 30% and 20% volume fraction antiformin solutions with varying durations between 15 seconds and 20 minutes. The effect of volume fraction and immersion duration is observed with the trial of different volume fractions and

34

www.manaraa.com

durations. The resultant structure formed on the copper substrate was in the form of micro wires forming a thin CuO film over the surface. It was observed that with immersions durations higher than 2 minutes in 30% VF antiformin solution, thin wire structures started to coagulate and form bean sprout-like structures on the surface. All samples immersed in antiformin solution regardless of time and solution concentration have shown superhydrophilic behavior with contact angles lower than 8 degrees. Following the antiformin dipping, the samples were modified in 0.01 M ethanolic stearic acid solution for 15 minutes to lower the surface energy. With the stearic acid modification, all samples regardless of the immersion time and antiformin concentration, have shown superhydrophobic behavior with contact angles higher than 155 degrees. Wang demonstrated a time-saving, practical, and pollution friendly method to generate a superhydrophobic coating on a metal substrate [52].

Sun et. al [53] have incorporated Cassie-Baxter and Wenzel wetting models to control a water droplet's motion over a hydrophobic roughness gradient created on silicon wafers. Parallel grooves were etched by using a short pulsed (pulse duration is not stated) KrF laser with 248 nm wavelength and 100 Hz repetition rate. Following the laser etching, silicon substrate was coated with fluoroalkylsilane (FAS) in order to reduce surface energies that renders hydrophobic behavior. The distance between parallel grooves were increased gradually along the surfaces (creating a roughness gradient) to observe the effects on apparent contact angles—in addition to droplet movement effect which is outside of the scope of this dissertation. Hydrophobicity was successfully generated through pre-calculated roughness pattern dimensions through Wenzel ((10) and Cassie-Baxter (equation (11) models. All parallel etched grooves had a depth of 20 μm with varying width and

spacing. It was observed that, near-millimeter scale groove spacing causes the roughness profile to yield Wenzel wetting mode in which droplet infiltrates into the grooves. As the groove spacing on Wenzel surfaces was increased, apparent contact angles were decreased from 144° to 126° across the roughness gradient (Figure 2.12a). Micrometer scale groove spacing has yielded Cassie-Baxter type wetting model in which the droplets sit on a composite silicon-air surface. However, on Cassie-Baxter surfaces, increasing groove spacing has caused an increase in apparent contact angles from 150° to 162° across the roughness gradient (Figure 2.12b).
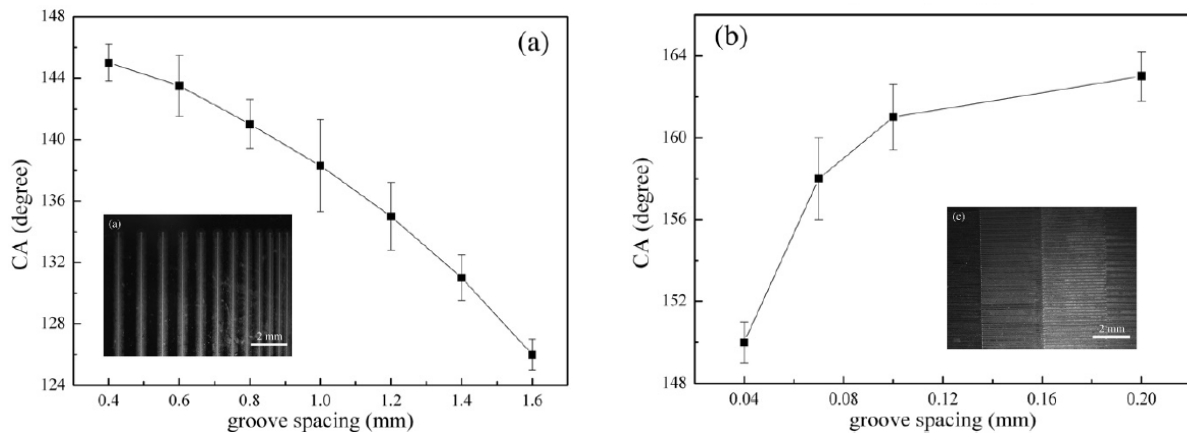
Figure 2.12 Contact angle changes with increasing groove spacing on Wenzel (a) and Cassie-Baxter (b) surfaces. [53]

One interesting study by Luo et. al [54] investigates manufacturing of a hydrophobic micro-texture pattern without any additional chemical treatment reducing surface energy.

Square micro-pillared patterns were etched on polished 316 stainless steel surfaces using a short-pulsed excimer laser (248 nm wavelength, 6 ns pulse duration, 150 Hz pulse repetition rate, 2.5 J.cm^{-2} energy density). Square pillars had a constant width of 50 μm and height of 8 μm while the trenches between pillars had varying widths between 10 μm and 50 μm. While smooth unetched surfaces had a contact angle of 68.5°, all patterned surface types had contact angles larger than 120° without any application of chemical surface modification. It was also noted that contact angles could be increased by 10° with an amorphous carbon deposition on the surfaces.

Chapter 3: Effects of Laser Ablation Parameters to Pattern

High Purity Magnesium Surfaces[1]

In this research in order to create surfaces with different wetting properties laser ablation was employed. To achieve a desired micro-structured texture on magnesium surfaces, a method had to be developed by an additional study. In this chapter the methods and results of the study on laser ablation parameters and their effects on magnesium surfaces is documented.

3.1 Introduction

Surfaces that have water repelling properties resulting in a droplet contact angle larger than 150° are defined as super-hydrophobic surfaces [51]. Mimicking nature to create super-hydrophobic substrates has been attracting widespread attention in the past decade [56]. Unique surface features of the lotus plant's leaves is one of multiple examples for super hydrophobic behavior seen in nature [57]. By replicating uniform repetitive patterns like pillars or holes carved on a solid substrate, it is possible to create hydrophobicity on materials like silicon, stainless steel and aluminum with methods such as etching, lithography and laser machining [51, 58, 59].

---

[1] This chapter is published as an ASME proceedings paper [55]   Y. E. Yayoglu, N. D. Gallant, R. Toomey, and N. B. Crane, "Effects of Laser Ablation Parameters to Pattern High Purity Magnesium Surfaces," in *ASME 2019 International Mechanical Engineering Congress and Exposition*, 2019.

Promotion of hydrophobic behavior on patterned solid substrates is explained by Cassie and Wenzel's wetting model [46, 47]. The dimensional ratios between the surface grooves' depth and width governs the wetting and non-wetting behavior. Hence, it is crucial to have the control ability on surface pattern dimensions in all three axes to achieve super-hydrophobicity based on Cassie and Wenzel's theoretical calculations.

Having super-hydrophobic and hydrophobic properties on a surface has been associated with a resultant corrosion resisting behavior on several materials in literature [33, 60, 61]. Due to magnesium's highly reactive behavior in corrosive environment, several studies adopting surface modifications creating hydrophobic magnesium surfaces to slow down its degradation rates are currently being conducted [44, 62, 63].

It is challenging to achieve desired uniform patterns on metal substrates due to limited micro-machining options compared to polymer or silicon-based substrates. Laser ablation is one of the promising methods that allows rapid, repeatable and high precision machining on metal substrates. Laser ablation is defined as material removal off the surface of a solid substrate due to thermal stresses and surface vaporization caused by laser radiation [64]. However, each metal substrate has a different response towards laser ablation due to their different material properties. It is important to gain material-specific knowledge on laser radiation response in terms of removed material amount and resultant

38

cavity geometry. In this study, the effects of various laser parameters such as average power, number of repeated scans and amount of scan overlaps to ablate micrometer scale trenches on polished pure magnesium substrates are observed for pulsed laser machining. The resultant data covering a wide range of parameters is used as a reference to generate pillared structures with desired dimensions. One example of patterned surfaces on pure magnesium created by laser ablation can be seen on Figure 3.1. The pattern has 100 x 100 μm^2 square pillars with 30 μm height and 30 μm spacing in between pillars. They were created by crisscrossing trenches with the help of the outcome of this study.
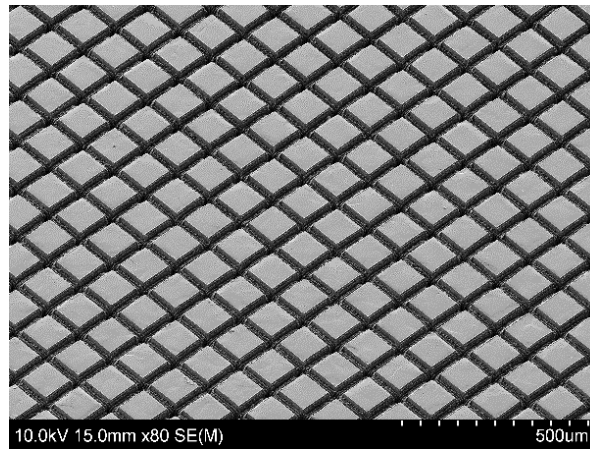
Figure 3.1 Square pillars ablated on polished pure magnesium substrate by ablating trenches in a grid pattern.

3.2 Experimental Methods

A large magnesium plate (99.9999% purity, Magnesium Elektron) with 2.1 mm thickness was cut into 10 x 10 mm^2 sized square coupons using wire EDM process. Each coupon was polished manually on a rotary metallographic grinder/polisher (Saphir 320, ATM) with 600, 1000, 1200 grit SiC paper using de-ionized water as coolant/lubricant, then polished on a cotton buffing pad using water soluble diamond lapping slurry (4857A41, McMaster-Carr) containing 1 μm diameter abrasive grains (1800 equivalent grit size).

Between each grinding and polishing step, coupons were rinsed with 99% isopropyl alcohol, then blow dried under pressurized air at room temperature. Due to magnesium's high vulnerability towards moisture, all coupons when they were not being processed, were stored in a desiccator containing silica beads under vacuum.

A high repetition rate picosecond laser system (Super Rapid-HE, Coherent) was used to ablate micro-trenches on polished magnesium surfaces. An integrated print stage numerically actuated in x, y and z directions of a micro dispensing 3D printer (Tabletop, nScrypt) was utilized to create the ablated geometries. The moving stage had a precision of ±1 µm in all three directions. Laser beam had a wavelength of 355 nm and 500 kHz pulse frequency. The pulse length was approximately 15 picoseconds. Laser scan feed rate was kept constant at 30 mm/s for all ablation steps. Varying feed rates can be considered to expand the scope of the study in future publications.

The industrial picosecond laser used in this study utilizes an objective that has a focal range of around 100 µm. Meaning there is a ±50 µm vertical distance from the focal point where the beam diameter is approximately 6 µm. This means the substrate has to be parallel to the x-y stage with less than 100 µm between its lowest and highest points in order to keep the beam diameter consistent (within 6 to 12 µm) during ablation at any point on the surface. Since the coupons were polished manually by hand on a rotary grinder, there was a concern of surface parallelism relative to the x-y stage. To ensure the coupon surface thickness was within that tolerance envelope, a proximity laser sensor (LK-H082, Keyence) was used to measure the flatness of the square coupon relative to the x-y stage on all four corners and its geometric center. Those five measurements were averaged, and the thickness deviation was verified to be less than 50 µm to ensure a consistent laser beam diameter that did not go over

12 μm. If the polished coupon thickness deviation was larger than 50 μm, the sample was discarded and replaced with a new one. Coupons were fixed on the x-y stage with the help of a double-sided tape (Scotch, 3M) on their bottom faces and all thickness measurements were done with double sided tape under the coupons.

In this study, multiple laser ablated micro trenches were generated by varying the following laser ablation parameters: average laser power as measured using a laser power meter (3A, Ophir-Spiricon, LLC), number of scans and scan overlap ratio. The impact of these parameters on cross sectional trench geometry profile and ablation depth is observed.

Between the laser ablation and consequent cross sectioning processes, each sample coupon was dipped in boiling Chromium Trioxide and Silver Chromate solution for 60 seconds in order to remove the generated oxide layer during laser ablation covering the bare magnesium substrate according to the ASTM G1-03 standard [29]. Following the oxide layer removal, samples were rinsed in de-ionized water, sonicated in 99% isopropyl alcohol for five minutes and blow dried under pressurized air at room temperature. The differences on the trench surface quality before and after oxide removal process can be seen on Figure 3.2.
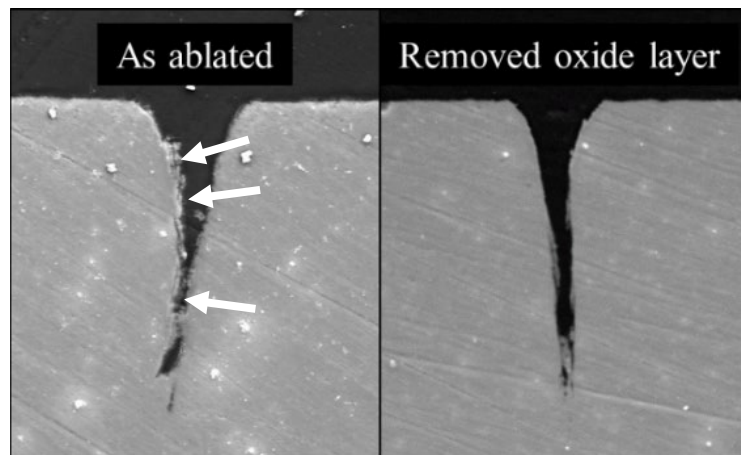
Figure 3.2 Cross sectional SEM images of two separate trenches created with identical ablation parameters with and without oxide layer. Effect of oxide layer removal on ablated

trench surface quality can be seen on the image on the right. Oxide formations creating roughened trench walls are shown with arrows.

Cross sectional views of the trenches were achieved by embedding the ablated coupons vertically in metallographic cold-mount epoxy (01300-XX, SPI Supplies) using a cylindrical polymer mold. Embedded coupons then were cut with a low RPM diamond saw orthogonally along their centerlines (5 mm off the coupon edge), followed by the same grinding and polishing procedure explained above revealing the cross sectional trench geometry to be observed with scanning electron (SU-70 SEM, Hitachi) or optical (VHX-6000, Keyence) microscopes.

3.2.1 Average Laser Power

The picosecond laser used for the study has adjustable average power levels ranging from zero to 2.3 watts at 355 nm wavelength and 500 kHz pulse repetition rate. Therefore, it was crucial to pinpoint an optimal power value that would remove/ablate enough material with good precision in the shortest time without damaging, melting, igniting or changing the chemical properties of the substrate. In order to find an optimal average power, cross sectioning was done on magnesium coupons ablated with different laser powers ranging between 0.3 and 2.3 watts. The lowest power setting at which the laser beam was able to remove detectable amounts of solid material off the surface at 500 kHz pulse frequency was 0.3 watts.

In order to assess repeatability, three identical 10 mm long trenches were ablated side by side with 50 µm spacing at a given power level. Average power was increased with small increments for the additional trench groups of three up to 2.3 watts. Using SEM imaging and ImageJ software, average depth and width data of each trench group for a given average laser power is collected.

42

3.2.2 Number of Scans

An alternative method for achieving a predetermined trench depth without increasing the average laser power is scanning along the same path multiple times to yield deeper trenches at each consecutive pass. This is desirable since extreme power levels will cause heat accumulation hence melt or ignite the substrate material causing uneven surfaces or destruction of the sample. Lower laser power is also preferred to achieve smoother trench walls.

In order to observe the effect of number of scans along the same path, similar to the previous step, three identical 10 mm long trenches were ablated side by side with 50 µm spacing on the coupon at a selected power level. More trench groups of three were then ablated by increasing the number of scans with increments of one up to six passes resulting in six groups of trenches ablated at the same average power level. The same ablation procedure is repeated for all power levels between 0.3 and 2.3 watts (Figure 3.3). The maximum number of scans was limited at six since more scans along the same path would increase the process time causing infeasibility at a scan speed of 30 mm/s. Using SEM imaging and ImageJ software, average depth and width data of each trench group for a given average laser power and number of scans was collected.
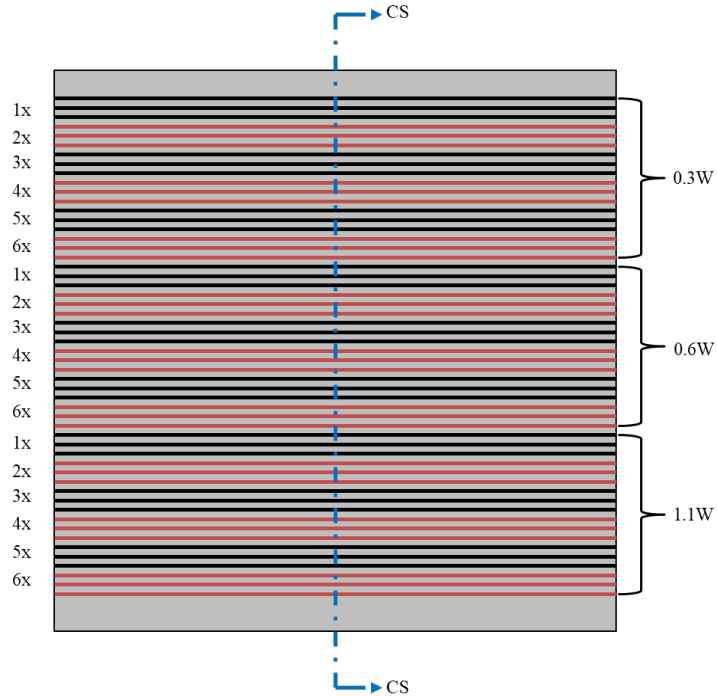
Figure 3.3 Scan pattern on 10 x 10 mm2 magnesium coupon to be cross sectioned to see the effects of varying number of scans and average laser power on ablated trench geometry. Each group of three horizontal lines represents trenches ablated by denoted parameters on the left (number of scans) and right (average laser power) side of the coupon. Same pattern was also used to test 1.5, 1.9, 2.0 and 2.3 watts of power levels (not shown on figure).

3.2.3 Scan Overlap Ratio

The laser beam has an approximate beam diameter between 6 and 12 μm as discussed above. Hence it is required to have multiple scans side by side to have ablated trench widths larger than 12 μm. Since the beam diameter is assumed to be a constant that cannot be adjusted, overlapping the line scans creating the ablated trenches is the only solution to have control over trench width; hence the need of an overlap percentage parameter arises. Another cross-sectional observation has been done on ablated polished magnesium substrates to see the effects of overlapped multiline scans with 0, 25, 50 and 75 percent overlap (Figure 3.4) with increasing number of passes.
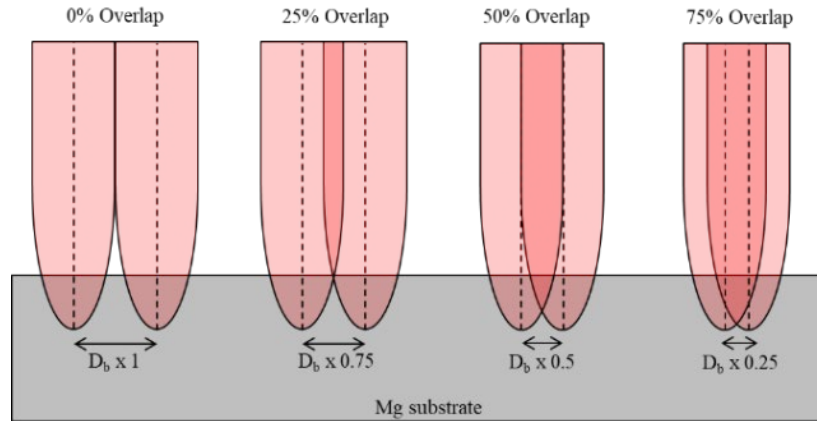
Figure 3.4 Different laser scan overlap ratios used to observe their effects on wider trench geometries. (D_b: laser beam diameter)

One polished magnesium coupon was prepared and 100 μm wide trenches were ablated side by side with increasing number of scans between one and six passes per each overlap ratio. Multiple trenches were overlapped at a given ratio until a trench width of 100 μm was achieved for easier observation under optical microscope. A single average power level of 1.5 watts was chosen since the effect of overlapping on trench geometry is expected to be similar regardless of the intensity of the laser beam.

Using optical microscopy and ImageJ software, average depth, width and wall angle data of each trench group for a given average laser power, number of scans and overlap ratio is collected from the cross sectioned samples.

3.2.4 Focal Distance Compensation Due to Material Removal

In addition to the overlap percentage, the effect of focal distance compensation parameter was added at this stage of the study. As discussed earlier, the laser objective has a focal range of ± 50 μm before the laser beam grows larger than 12 μm in diameter or simply goes out of focus in other words. As trenches get deeper at each consecutive scan, the laser

will de-focus since the objective stays at the same height relative to the x-y stage. This will cause de-focusing issues as trenches reach a depth of 50 μm or more.

In order to overcome this issue, we repeated the 100 μm trenches by ablating in a similar fashion explained in Section 2.3 (also at 1.5 watts of average power) while also incrementally lowering the laser objective down by a predetermined distance along z axis right before a consecutive scan was initiated in order to keep the laser beam diameter constant during each scan. The compensation amount along the z axis was determined from the outcome of the process explained in Section 2.2 for trenches ablated at 1.5 watts of power. According to the data (Figure 3.5), the first single scan caused a material removal resulting in an approximately 30 μm deep trench, hence 30 μm of compensation was chosen.

Using optical microscopy and ImageJ software, average depth, width and wall angle data of each trench group ablated with a focal distance compensation at a given average laser power, number of scans and overlap ratio is collected from the cross sectioned samples.

3.3 Results and Discussion
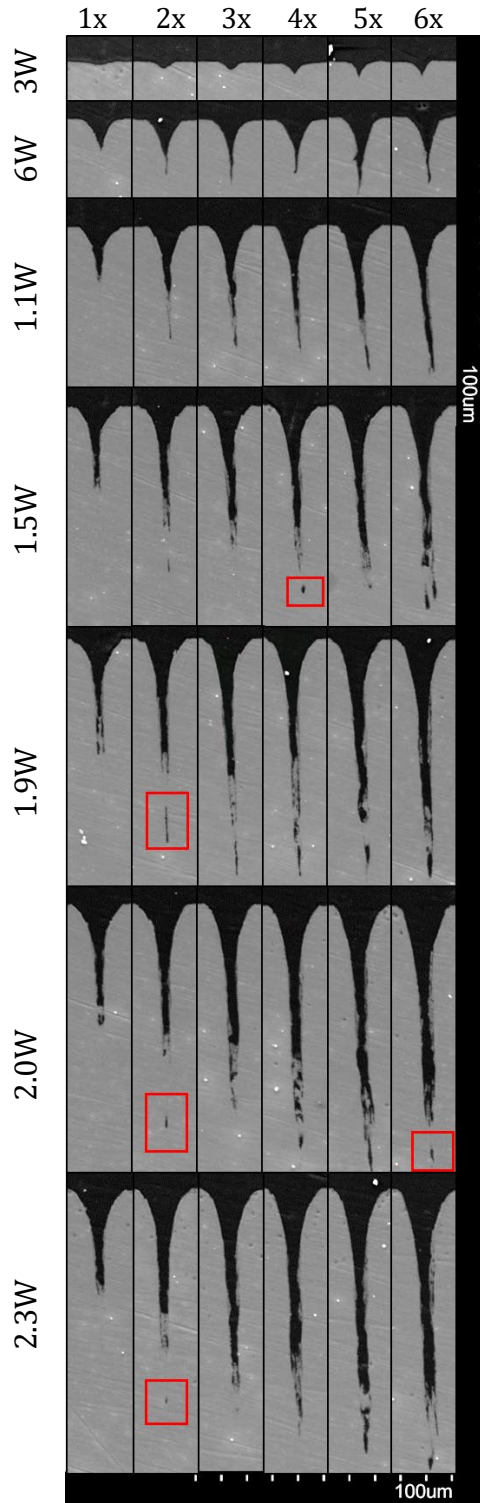
Figure 3.5 Cross section of trenches ablated at given laser power (rows) and number of scans (columns). Red squares show cases of re-solidified molten material encapsulating ablated cavities during process.

Ablating trenches with multiple passes at lower power levels is desirable since it is the least destructive way of creating deeper trenches avoiding substrate meltdown. Depth data for increasing number of passes and average laser power measured from the SEM images can be seen on Figure 3.5. Measured trench depths are shown as bar graphs on Figure 3.6. Each bar shows the average cross-sectional depth of three separate trenches ablated with same parameters (only one shown on Figure 3.5) given on the graph.
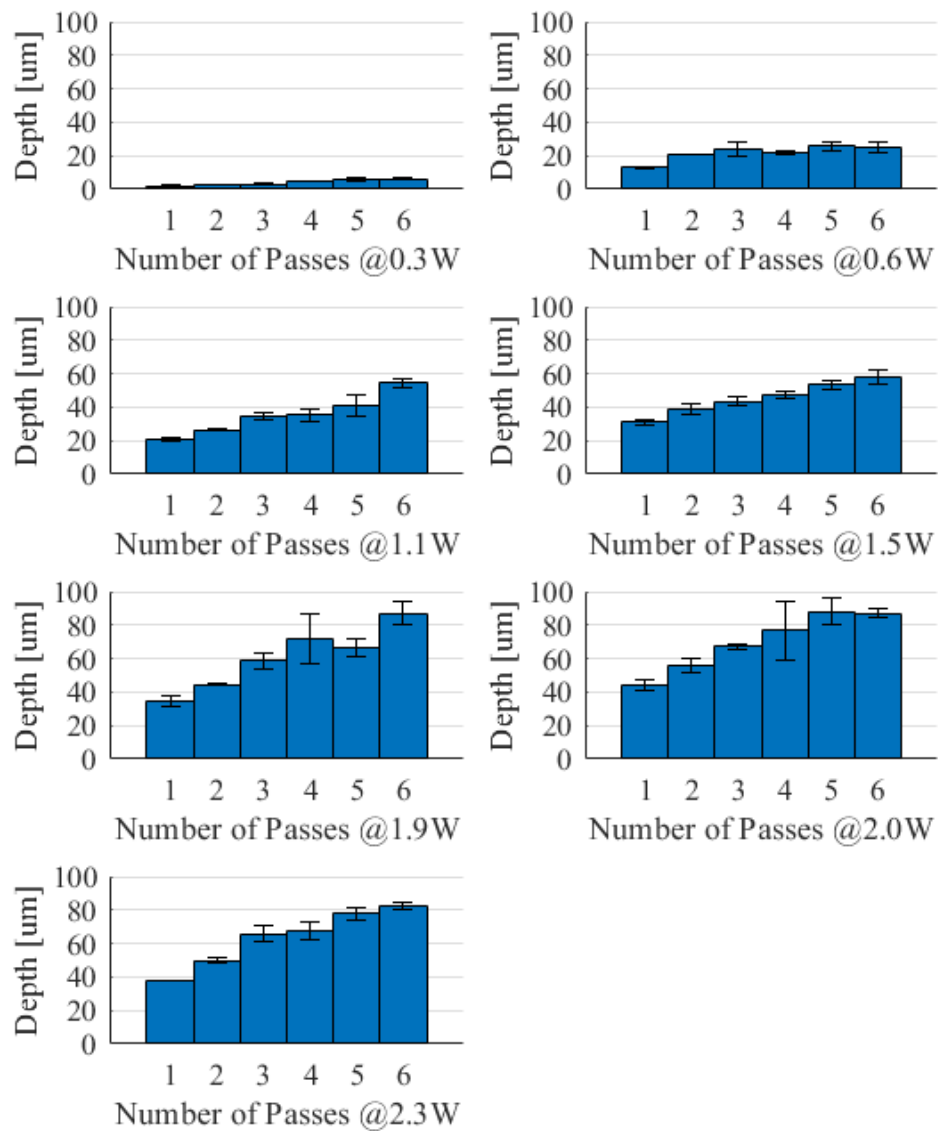
Figure 3.6 Trench depth vs number of passes at a given average laser power.

As expected, trench depths increased in a nearly linear fashion as the number of passes increased at average laser power levels less than 1.9 watts. With average laser power levels of 1.9 watts and above, the magnesium substrate melted and accumulated at the bottom of the trenches (see Figure 3.5) due to excessive residual heat during ablation as the number of scans increased. In some cases, with increased power levels and number of scans, the trench depth decreases. This may be due to molten material that re-solidifies at the base trapping pores. This accumulation caused a tapering effect on the linear response of trench depths towards increasing number of scans. Each trench also had V-shaped cross section as expected due to the laser beam's Gaussian shape that gets narrower closer to its tip where it hits the substrate. As the beam gets narrower, more power per area is exerted on the substrate hence it causes deeper ablation at the centerline of the trenches.

Second cross-sectional observation was done on wide trenches (100 μm in width) ablated by overlapping scan lines with varying ratios from 0% to 75% as shown on Figure 3.4 above. Imaging was done with an optical microscope on cross sections 3.31, 4.31, 7.44 and 7.70 mm away from the edge of the square magnesium coupon. Cross sections are perpendicular to the ablated trenches. Only images from the cross-section 4.31 mm away from the coupon edge are shown on Figure 3.7 with corresponding overlap ratios and number of scans. The averaged width and trench wall angle data from all four cross sections is presented as bar graphs on Figure 3.8 and Figure 3.9 with respective laser scan parameters.

It can be seen on Figure 3.7 that, even when the scans are overlapped, due to the Gaussian shape of the laser beam it was not possible to achieve perfectly flat trench valleys with the scanning method adopted in this study. As the beam did not have a straight

cylindrical profile (i.e. beam diameter is smaller where it hits the substrate, hence more power per area is exerted) it was inevitable to get narrower micro-trenches at the bottom of all 100 μm wide trenches. This issue can be observed clearly on trenches ablated with low number of scan repetitions regardless of the overlap ratio. An ablation pattern involving scans in both orthogonal directions should be adopted in a future study to overcome this issue.

Another observation on Figure 3.7 was the unintended spike shaped valleys at higher number of scans and/or higher overlap ratios (especially at 75%). This phenomenon is thought to be caused by the temperature gradient created during ablation. As the ablation process moves on to the consecutive overlapping line scan, at higher overlap ratios the substrate does not have enough time and distance from ablation zone to cool down before the next scan step initiates. Especially at higher overlap ratios and scan repetitions the substrate material's ablation rate overshoots the expected amount causing uneven profiles at the trench base. Excessive ablation behavior accumulated on one side of the trench also caused unwanted meltdown of material causing it to flow into previously created grooves and smoothing out the further end of the intended trench. This effect can be observed clearly on frames at the bottom right corner of Figure 3.7. Using lower average laser power without unnecessary overlaps at fewer scan repetitions in the future is suggested to eliminate this problem.

Data presented on Figure 3.6 shows, at 1.5 watts of average laser power, a single line scan yields a trench depth of 30 μm in average. Since at this step of the study, 1.5 watts of power was being used, 30 μm compensation along vertical direction (z axis) was tested. The effect of keeping the laser beam constantly in perfect focus was observed by lowering the

laser objective closer to the substrate by 30 μm as the trenches get deeper at each scan repetition.

Figure 3.7 shows the cross-sectional images of 100 μm wide trenches ablated with respective overlap ratios, scan repetition numbers with and without 30 μm focal distance compensation. There was no significant improvement in trench geometries with focal distance compensation.

Since the bottoms of the trenches were irregularly shaped on some cases, three depth measurements were taken on both ends and the center of the bases of all trenches to be documented on Figure 3.8. According to Figure 3.8, regardless of focal distance compensation presence, the overall average depth of the wide trenches (except the highly deformed trenches at high overlap ratios and number of scans) was in parallel with the depth values presented on Figure 3.6 for single line scans at 1.5 watts of power.
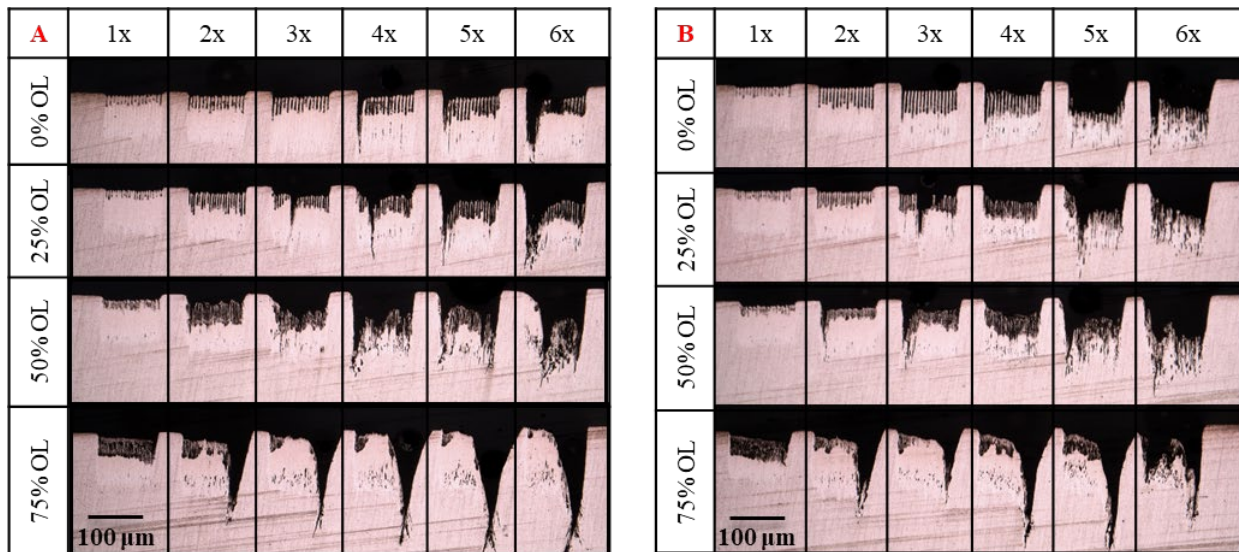
Figure 3.7 Cross sectional views of 100 μm wide trenches ablated with given overlap ratio (rows) and number of scan (columns) (A) without focal distance compensation, or (B) with 30 μm focal distance compensation at 1.5 watts of laser power.
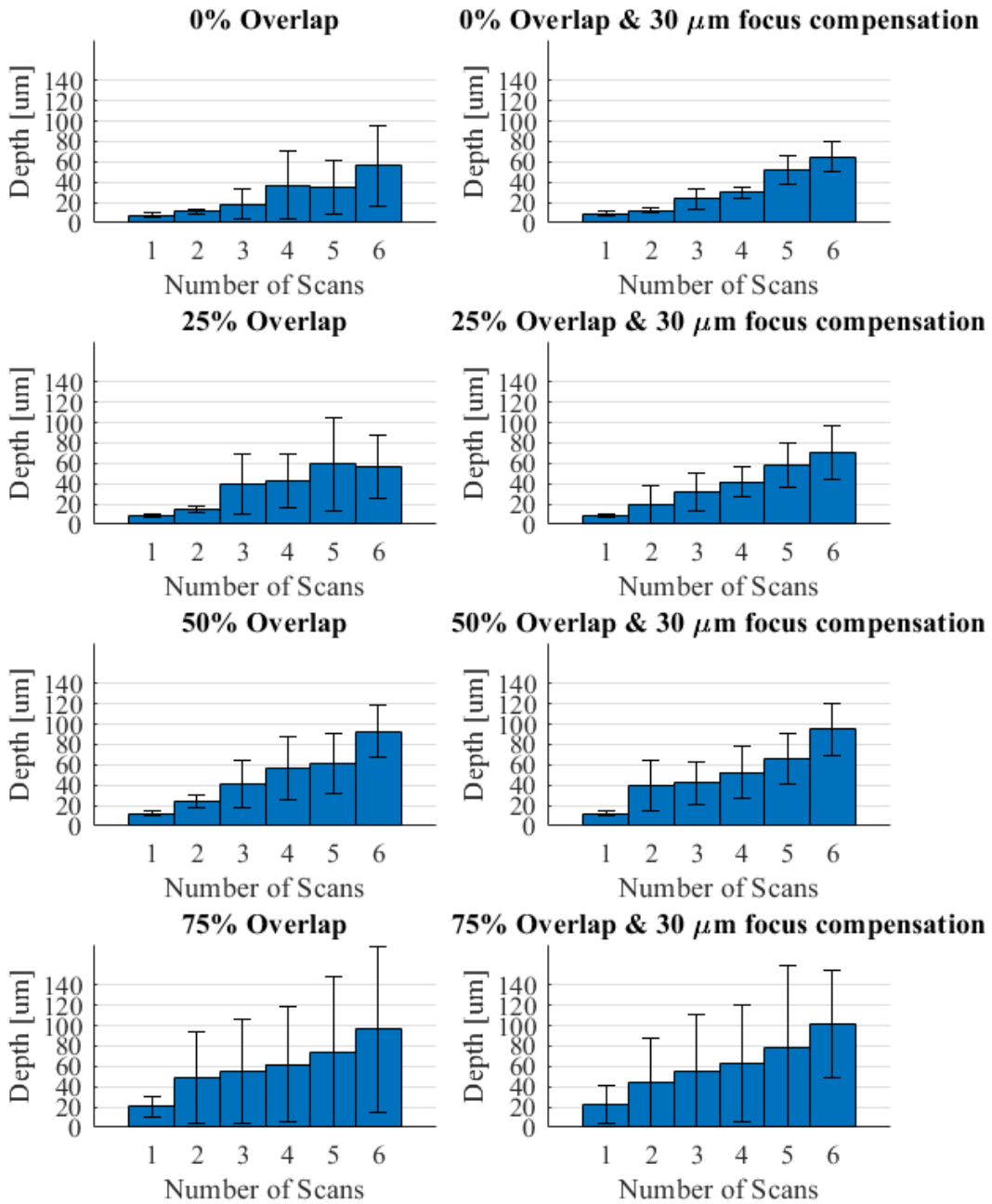
Figure 3.8 Depth vs number of scans at given overlap ratio with and with and without focal depth compensation at 1.5 watts of laser power.
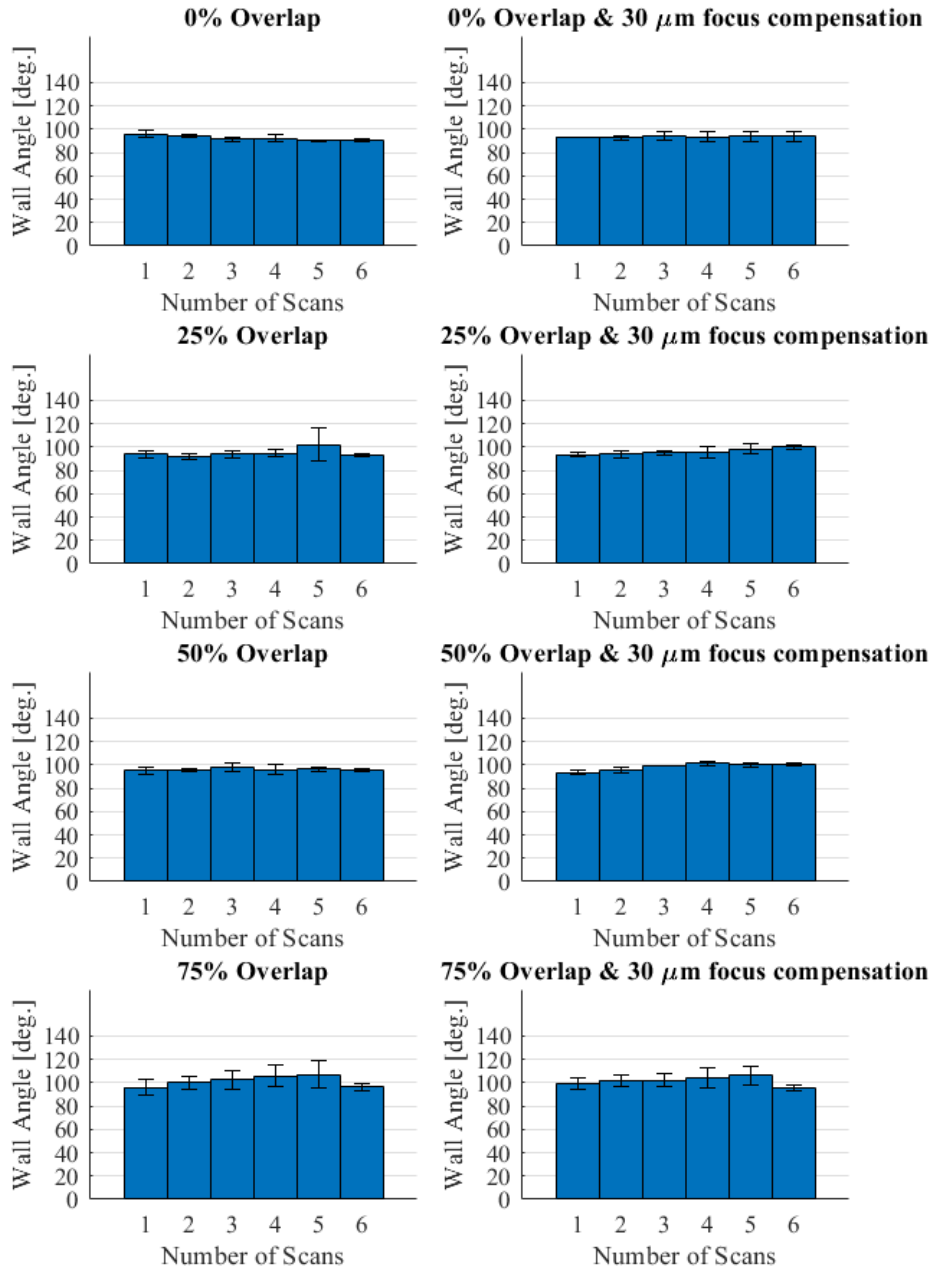
Figure 3.9 Trench wall angle vs number of scans at a given overlap ratio with and without focal depth compensation at 1.5 watts of laser power.

The depth of the micro trenches present at the bottom of main trenches was not accounted for in depth measurements since their widths were less than or equal to 10 μm. As expected, the large error bars denote the irregularities on the geometry of the associated

trenches especially the ones ablated with an overlap ratio of 75%. The focus compensation does appear to have reduced the variation in the depth at 0 and 25% overlaps.

The angle between the trench wall surfaces and the polished unablated flat surface of the substrate was defined as the wall angle. Wall angles of each trench were measured from the optical microscope images and there was no significant variation in the angle values. Most trenches had wall angles between 90 and 100 degrees. Having focal distance compensation at each scan did not affect the wall angles. Higher angles were observed on deformed trenches at higher overlap ratios as expected from cross sectional images.

3.4 Conclusion

Using lower laser ablation power settings with multiple number of repeated scans is the least destructive and most efficient method to achieve a desired trench depth. In order to achieve deeper grooves, increasing the number of repetitions is preferred over increasing the average laser power. It was also possible to achieve wider trenches by overlapping single line scans. An overlap ratio up to 50% for a scan repetition of less than five was desirable to achieve trapezoidal trench cross sections. However, the scanning pattern needs to be changed in order to achieve smooth trench bases. Lowering the objective in order to preserve laser focus as the trenches get deeper had no significant effect on any of the cross-sectional geometries.

Chapter 4: Corrosion Rate Reduction with Hydrophilic and Super-Hydrophobic Micro-Textured Surfaces: Effect of Oxidation

4.1 Introduction

Many studies in literature have shown improved corrosion resistance with increased hydrophobicity on metal surfaces [60, 61, 65-67] and a few similar experimental works were shown on magnesium/magnesium alloys [68-70]. These studies primarily focus on two approaches that enhance the hydrophobicity by altering the surface structure: (1) creating a hierarchical roughness pattern that induces super-hydrophobicity, or (2) treatment with agents that reduce surface energy. The theory behind employing hydrophobic behavior towards corrosion resistance is based on three phase solid-fluid interaction happening on the surface of a submerged magnesium specimen (Section 2.4). In theory, the optimal hydrophobic surface texture would promote adhesion of gas within and over the surface features, hence yielding a hydrogen gas layer over the surface, evolved from the oxidizing Mg substrate itself. The gas layer would act as a buffer, inhibiting extremely rapid in-vitro degradation seen on smooth magnesium surfaces.

This method attracts wide range of interest for biodegradable medical implant applications as well due to the multi-functionality of the textured surfaces compared to coating the substrate with a possibly biocompatible hydrophobic treatment. However, the effects of the applied hydrophobic treatment on corrosion behavior is debatable since the

coating layer itself might act as a corrosion protective barrier regardless of the effectiveness of hydrophobicity against corrosion.

In this chapter we evaluate a method to slow down the corrosion rate of a pure magnesium substrate in a saline environment. Pillar shaped microstructure patterns with different dimensions were created on flat polished surfaces. In order to assess the necessity of hydrophobic treatments in addition to micro-patterning, the corrosion rates of textured surfaces with and without a biocompatible hydrophobic treatment are compared to polished pure magnesium.

As mentioned in section 2.1.1, solely relying on electrochemical measurements may not be definitive to assess corrosion behavior on magnesium, therefore, corrosion protection performances of different textures were assessed through submersion tests first, then supplemented with electrochemical impedance spectroscopy (EIS) method.

4.2 Experimental Methods and Setup

4.2.1 Sample Preparation

Magnesium coupons were embedded into metallographic epoxy (01300-XX, SPI Supplies) using cylindrical molds exposing an area of 10 x 10 mm² for ease of handling as well as keeping the exposed area constant throughout experiments (Figure 4.1). Each resultant puck face with exposed magnesium surfaces was polished and stored in dessicator that prevents air induced oxidation using the as explained methodology documented on section 3.2.
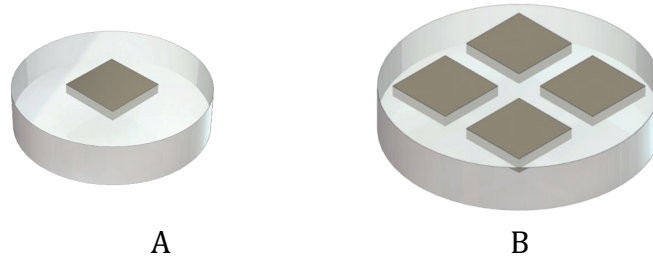
Figure 4.1 Pure magnesium sample coupons embedded in metallographic epoxy using 1.25 in (A) and 1.5 in (B) diameter molds.

Using the outcome of the study documented in Chapter 3:, pillar shaped micro-textures were patterned via laser (355 nm wavelength, 500 kHz pulse repetition rate, 1.5 W average power) on the exposed magnesium surfaces. Equally spaced ablated trenches orthogonally in vertical and horizontal directions (Figure 4.2) formed square micro-pillars. Each trench was created by ablating multiple adjacent lines side by side, resulting in various trench widths (T) on different samples. Trench depth was also changed by increasing or decreasing the number of laser scan repetitions. Trenches got deeper with each consecutive scan. Micro-structures tested can be seen in Appendix. All ablated trenches had rectangular profiles with side wall angles approximately vertical to trench bases.
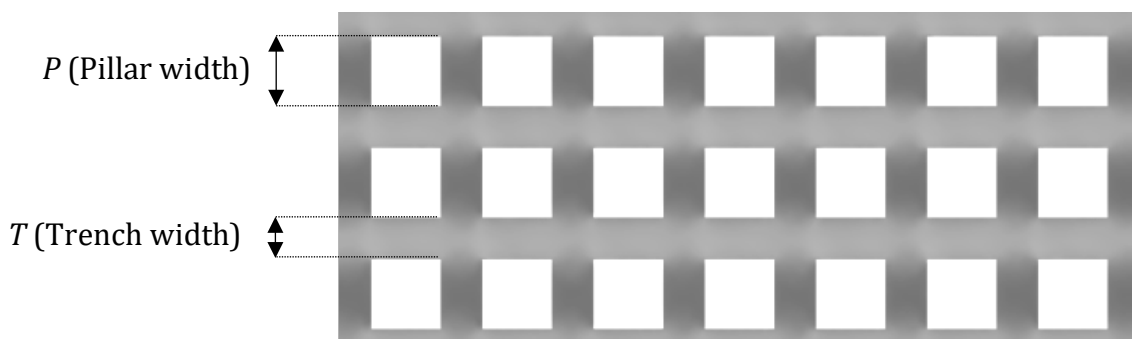
Figure 4.2 Top view of ideal square pillar pattern created by ablating trenches orthogonally (3D rendered image)

4.2.2 Surface Morphology and Wettability Measurements

Scanning electron microscopy (SU-70, Hitachi) was used to image the micro-structures created on the pure magnesium samples. SEM images were taken from a vertical view above the samples without any tilt and from an isometric view by tilting the sample stage by 42 degrees to give a visual idea on the height of the micro-pillars. Pillar widths (denoted by P parameter) were measured using ImageJ (Version 1.46r) software from the SEM images of the top views of micro-patterns.

The dimensions of the micro-structures were measured with a non-contact optical profilometer/interferometer (Wyko 9100NT, Veeco). Trench depth measurements were taken from six different spots on each sample and the average value was used to represent the trench depth denoted by the parameter 'D'. This method can be applied to all test samples since it is non-destructive but may not detect narrow, deep trench sections seen in some cross sections, especially if they are curved as seen in Figure 3.2.

Static contact angle measurements were taken on all samples using a contact angle goniometer consisting of a bright light source and a high-resolution camera. De-ionized water droplets with 10 µL volume were placed on the surfaces using a syringe with an automated pump. Three measurements were taken on each sample at separated areas on their surfaces. Contact angles were digitally measured using ImageJ (Version 1.46r) software with Drop Snake (EPFL) plugin.

4.2.3 Oxide Layer Removal

Since laser ablation is a thermal process, there was significant amount of oxidation present on the pure magnesium substrate after surface patterning. Besides a possible shielding behavior, the effects of a thick oxide layer on corrosion performance is

58

unpredictable due to the non-uniform thickness and the added roughness that comes with it. In order to remove the oxide layer, standard ASTM G1 procedure for oxide removal [29] specific to magnesium was employed. Each textured sample was dipped for one minute into a boiling aqueous solution containing concentrations of 15 w.% chromium trioxide (CrO_3) and 1 w.% silver chromate (Ag_2CrO_4). Subsequently, samples were rinsed with de-ionized water, sonicated in 99% ethanol for five minutes, then blow dried under pressurized air at room temperature to be stored in a desiccator under vacuum.

The effect of oxide layer cleaning on surface morphology can be seen in Figure 4.3 below. Visible reduction of oxide particles on and in between pillars was observed after oxide layer cleaning process. More detailed analysis incorporating the EDS measurements on the effectiveness of the oxide cleaning process can be found in section 4.3.3.

A   **B**
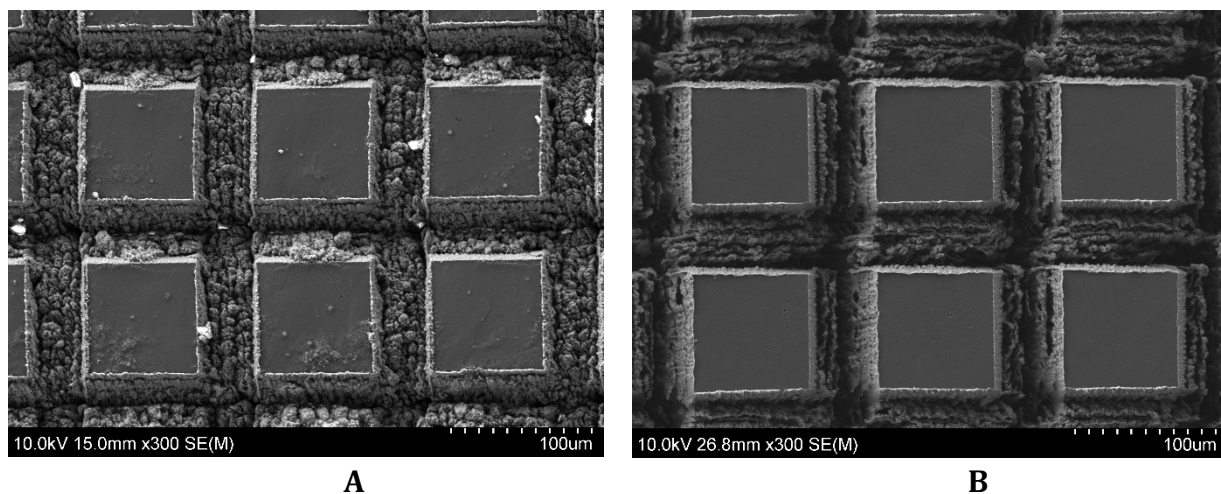
Figure 4.3 SEM images of micro-textures before (A) and after (B) oxide layer removal process.

Cross sections of the microstructures were analyzed via EDS to characterize the oxidation before and after oxide removal. Effects of oxide removal on corrosion rates were quantified with controlled electrochemical measurements to assess the necessity of the

59

oxide removal process in surface preparation. It was concluded that there was minimal effect of the oxide removal.

4.2.3.1 Surface Composition and Contamination Assessment

Elemental compositions of sample surfaces were determined using EDS tool (EDAX, Hitachi) attached to the SEM (SU-70, Hitachi). Three random, non-overlapping areas on each area of interest were selected to gather EDS data. Lowest possible magnification of 30x was used in order to detect composition of an area as wide as possible. Sample stage was tilted 30 degrees to allow data collection with the EDS detector. Each quantified area of interest was also imaged via SEM at the given magnification and stage tilt.

EDS measurements were taken on a representative sample from each smooth and patterned surface types tested to ensure corrosion process was only being influenced by pure magnesium surface microstructure geometry without secondary interferences such as impurities and process related residue.

4.2.4 Stearic Acid Modification (SAM)

For achieving hydrophobic behavior, some of the microstructures were modified by submerging them in 0.05 mol/L ethanolic stearic acid (Hystrene 5016/Food grade - NF/USP, Duda Diesel) solution for 1 hour in order to reduce their free surface energies. The stearic acid submersion is performed after the oxide removal in the cases where the oxide was etched away. Following the stearic acid solution submersion, samples were rinsed with de-ionized water and blow dried under pressurized air. Resultant patterned surfaces after stearic acid treatment had hydrophobic properties. Hydrophobicity was verified through contact angle measurements. All samples without the stearic acid treatment were expected to have hydrophilic properties.

4.2.5 Submersion Test Setup

Corrosion resistances of samples with varying microstructure dimensions were measured under submersion conditions. The corrosive medium was 0.9 w% saline (salt - water) solution that matches the salinity of human blood plasma [71]. Each sample was submerged in the saline solution and optical microscope images were taken over the course of at least 7 hours.

Imaging was done using an optical microscope at low magnification in order to observe all samples simultaneously. One relatively high magnification observation was done on sample P100-T35-D30-B in order to see gas generation inside the trenches until the view was obstructed by corrosion byproducts.

USB Microscope

Petri dish
Saline
Mg embedded epoxy
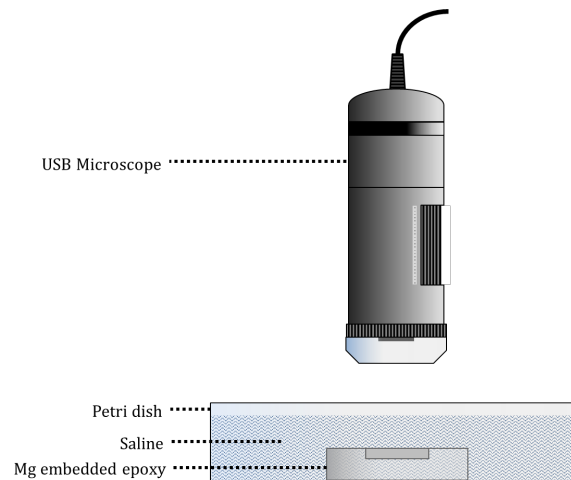
Figure 4.4 Setup used to image submersion experiments.

4.2.6 Electrochemical Corrosion Measurements

Following the submersion tests, the most promising texture types were identified for closer evaluation using electrochemical impedance spectroscopy (EIS). New samples were fabricated with electrical connections to allow electrochemical corrosion testing for monitoring over time. An insulated copper wire was attached on the back of the coupons

using adhesive copper tape that would allow conduction for EIS measurements. Then each sample was embedded in metallographic epoxy with only a 10 x 10 mm^2 area exposed. Each submersion test sample was polished and micro-patterned using the laser setup as described in Chapter 3.

The setup used to collect EIS data is illustrated below in Figure 4.5. Measurements were conducted in a 3-electrode cell composed of a titanium mesh counter electrode, a micro-patterned magnesium coupon with conductive copper wire embedded in epoxy as working electrode and a commercial silver-silver chloride electrode (CHI111, CH Instruments, Inc.) with 1 M KCl internal solution as reference electrode. Electrolyte was 0.9 w% aqueous NaCl (normal saline) solution. The distance between the working electrode (magnesium sample) and the reference electrode (silver-silver chloride) was kept at 10 mm for all measurements. All tests were conducted with Gamry Reference 600® potentiostat at room temperature (22° C). Potentiostatic EIS data was collected between 0.5 Hz and 100 kHz with 5 points/decade resolution.
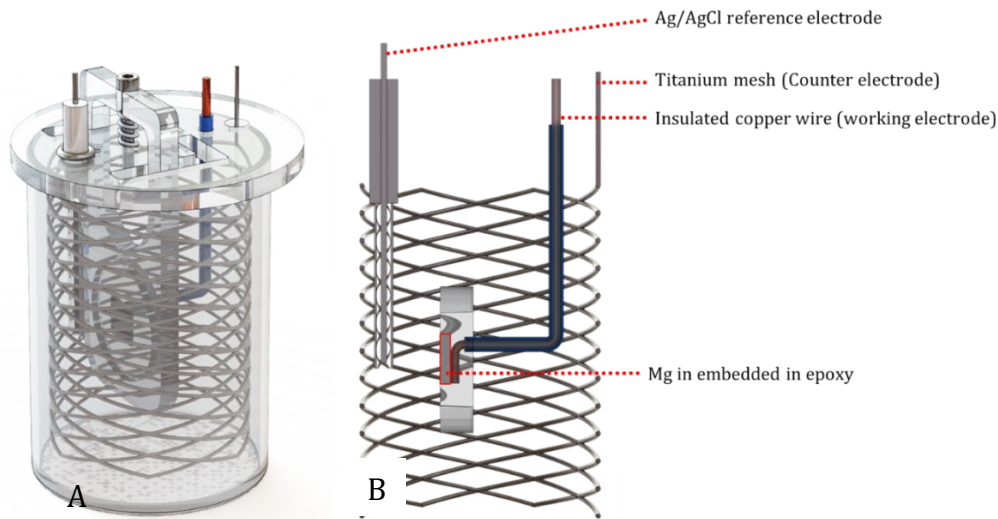
Figure 4.5 A) Rendered image of custom made EIS test cell used for electrochemical measurements. B) Cross sectioned side view of internal components only showing electrodes.

4.2.6.1 EIS Data Interpretation

Due to the dynamic nature of magnesium's volatile corrosion behavior, impedance spectra were collected every 10 minutes for one hour. The first data point was collected after five minutes following the submersion in electrolyte in order to allow stabilization of the open circuit potential between the reference electrode and the sample. Corrosion data for each time point was represented on a Nyquist plot (Figure 4.6).
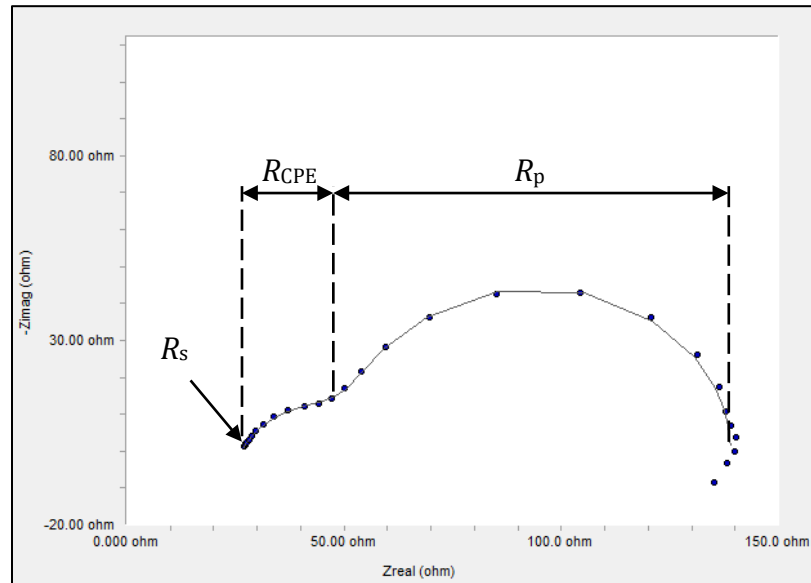
Figure 4.6 Nyquist plot for a polished magnesium surface. The line shows the fitted result via transmission line equivalent circuit with constant phase element.

The Nyquist curves were individually fitted using Gamry Echem Analyst software (Version 7.07, Gamry Instruments, Inc.). In order to fit a curve, Ishizaki et. al's [33] equivalent circuit (Figure 4.7-A) was used to determine corrosion resistances of textured samples. For smooth polished Mg surfaces, Curioni et. al's [18] equivalent circuit was used (Figure 4.7-B).
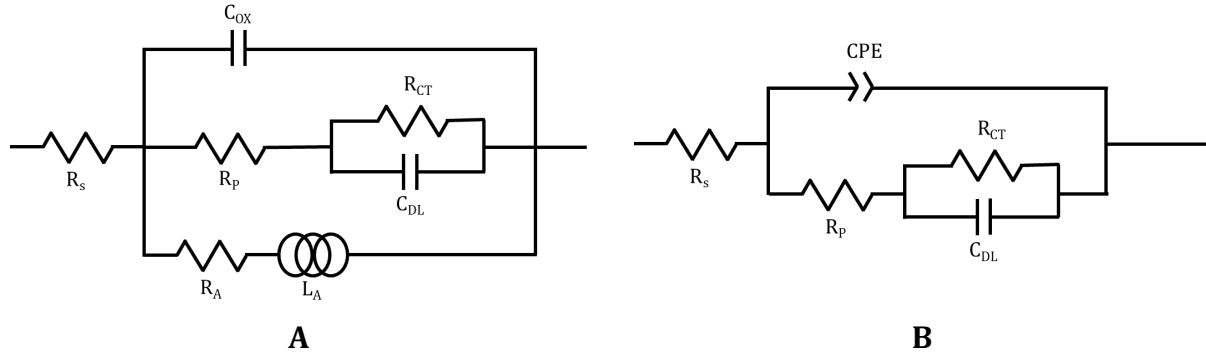
Figure 4.7 Ishizaki et. al's [33] equivalent circuit used to fit impedance spectra for untreated polished samples (A) and Curioni et. al's [18] equivalent circuit used to fit impedance spectra for micro patterned samples (B).

The corrosion current density (i_{corr}) was obtained from the polarization resistance (R_p) and Stern Geary constant (B) using equation (15 below.

$$i_{corr} = \frac{B}{R_p} \;, \qquad where \; B = \frac{\beta_a \, \beta_c}{2.3(\beta_a + \beta_c)} \qquad\qquad (15)$$

Anodic and cathodic Tafel slopes for Magnesium's corrosion reaction are represented by β_a and β_c respectively. The B value—also known as the Stern Geary constant—is approximately equal to 253 mV for Magnesium [18, 72]. The corrosion rate in terms of mm/year was estimated by faradaic conversion of the corrosion current density (i_{corr}). Considering uniform corrosion of Mg with the formation of Mg^{2+}, 1 mA/cm^2 of corrosion current density corresponds to a rate of corrosion of approximately 22.6 mm/year [32, 73]. Once the polarization resistances (R_p) were determined from corresponding Nyquist curves at each time point, corrosion rates were determined via this simple conversion.

In order to monitor medium conditions, pH of the electrolyte was measured before and after all tests for each individual sample. Electrolyte volume of 500 ml was used in order to minimize the effects of alkalization due to hydrogen evolution.

4.2.6.2 Accuracy of Electrochemical Methods

Degradation data gathered via electrochemical impedance testing is a fast and practical method to determine long term corrosion behavior of textured or polished magnesium surfaces. However, the accuracy of these measurements had to be quantified by comparing the converted EIS data (in terms of $mm.year^{-1}.cm^{-2}$) to a more direct measurement method such as gravimetric analysis (mass loss analysis).

In order to measure the corrosion rates using the gravimetric method, three pure magnesium coupons with $10 \times 10 \times 1.6$ mm^3 volume were prepared. The coupons were not embedded in metallographic epoxy for this test to have precise mass measurements. All faces of the coupons were polished in order to reveal substrate material with minimal oxidation using the same method explained in section 4.2.1. Mass of each coupon then was measured using a digital scale with a resolution of 0.001 g.

Three prepared magnesium coupons were each submerged in separate 50 ml beakers filled with 0.9 w% saline solution (same electrolyte used in EIS setup explained in section 4.2.6.1) at 22° C ambient temperature. Coupons were left in beakers for one hour (coupons were held from their corners using tweezers to ensure exposure of all faces to saline during immersion), then immediately dipped in boiling CrO_3/Ag_2CrO_4 solution for 60 seconds to remove corrosion byproducts (Method explained in detail in Section 4.2.2). Consecutively, each coupon was rinsed with de-ionized water, sonicated in 190 proof ethanol for five minutes and dried under pressurized air. Samples were then kept in a desiccator under vacuum for 30 minutes to ensure complete evaporation of ethanol residue on surfaces. Finally, each sample was re-weighed in order to determine their mass loss post-submersion.

In order to compare this gravimetric mass loss measurement to EIS corrosion rate data gathered under the same conditions, corrosion rate values of three additional freshly polished samples determined by EIS measurements in terms of mm/year were converted to g/hour by using the simple equation below.

$$Surface\ Area_{EIS}\ [cm^2] \times Corr.Rate_{EIS}\ \left[\frac{mm}{hour}\right] \times Density_{Mg}\ \left[\frac{g}{cm^3}\right] = Mass\ Loss_{EIS}\ \left[\frac{g}{hour}\right] \quad (16)$$

The averaged gravimetric corrosion rate then was compared to the average corrosion rate data gathered from EIS tests. Tabulated comparison can be seen in section 4.3.4.1.

4.3 Results and Discussion

4.3.1 Initial Submersion Test Results

Candidate microstructure pattern dimensions that would theoretically yield super-hydrophobic properties on the surface were determined using Cassie-Wenzel wetting formulations [16, 46, 47, 74]. Square pillar shaped micro-textures with 25, 30, 50 and 100 μm width were patterned by ablating (355 nm wavelength, 500 kHz pulse repetition rate, 1.5 W average power) equally spaced trenches orthogonally in vertical and horizontal directions. Each trench was created by ablating multiple adjacent lines side by side, resulting in wider trenches than the laser beam diameter [74]. Trenches that yielded micro pillars in between had width and depth of 30 μm and 40 μm, respectively. There was a deviation of approximately 5 μm on trench width and depth measurements due to the nature of the laser-based material removal. All samples tested in submersion experiments (without electrical connections) were processed with the oxide removal method since effects of the laser on oxidation's effects were not clear initially.

Several submersion tests were performed in saline and micro-patterns with slowest corrosion rates relative to polished samples were identified to narrow down the scope of the

66

experiments. Micro-patterns with 25, 30, 50 and 100 μm wide pillars were tested without stearic acid modification. As 100 μm wide pillars showed significantly improved corrosion resistance compared to narrower pillared textures (Figure 4.8), multiple variations of 100 μm pattern with varying trench width and depths were tested in order to see a possible trend.

As corrosion proceeded, dark colored corrosion byproducts ($Mg(OH)_2$ flakes) eventually blocked the view at the end of a 7-hour long imaging period. For samples with higher corrosion rates, this occurred during the test. However, the images captured before the view was blocked gave a good comparison of relative corrosion performance of the samples tested in a round of experiment. The corrosion progression of each sample is compiled on Figure 4.8 by putting together captured images from each time point. The definitive result at the end of a round of experiment was better understood by observing the remaining undissolved material in the epoxy pucks.

Each tested micro-patterned sample was also compared to a polished flat control sample to see the relative improvement or deterioration in corrosion resistance that comes with laser ablated micro-patterns. All polished samples—tested along with a micro-patterned sample—completely degraded in saline shortly after the one-hour mark. Since the performance of the polished control samples was comparable in all tests it is only documented once in Figure 4.8. An additional 100 μm wide pillared sample that is not shown on Figure 4.8 was created to image submerged in saline at high magnification.

All micro-patterned samples have shown improved corrosion resistance compared to polished ones. The benefit of stearic acid modification was tested only on 100 μm pillared pattern as it had the most improvement among all textures (Figure 4.8).
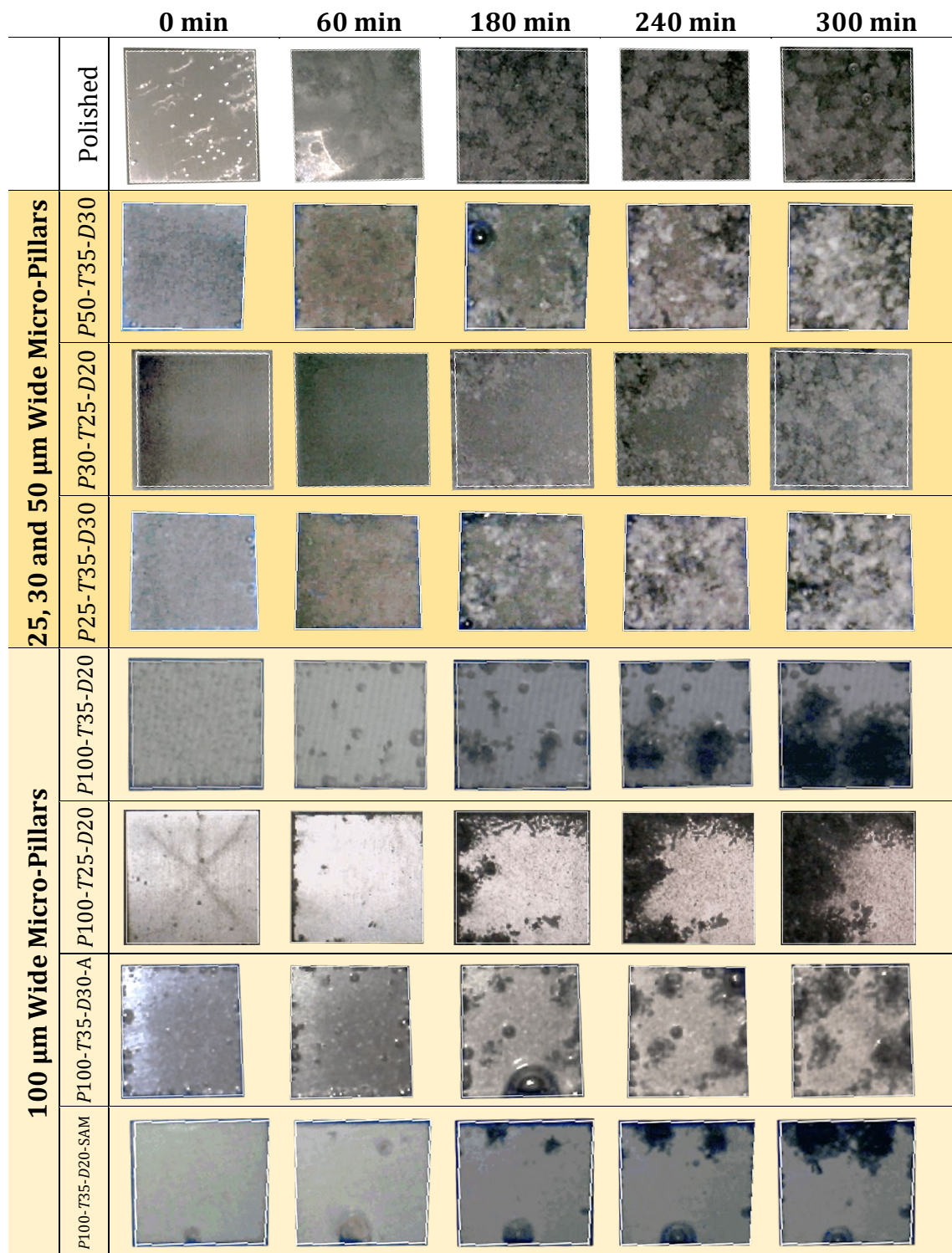
Figure 4.8 Micro-patterned samples immersed in saline over time. Each column of images shows the overhead view of samples in saline at the given time following submersion. Each row represents one sample with the stated name depicting its micro-pattern geometry (P: pillar width, T: trench width, D: trench depth in μm, SAM: stearic acid modification presence, A/B: indicators to distinguish samples with same micro-pattern dimensions).

4.3.1.1 Corrosion Performance of 25, 30 and 50 µm Wide Pillared Micro-Patterns

Sample with 30 µm pillar width stayed completely intact for more than 60 minutes. Around 180-minute mark, degradation initiated from top and bottom edges resulted in almost complete disintegration at the end of the experiment. By staying intact for more than 60 minutes, 30 µm wide pillars have shown improved corrosion resistance compared to the flat polished sample which dissolved completely in less time.

Submersion experiments were done with one 25 µm wide pillared sample and one 50 µm wide pillared sample in hopes of seeing a correlation between increasing/decreasing pillar widths and corrosion resistance after promising results of 30 µm wide pillars to some extent. As documented on Figure 4.8, decreased pillar thicknesses on 25 µm wide pillared sample did not improve the corrosion resistance but had quite the reverse effect. Sample with 50 µm wide pillared sample has shown similar corrosion performance to 30 µm with no significant improvement. The view of both 25 and 50 µm wide pillared sample was blocked by corrosion byproduct flakes after 1-hour mark (even though the micro-patterns were possibly still uncorroded under the flakes) and completely dissolved into saline at the end of 300-minute-long testing. Even though there was an improvement compared to untreated polished control samples, the corrosion rate of 25, 30 and 50 µm wide pillars were still too rapid.

4.3.1.2 Corrosion Performance of 100 µm Wide Pillared Micro-Pattern

A total of five 100 µm wide pillared samples were tested (*P*100-*T*35-*D*30-B is not documented on Figure 4.8 as it was imaged under high magnification as shown on Figure 4.9). There were minor dimensional deviations due to inaccuracies in laser machining that

only affected the trench widths and depths. All five samples had trench widths and depths of approximately 30 and 25 μm respectively.

All samples with 100 μm pillar width started to show signs of degradation around 180-minute mark at the magnesium/epoxy interface similar to 30 and 50 μm wide pillared samples (Figure 4.8). Around 300 minutes, the viewable area of all 100 μm wide pillared samples during the test was considerably undamaged by the saline which is a significant improvement compared to 30 μm wide pillars and the polished control sample. Samples have stayed mostly intact until 300-minute mark when approximately 50% of their surfaces were still visible without major disintegration. Similar behavior is observed on all four 100 μm wide pillared samples without stearic acid treatment, which supported the superiority of 100 μm wide pillars against corrosion compared to polished control sample and other tested micro-patterned samples with smaller pillar widths (25, 30 and 50 μm).

Stearic acid modified sample showed larger improvement in corrosion resistance by having 75% of its surface visible and uncorroded inside the saline after 300 minutes. Stearic acid modification—giving the micro-textured surfaces hydrophobicity—was expected to improve the corrosion resistance. Even though the corrosion resistance was improved with stearic acid modification, it did not cause a dramatic increase as anticipated.

One sample (not shown on Figure 4.8) that again had 100 μm wide pillars but was observed at high magnification to be able to reveal gas bubble activity happening inside its trenches. Proof of attachment and immobilization of gas bubbles in or around the trenches would explain the reduced corrosion behavior at this given micro-structure geometry dimensions. As expected, 100 μm wide pillared P100-T35-D30-B sample has shown similarly improved degradation performance similar to previous 100 μm wide pillared samples.

70

However, it was not possible to view gas bubble activity inside trenches past 120-minute mark due to micron sized small cluster of flakes blocking the high magnification view. During the visible 120-minute period, gas bubble generation coming off the surface was clearly visible however there was no signs of attachment or immobilization of a stable gas layer on the surface.

| 0 minutes | 60 minutes |
| 120 minutes | 160 minutes |
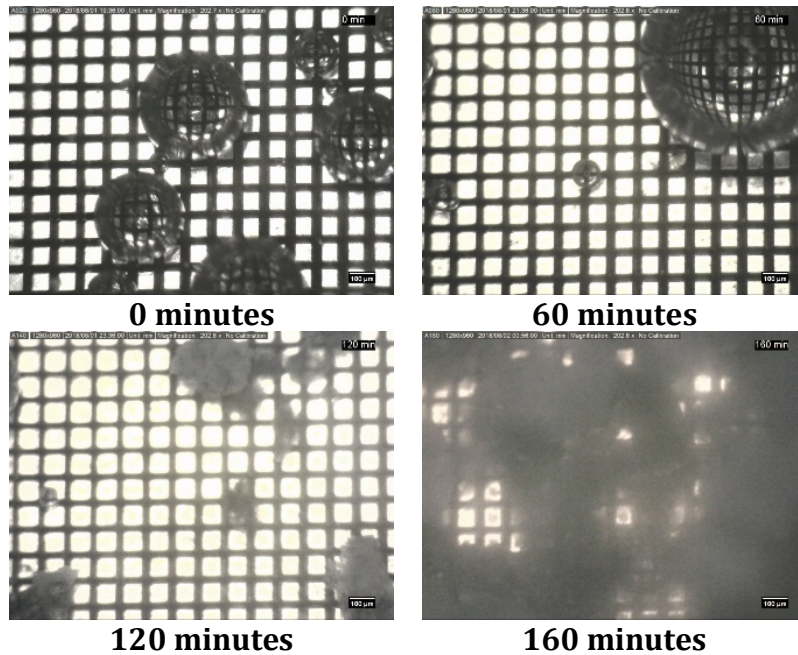
Figure 4.9 P100-T35-D30-B structure immersed in saline over time (200x magnification).

At the end of 8 hours of saline submersion, all samples with 100 μm wide pillars had a region of the sample with undegraded material embedded in their respective epoxy casings. SEM image of the uncorroded region of 100 μm wide pillared sample (P100-T35-D30-A) after 8 hours of saline exposure can be seen below in Figure 4.10.
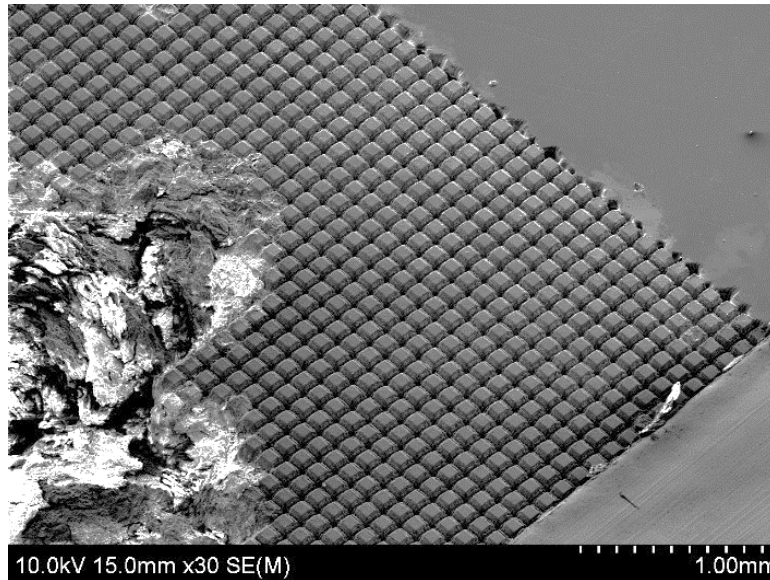
Figure 4.10 SEM image of an uncorroded region of P100-T35-D30-A after 8 hours of saline exposure.

4.3.1.3 Submersion Test Results Summary

Severe corrosion byproduct flake generation caused a blockage in the view after 300 minutes on all samples. However, samples were left in saline for 19 hours for one leg of the experiment. The remaining material after the submersion in saline for 19 hours can be seen below on Figure 4.11 showing the state of the surfaces post-submersion. Samples with100 μm wide pillared micro-pattern still had areas with completely intact pillars without a sign of degradation. This indicates significant corrosion resistance compared to polished control samples and patterns with narrower pillars.

As it can be seen on Figure 4.11, the polished sample was almost completely dissolved revealing the epoxy casing substrate that it was embedded in. Sample with 30 μm wide pillars was also highly deformed revealing its epoxy substrate partially.

One thing to draw out from Figure 4.11 is the fact that some regions did not visibly degrade such that the high amounts of degradations seem to initiate from a nucleation and

propagation phenomena. Where corrosion does not nucleate, there is no damage to the microstructures. This means there is a need to understand what drives nucleation of a failure point. Further imaging during similar samples' degradation behavior and surface characterization before and after submersion is done and discussed in Chapter 5.

| Polished control sample | P30-T25-D20 | P100-T25-D20 |
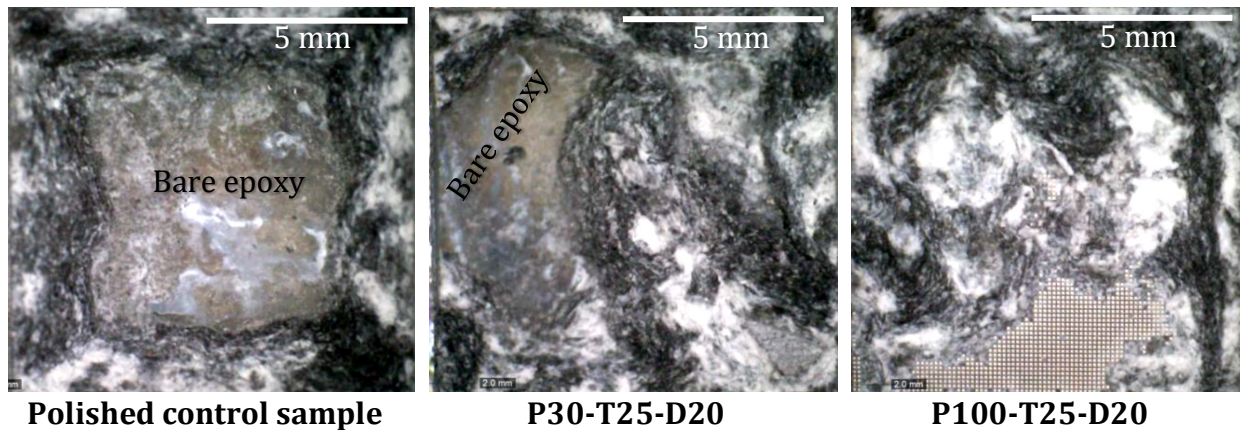
Figure 4.11 Aftermath of submersion for 19 hours in saline solution.

The resulting data gathered from submersion tests is mainly visual since it is based on captured images at certain time-points. In order to interpret any possible correlation between micro-pattern geometry and degradation behavior, a quantified metric was needed.

The ratio of the of corrosion affected area to the overall exposed area from the overhead view was chosen as a metric to compare corrosion resistances of each micro-patterned sample. Using Adobe Photoshop software, each captured image documented on Figure 4.8 was processed by highlighting both $Mg(OH)_2$ flakes and visibly corroded areas. Highlighted number of pixels were divided by the total number of pixels span the overall surface of the sample to get a corroded area fraction in terms of percentages. Corroded area fractions of each tested sample and version of Figure 4.8 with highlighted areas that were corroded or covered by $Mg(OH)_2$ flakes can be seen on Appendix C. Highlighted areas for a promising 100 µm sample can be seen below on Figure 4.12.
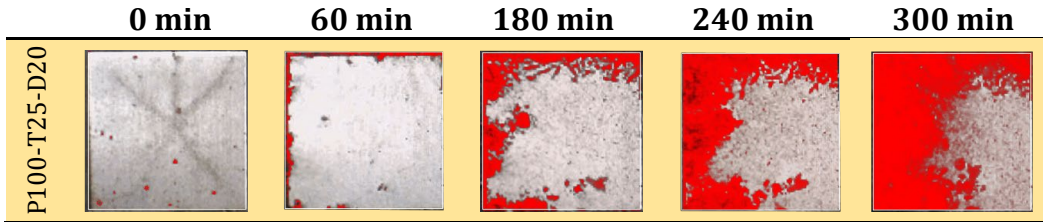
Figure 4.12 Highlighted Mg(OH)2 flakes and corroded areas visible on P100-T25-D20 sample during submersion at given timepoints.

An additional plot was made and documented on Figure 4.13 to see any possible correlation between laser ablated trench area fraction to corrosion performance at each time point. There is a possible correlation between increasing trench area fraction on the surface and the corrosion rates (with exception of 0% coverage, depicting the polished samples). Different behavior seen on 50% trench coverage is thought to be caused by under/over estimation of trench depths when total surface area was being calculated. An accurate depth measurement was not possible to achieve due to high roughness of the ablated trenches.
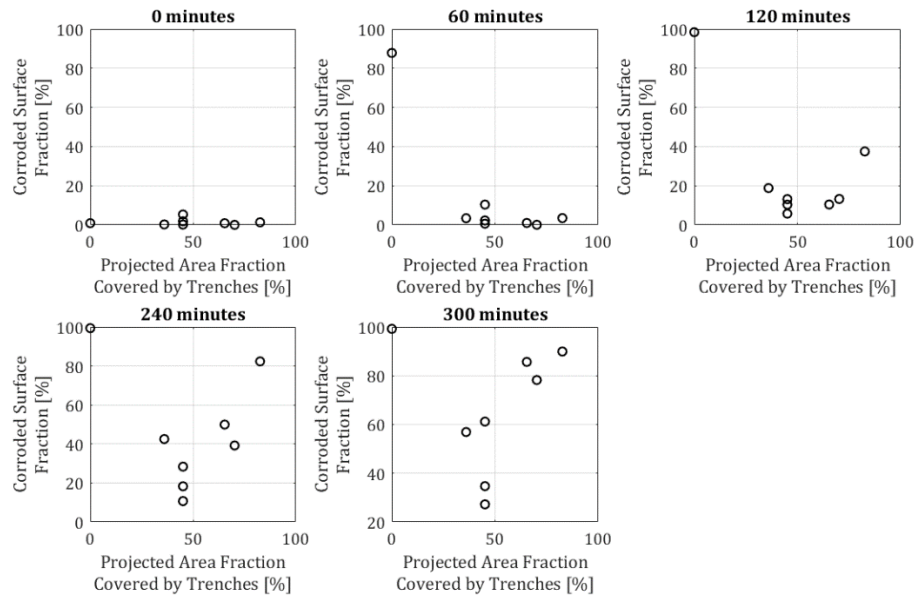
Figure 4.13 Effect of laser ablated trench area fraction to corroded area on given time-points. Trench coverage is based on the ratio of projected trench area to overall surface area.

In conclusion, increasing micro-pillar width and decreasing trench coverage have shown positive correlation to the corrosion resistance based on the visual assessment of submersion experiments. Stearic acid modification did not have any significant improvement in corrosion behavior which was not expected. The mechanics of corrosion protection and necessity of oxide removal process on 100 μm wide pillared is investigated further through electrochemical measurements.

4.3.2 Contact Angle Measurements

Micro-patterned samples with 100 μm wide pillars had contact angles of approximately 135 degrees after treating with stearic acid, whereas all unmodified micropatterned samples (including 100 μm wide pillared) had strong hydrophilic behavior with contact angles below the measurement threshold (Figure 4.9). Stearic acid modified hydrophobic samples have the abbreviation "SAM" in their names to distinct them from unmodified structures.

However, during contact angle measurements when stage was tilted the droplet did not roll off on any SAM hydrophobic samples even when the surface was vertical to ground. This is a sign of the wetting behavior bein in Wenzel state (Figure 2.10) where the droplets pin on the surface by infiltrating into the grooves. According to literature, this condition would yield gas blister formations (Figure 2.11) when in submerged conditions. Perfect Cassie state where the water droplets sitting on top of pillar is ideal for corrosion protection purposes since it yields gas plastron formation which the gas is completely contained within roughness grooves. However, this requires much higher precision manufacturing methods on magnesium that yield ideal smooth walled micro-pillars similar to illustration shown on Figure 2.9. Currently employed laser ablation method to generate surface micro-patterns

75

when combined with stearic acid modification is only able to promote gas blister formation in submerged conditions which is expected to show corrosion inhibiting effects.

<div align="center">A   B</div>
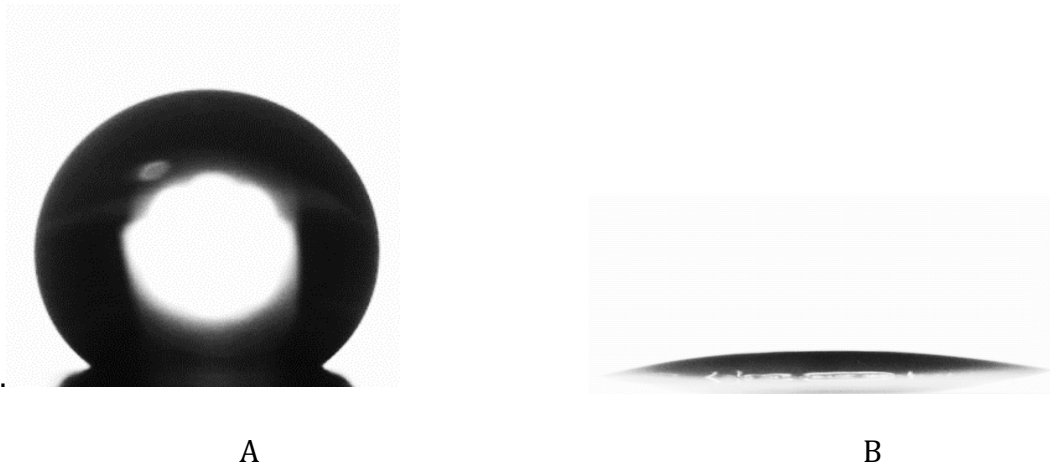
Figure 4.14 Static contact angles on micro-pillar structures with (A) and without (B) stearic acid modification.

4.3.3 Effect of Laser Generated Oxide Layer

All samples tested in submersion experiments were cleaned using the oxide removal process introduced in section 4.2.3 since the effect of laser ablation influenced oxidation was not clear. There is a possibility of a buffering effect against corrosion when a thick oxide layer is deposited. However having an extra step of oxide removal process in sample preparation is not desirable due to its impracticality and the introduction of chromium based contamination on surfaces as documented on section 4.2.3.1. In order to determine necessity of oxide removal process in further experimentation, EIS measurements were utilized.

One of the micro-pillared samples was cross sectioned and oxidation amounts on trench surfaces were determined with EDS. Cross sectioning was done with a diamond saw after the sample was embedded in metallographic epoxy then polished with the procedure explained on section 4.2.1. As expected, EDS measurements (Figure 4.12) have shown oxidation was more prominent on trench bottoms and walls where the laser beam directly

hit the substrate during laser machining. Areas unaffected by the laser had similarly low oxygen content. The 6-7% oxygen content away from the laser machined regions is likely surface oxidation of the polished cross section from ambient atmosphere and de-ionized water exposure during polishing.
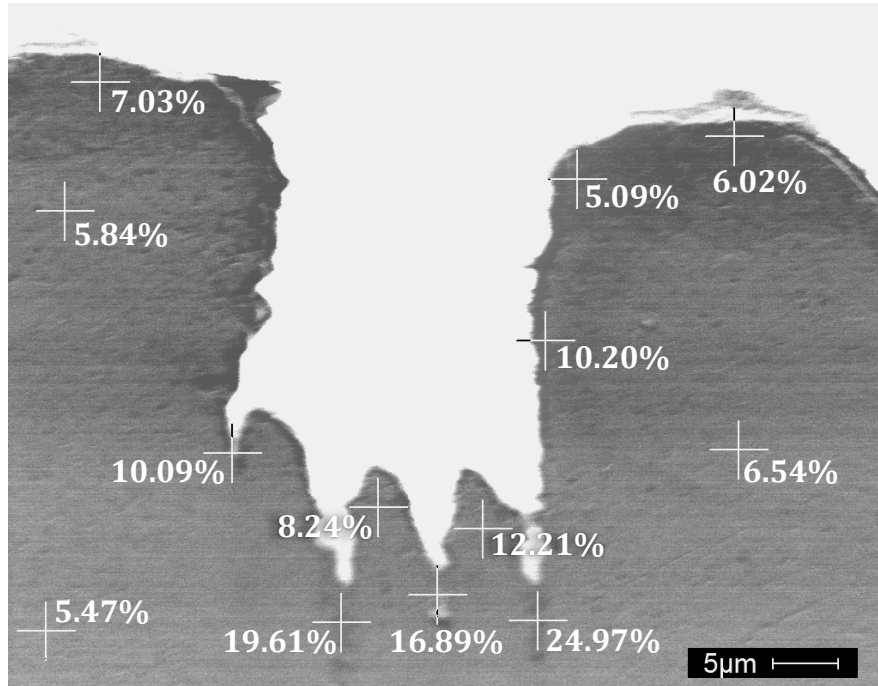
Figure 4.15 Localized oxygen content (in terms of atomic oxygen percentage) on cross section of a laser ablated micro-trench. Measurements were taken following the laser ablation without oxide removal procedure.

In order to assess the possible corrosion hindering effect of the oxide layer deposited in the trenches, the oxide layer was removed by selective etching following ASTM standard G1 (Section 4.2.3) and compared to unetched samples. The amount of oxidation before and after etching was quantified via EDS on both pillar surfaces (plateaus) and trenches. The etchant smoothed the micro-texture morphology and significantly reduced oxygen on the surface. As documented on Figure 4.16, average atomic composition of oxygen on top of the pillars (not directly ablated by laser) reduced from 5.02% to approximately 2.34% after

oxide cleaning process. Oxide removal reduced the laser ablated trench regions from 29.92% to 13.60% post-cleaning. However, there was also minor amounts (around 6.80%) of chromium (Cr) deposition on trench surfaces originating from the chemical solution used to remove the oxide.
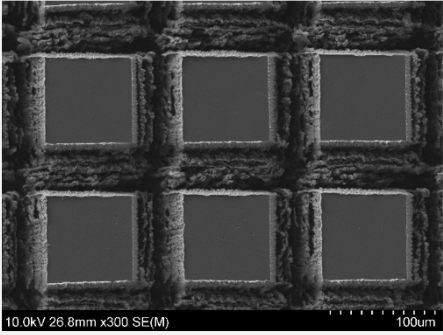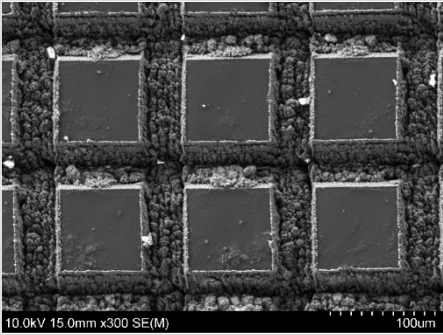
After Removal		Mg [A%]	O [A%]	Cr [A%]
	Plateaus	97.66±0.13	2.34±0.13	0
	Trenches	79.59±1.56	13.60±1.90	6.80±0.47
Before Removal		Mg [A%]	O [A%]	Cr [A%]
	Plateaus	94.98±2.10	5.02±2.10	0
	Trenches	70.08±1.98	29.92±1.98	0

Figure 4.16 Elemental compositions on plateau and trench surfaces of pillared micro-textures before and after oxide removal process.

Minor amounts of oxidation on unablated polished portions is caused by ambient air exposure during the transfer of the samples between processes. A relatively higher amount of oxidation on the trenches is expected due to the thermal nature of the laser ablation process which promotes oxidation. Increasing the submersion duration inside CrO_3/Ag_2CrO_4 solution during the oxide removal process explained above could help further reduce the oxygen composition. However, it may not be beneficial since there is a potential risk of etching away substrate material when samples are overexposed to CrO_3/Ag_2CrO_4 solution [29]. Relatively higher oxidation and minor amounts of chromium deposition were only

observed on trenches and it is attributed to the higher roughness values of the trench surfaces making it harder for the boiling CrO_3/Ag_2CrO_4 solution to infiltrate in while also promoting entrapment of Cr molecules present in the solution.

The potential buffering effect of the high oxygen region from laser ablation on corrosion resistance is investigated through EIS measurements on both polished (smooth) and patterned surfaces. Oxidized polished samples were included in tests in order to assess the effect of oxidation itself as a corrosion inhibitor without the effects of patterning. Patterned "oxidized" samples were tested as ablated following the laser ablation procedure with the oxide layer intact on surface. Patterned "low oxide" samples prepared similarly were post processed with the oxide removal procedure before EIS measurements. The polished "oxidized" sample group with elevated oxidation levels was prepared by leaving them in room environment for four days allowing them to oxidize naturally, while the "low oxide" polished sample group was stored in a desiccator immediately after they were polished. The average surface compositions of patterned and polished samples determined by EDS can be seen on Figure 4.16 and Table 4.1 respectively. Sample size for each group was three.

Table 4.1 Elemental compositions on polished surfaces before and after oxide removal process.

	Mg [A%]	O [A%]	Cr [A%]
Low Oxide	99.55 ± 0.26	0.45 ± 0.26	0.00
Oxidized	97.76 ± 0.22	2.24 ± 0.22	0.00

Corrosion rates of each sample group of three is plotted over a 60-minute time period (Figure 4.17). Impedance data gathered from EIS measurements were converted to corrosion rates in terms of mm/year with the method explained earlier (Section 4.2.6.1). Due

to the untreated/untextured state of the polished bare magnesium substrate, corrosion rates were relatively high for both sample types. The slightly increased amounts of oxidation on the polished sample group left in ambient room environment did not cause a notable inhibiting effect on the degradation behavior compared to the freshly polished (low oxide) sample group.

Patterned samples had significantly decreased corrosion rates compared to polished samples regardless of the presence of increased oxidation from laser ablation. The oxide removal process had a minimal impact on the corrosion resistance of both patterned and polished surfaces Since the oxide/hydroxide layer is inevitable as soon as the samples are submerged in the electrolyte (due to hydrophilic properties), it is desirable to leave the oxide/hydroxide layer intact on surfaces.

Oxide layer cleaning process itself introduces biochemically undesirable components on the surfaces such as chromium deposited by CrO_3/Ag_2CrO_4 solution. Since laser ablated trenches make approximately a third of the overall projected area of all EIS tested samples, the possibility of a buffering effect due to chromium presence on trenches against corrosion arises. However, the results from submersion tests performed with narrow pillared micro-patterns (hence larger trench coverage) shown significantly poor corrosion resistance (Section 4.3.1.3) which contradicts this possibility. Additionally, Figure 4.13 showing the relation between the trench area coverage and corrosion resistance of all submersion test samples has shown negative correlation to a limited extent.

No significant evidence was found for corrosion inhibiting behavior of the laser-induced oxide layer since oxide free micro-patterns have shown similar corrosion resistance compared to as-etched "oxidized" patterns. With the information gained from this corrosion

assessment, the following corrosion studies were completed to understand increased corrosion resistance on patterned hydrophilic and hydrophobic samples without the oxide removal procedure.
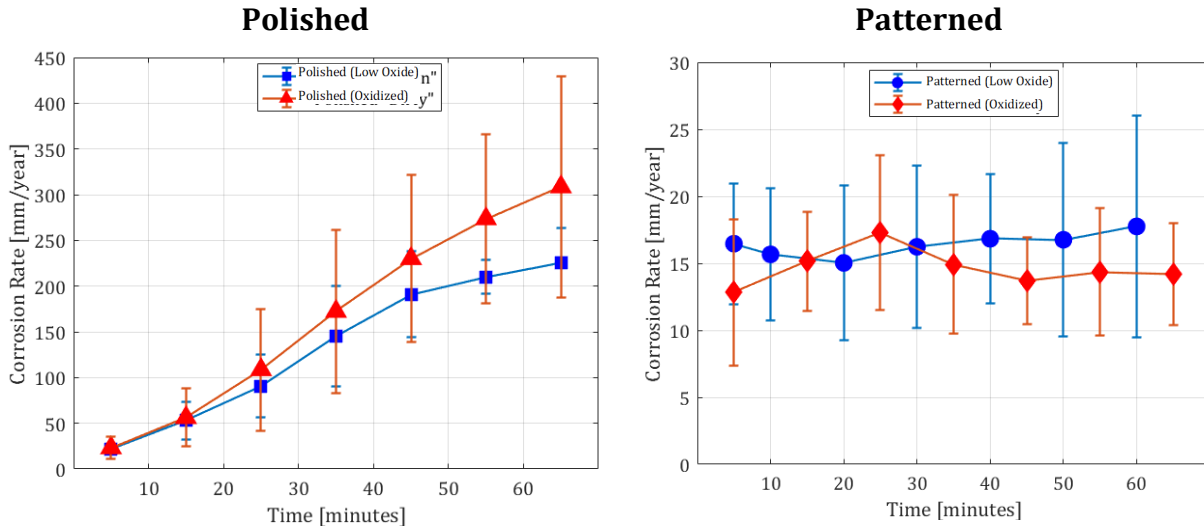
Figure 4.17 Corrosion rates of sample groups with and without oxide removal process.

4.3.4 EIS Results

4.3.4.1 Comparison of Electrochemical and Gravimetric Corrosion Analysis Methods

Correlation between EIS measurements and gravimetric analyses had to be quantified in order to use EIS method as the sole deterministic tool for corrosion behavior of surfaces used in a portion of this study. Detailed mass loss measurements for each polished Mg coupon can be seen on Appendix D. Average gravimetric corrosion rates are compared to the EIS data (units converted to g/hour using equation derived in section 4.2.6.2) on Table 4.2.

Table 4.2 Corrosion rate comparison of data derived from mass loss and EIS measurements.

Gravimetric Corrosion Rate [g/hour]	Electrochemical Corrosion Rate [g/hour]
36 ±3	45 ±8

Relatively close corrosion rate values between EIS and gravimetric methods were observed and based on this conclusion EIS was used for the remainder of the experiments in confidence in order to assess corrosion behavior of magnesium surfaces.

4.3.4.2 Effect of Hydrophobicity (Stearic Acid Treatment)

The same 100 μm wide pillared patterned surfaces that have shown the most corrosion resistance in submersion tests (Section 4.3.1) were replicated with and without stearic acid modification (SAM) for EIS testing to assess the effects of hydrophobicity on corrosion resistance. SEM images of tested samples can be seen in Appendix E. Patterned hydrophobic samples were prepared by submerging them in ethanolic stearic acid solution post laser ablation as explained in detail on section 4.2.4. Hydrophilic patterned samples were prepared by leaving them untreated (without stearic acid modification) following the laser ablation. Sample size for each patterned surface group (hydrophilic and hydrophobic) was three. Oxide layer removal procedure was not applied on any of the samples as its effect on corrosion behavior was shown above as negligible. Contact angle measurements were taken on a representative sample from each hydrophilic and hydrophobic group. Micro-patterned samples had contact angles of approximately 135 degrees after treating with stearic acid, whereas all unmodified micropatterned samples had strong hydrophilic behavior with contact angles below the measurement threshold.

EIS data was collected for one hour at 10-minute intervals in saline solution. The resultant polarization resistance (R_p) was calculated from a fitted Nyquist curve using Gamry Echem Analyst software. Polarization resistance value for each data point was converted to corrosion rate in terms of mm/year using the formulation shown on section 4.2.6.1. Plotted

EIS results of patterned surfaces with and without stearic acid modification (SAM) is shown on Figure 4.18.
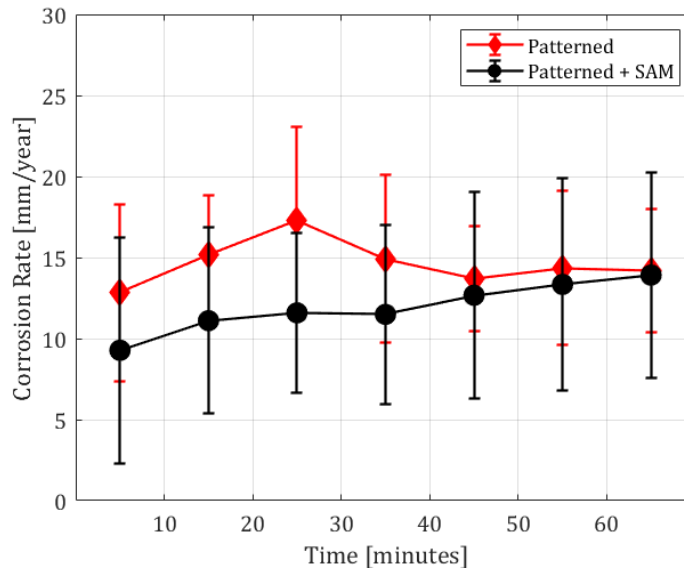
Figure 4.18 Corrosion rates over time estimated with EIS. Each data point and error bar represent mean and standard deviation of the corrosion rate of three separate samples with same micro-texture geometry.

Both patterned sample groups have shown significantly improved corrosion resistance compared to polished samples. However, stearic acid modification that yielded hydrophobic behavior on patterned surfaces (Section 4.2.4) did not cause a significant decrease in corrosion rates compared to hydrophilic patterned samples which is unexpected in theory. First 40 minutes following the submersion in medium has shown marginally improved corrosion resistance on hydrophobic samples relative to hydrophilic samples. However, the average corrosion rate values on both hydrophilic and hydrophobic groups have converged after 40 minutes of measurements in saline. Similar to submersion tests (Section 4.3.1), the effect of SAM on corrosion rates was not significant as hydrophilic textured P100 samples still had significant corrosion resistance without any further treatment. The increased corrosion resistive behavior of textured samples is quite stable

83

over the course of 1 hour. Figure 4.19 captured during EIS measurements of one of the patterned samples show gas evolution and macro bubble attachment on the surface which is expected to have large influence on corrosion protection. The micro-activities of gas bubbles inside the trenches needs to be further analyzed by microscopy in submerged condition during EIS measurements.

The minor increase in corrosion resistance during the first 40 minutes on hydrophobic samples is thought to be caused by the slight protective effect of hydrocarbon layer developed on the surface due to stearic acid modification. As the testing continued past the 40-minute mark, the difference between treated and untreated samples disappears. It is possible that the thin stearic acid monolayer has dissolved or been removed with surface corrosion and yielded similar corrosion rates on both hydrophilic and hydrophobic samples. However, the fact that the corrosion rate remains low, indicates the action of a second protective mechanism that does not depend on the surface coating or wetting characteristics.
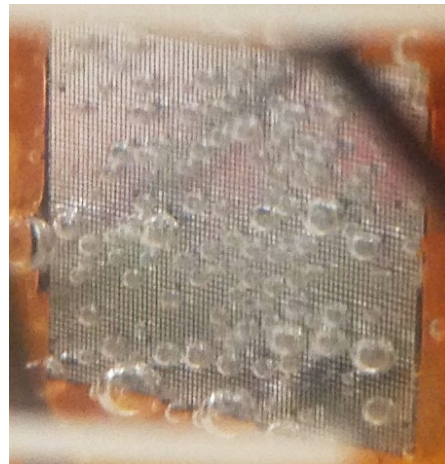
Figure 4.19 P100-T30-D40-CRO3-A Sample during EIS testing. Gas evolution and bubble attachment over micro-patterns can be observed.

4.4 Conclusion

Effects of micropatterning and hydrophobicity that comes with on corrosion resistance of pure magnesium were observed through submersion experiments and EIS experiments in saline solution. In order to narrow down the scope of experiments, initial submersion tests in saline were performed on square micro-pillared samples with square pillar edge dimensions varying between 25 and 100 μm. Samples with 100 μm square pillars have shown significant corrosion resistance as they partially stayed intact in corrosive saline environment for more than 19 hours. Hence the successive experimental efforts were focused on samples with 100 μm square pillars as they have shown the most promising corrosion resistance. Unexpectedly, hydrophilic samples without the stearic acid modification with identical micro-pattern geometries to hydrophobic ones have also shown comparable corrosion resistance.

While investigating underlying reasons for the corrosion protection of patterning, significant pre-submersion oxidation was detected on patterned surfaces caused by laser ablation micropatterning method. The effect of surface oxide layer from atmosphere exposure and laser etching on corrosion protection was investigated through controlled experiments. There was no significant difference between corrosion behaviors of as patterned and patterned samples without oxide layer. Due to undesirable chemical deposition on surfaces that came with oxide removal process and its insignificant influence on corrosion response, it was concluded that having an additional oxide removal procedure in surface preparation was not beneficial for biomedical application purposes.

In order to show repeatability and to further investigate corrosion behavior of micropatterned hydrophobic and hydrophilic surfaces that have shown good corrosion

85

resistance in submersion tests, controlled EIS experiments were conducted. Spacing between trenches was again 100 µm. Since oxide layer removal was rendered uninfluential on corrosion response earlier all patterned samples had visible oxidation after fabrication of the micropatterns (Figure 4.20). Same as submersion experiments patterned samples with hydrophilic (without stearic acid treatment) and hydrophobic (with stearic acid treatment) were compared via EIS measurements. According to EIS measurements, all patterned samples had similar significant corrosion resistance compared to untreated polished surfaces. These results were in agreement with the preliminary submersion tests. However, the similarity between identically patterned hydrophilic and hydrophilic samples' corrosion behavior raised questions about the hypothesized corrosion protective mechanism utilizing the hydrophobicity. The possible effect of laser induced oxide layer has been shown ineffective on corrosion protection, hence the hypothesized effects of gas adhesion within micro-trenches and additional mechanisms that might play a role are further investigated in Chapter 5.
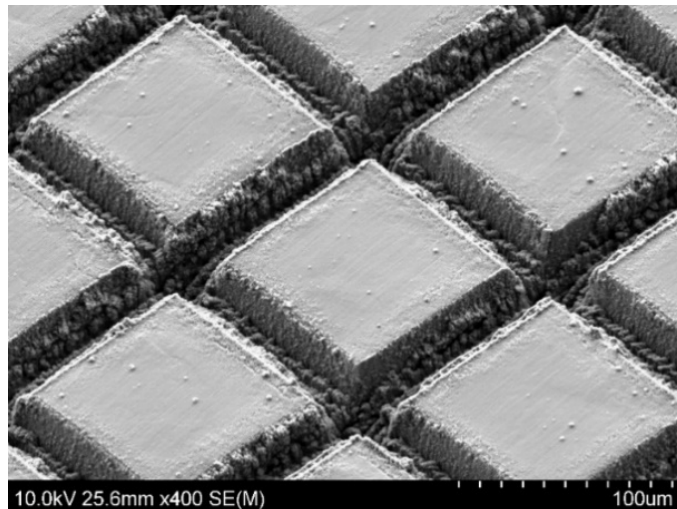
Figure 4.20 Laser ablated micro-pillars and visible oxidation on trenches caused by ablation.

Chapter 5: Unexpected Increased Corrosion Resistance on Hydrophilic Surfaces

In the previous chapter, 100 μm wide micro-pillared patterns were demonstrated to have significantly improved corrosion resistance compared to smooth surfaces. However, laser ablating super-hydrophobic surfaces with contact angles higher than 150 and low contact angle hysteresis (yielding Cassie-Baxter type wetting properties) was not possible due to irregularities in ablated trench geometries and inaccuracies in laser machining setup. Unexpectedly the hydrophilic textures have shown high corrosion resistances compared to smooth surfaces up to approximately a factor of 45. Possible explanations for this behavior are studied and discussed in this chapter.

5.1 Introduction

The purpose of this dissertation was to investigate a possibility of entrapping generated hydrogen gas within Cassie-Baxter type surface profiles. In theory, entrapment of gas bubbles on hydrophilic or Wenzel type roughness profiles have no examples in literature. However, there are several methods to test bubble adhesion inside micro-grooves.

First qualitative method to observe gas adhesion within grooves is optical imaging of the samples in a submerged condition. Several studies have adopted a camera setup placed at a certain angle relative to the sample surface rendering gas bubble distinctive with reflecting light [16, 73, 75].

Another theory that might explain increased corrosion resistances on micro-pillared surfaces is the possible local increase in alkalinity caused by micro-pillars. It is well documented that increased alkaline environment promotes stability of corrosion byproduct protective layers created on magnesium surfaces [18]. Once the oxide layer is rendered insoluble in the medium, combined with increased surface area of a patterned surface might cause superior corrosion protection. Additional tests were performed to investigate these theories.

5.2 Experimental Setup

The same 100 µm wide pillared micro-patterns were created with the methods explained in previous chapters. The oxidation removal step was skipped for this setup as it has been documented in section 4.3.3 that oxide removal has no significant effect on corrosion behavior. Furthermore, introducing chromium on the surfaces due to oxide removal is undesirable for biocompatibility.

One patterned sample group was treated with stearic acid modification yielding hydrophobic properties. Apparent contact angle on the surface was 135 degrees as expected (Section 4.3.2). However, the droplet used to determine the contact angle was in Wenzel state (pinned into the trenches) as it was not possible to roll it off the patterned surface at any tilt angle.

In order to see bubble attachment on the surface, a digital microscope (at low magnification) and a light source were placed facing the patterned EIS sample at a 45 degree angle on opposite sides (Figure 5.1). A second digital camera was also placed directly facing the sample to get a natural colored view of the corrosion process. The EIS cell containing the sample and electrodes (shown in detail on Figure 4.5) was placed in a sonicator bath in order

to remove attached bubbles when sonication was activated. The detachment of gas bubbles would allow the observation of corrosion buffering effects of a possible gas layer caused by hydrophobicity as hypothesized. Impedance spectra were collected from prepared samples with 10-minute intervals for an hour. Following the 70 minutes of undisrupted measurements, the sonicator was turned on for 10 seconds and additional impedance spectrum data was collected to see the effects of bubble detachment from the surfaces.

In order to monitor medium conditions, pH of the electrolyte was measured before and after all tests for each individual sample. Electrolyte volume of 500 ml was used for these experiments which is larger than previous experimentation volumes (250 ml) in order to minimize the effects of alkalization due to hydrogen evolution.
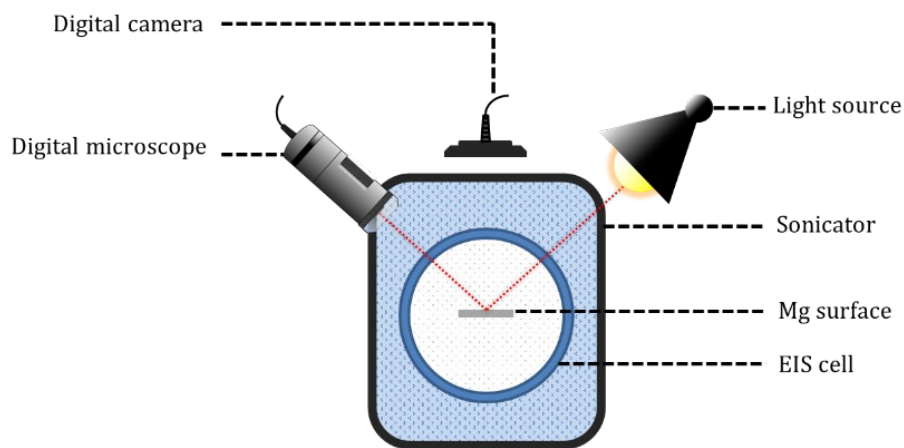
Figure 5.1 Top view of the EIS and imaging setup used for corrosion monitoring.

5.3 Correlation Between CPE and Hydrogen Layer

The equivalent circuit used to fit the impedance spectra of the patterned samples (Figure 4.7-B) contains a constant phase element (CPE) that is useful for understanding the properties of a possible gas interference on rough surfaces.

Constant phase angle element (CPE) is used in equivalent circuits when a non-ideal charge storing double layer behavior is present on surfaces. This charge storing behavior is

89

caused by either defective protective films or a dynamic air-metal composite surface generated by partial aerophilic behavior of a rough surface. Impedance of this non-ideal CPE capacitance as a function of applied EIS voltage frequency is defined as:

$$Z_{CPE}(\omega) = 1/y_0(j\omega)^n \qquad (17)$$

Where y_0 is a constant and n is a real number between 1 and 0. It should be noted that when n is equal to 1, impedance of CPE simply reduces to impedance of a simple capacitor (where $y_0 = C$).

The contact area between the electrolyte and the sample substrate can be qualitatively determined by comparison of y_0 coefficients of a sample's EIS spectra fits at different time points. Any interference between the electrolyte and the metal substrate by adhered gas bubbles would cause a momentary reduction in detected surface area. Hence, an increase in y_0 values would point to an increase in electrolyte contact area on substrate. The y_0 parameter is used to assess the influence of gas layer adherence on the corrosion rates.

5.4 Results and Discussion

5.4.1 Effect of Gas Layer Adhesion

Six identically patterned samples (SEM images shown on Appendix F) were tested through EIS experiments while capturing the surface conditions with a camera. Three of the six samples were hydrophobic due to the applied stearic acid treatment whereas the remaining samples were hydrophilic. Due to the angled camera and light placement, generated gas bubbles had a silvery color distinct from the substrate material allowing a qualitative assessment of gas adhesion. During EIS experiments, a sonicator containing the EIS cell was turned on at the 69-minute mark for 30 seconds then EIS data was continued to

90

be collected starting at 70-minute mark. Sonication was expected to detach possible gas layer present over the hydrophobic samples hence increase the corrosion rates.

Corrosion rates of all six tested samples are shown on Figure 5.2. As demonstrated in previous chapter, all hydrophilic and hydrophilic patterned samples have shown similar corrosion rates inside normal saline. However, once the sonicator was activated which agitates the electrolyte inside the EIS cell, all samples have experienced rapid increase in corrosion rates which was not expected on hydrophilic samples. After the sonicator was deactivated there was a slight regeneration of corrosion resistance on all samples.
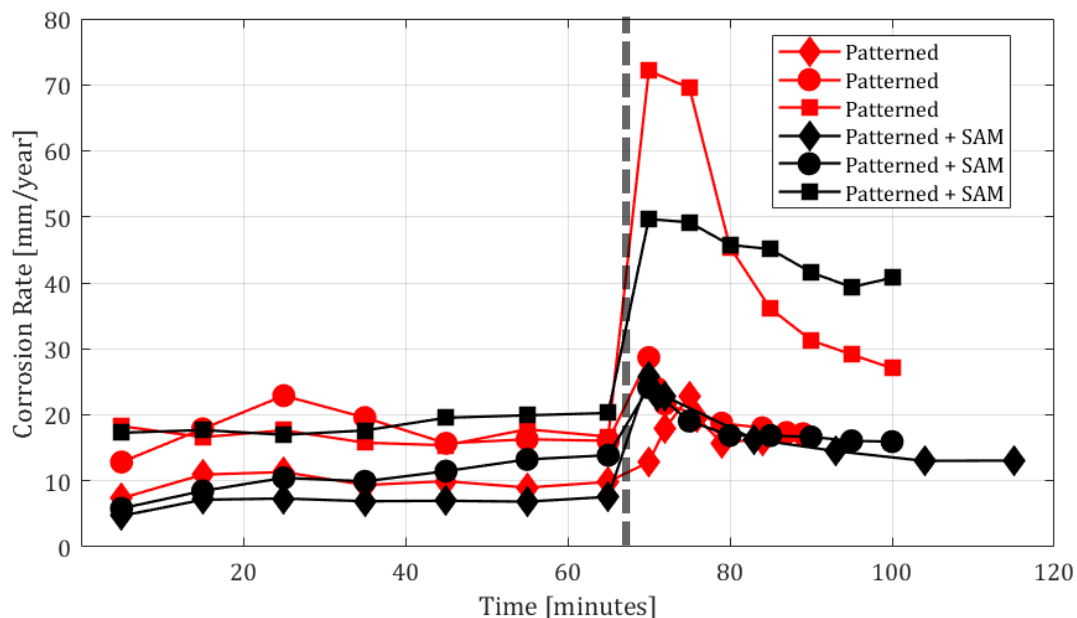
Figure 5.2 Corrosion rates of individual hydrophilic and hydrophobic patterned samples over time. Vertical dashed line indicates the instance the sonicator was turned on for a duration of 30 seconds.

Surface conditions of one hydrophilic and one hydrophobic sample captured during the EIS measurements is shown on Figure 5.3. On sample with no stearic acid modification (hydrophilic), there was no significant bubble attachment where bubbles were generated and detached from the surface continuously. Furthermore, hydrophobic SAM sample's bubble formation was also very uniform across the surface and individual bubble sizes were

small showing signs of containment within trenches (grey color of the samples is caused by the bubbles. Contrast can be seen at the instant the sample is sonicated. The surface achieves a darker grey color for a very short period before rapid bubble regeneration.). All samples had corrosion rate regeneration after sonication due to regeneration of bubbles. The unexpected similar corrosion rate increase that came with sonication on all samples was investigated by analyzing much useful EIS data.
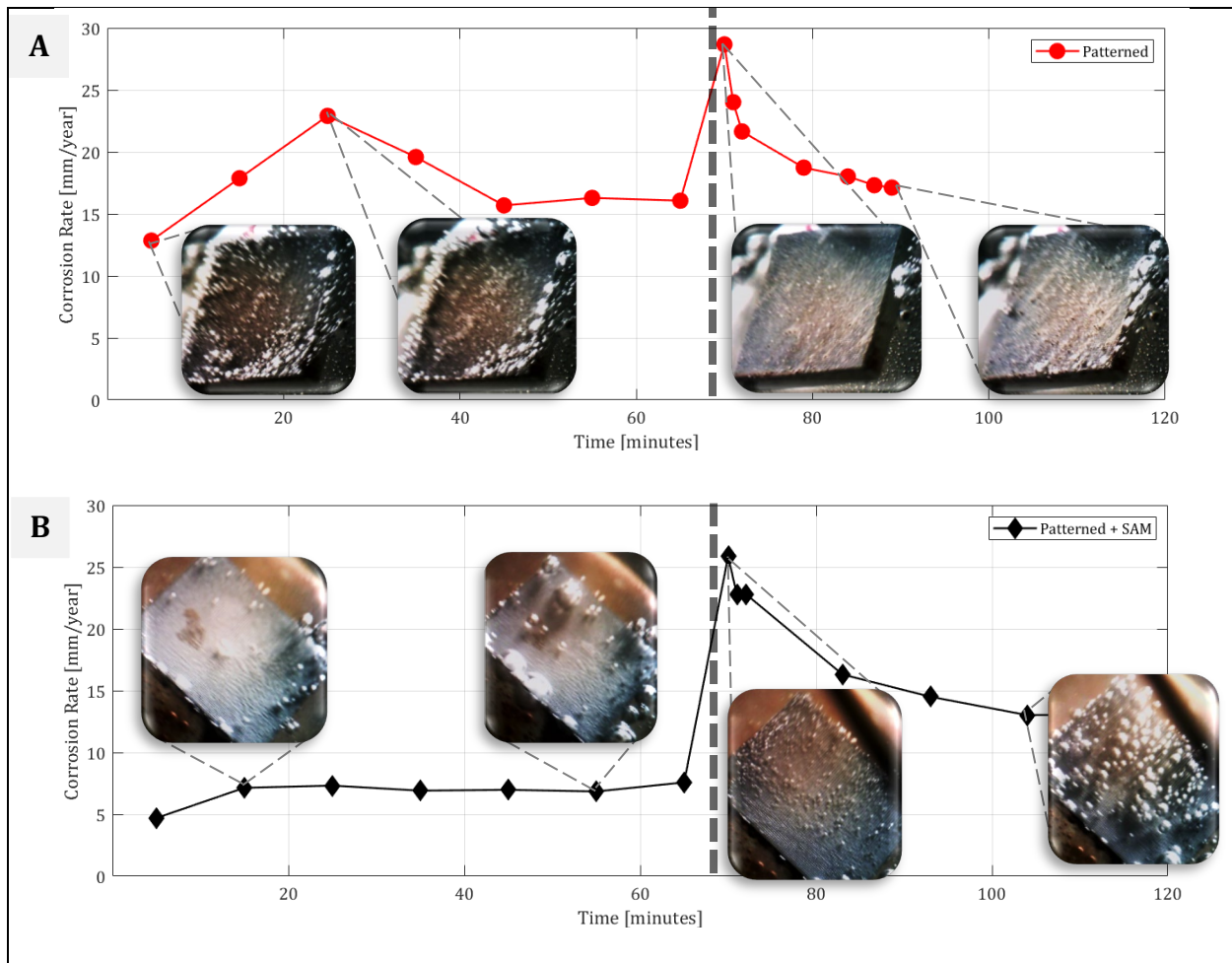
Figure 5.3 Visual gas bubbles and corrosion rate comparison of (A) hydrophilic (patterned) and (B) hydrophobic (patterned + SAM) samples. Corrosion rates on y-axis are determined via EIS. Vertical dashed lines on both graphs indicate the time-point when sonicator was turned on.

On the sample with no SAM (Figure 5.3-A), there is a direct correlation with visible bubbles and corrosion rate. Second sample had higher and irregular corrosion behavior due

to irregularities in laser machining. Central zones are not inhabited by corrosion. All samples had corrosion rate regeneration after sonication due to regeneration of bubbles. Stearic acid modified sample (Figure 5.3-B) had similar corrosion rate to the untreated patterned sample as expected through experimental results documented in Chapter 4. However, SAM sample's bubble formation was also very uniform across the surface and individual bubble sizes were small showing signs of containment within trenches (grey color of the samples is caused by the bubbles. Contrast can be seen at the instance sample is sonicated. Surface achieves a darker grey color for a very short period before rapid bubble regeneration.). This is possibly a sign of gas layer adhesion playing a role in corrosion inhibition on stearic acid modified hydrophobic samples. Even though the untreated hydrophilic patterned samples had similar corrosion rates to SAM samples, the lack of observed gas adhesion (as expected) points to the possibility of more than one mechanism playing a role in corrosion inhibition on both sample groups.

5.4.1.1 Correlation Between CPE and Hydrogen Layer

Collected EIS spectra from all six patterned samples (Figure 5.2) were fitted using Ishizaki et. al's [33] proposed equivalent circuit (Figure 4.7-B) for rough textures. The equivalent circuit contains a constant phase element (CPE) that is useful for understanding the properties of a possible gas interference on rough surfaces. Constant phase angle element (CPE) is used in equivalent circuits when a non-ideal charge storing double layer behavior is present on surfaces. This charge storing behavior is caused by either defective protective films or a dynamic air-metal composite surface generated by partial aerophilic behavior of a rough surface. Impedance of this non-ideal CPE capacitance as a function of applied EIS voltage frequency is defined as:

93

$$Z_{CPE}(\omega) = 1/y_0(j\omega)^n \tag{18}$$

Where y_0 is a constant and n is a real number between 1 and 0. It should be noted that when n is equal to 1, impedance of CPE simply reduces to impedance of a simple capacitor (where $y_0 = C$).

The contact area between the electrolyte and the sample substrate can be qualitatively determined by comparison of y_0 coefficients of a samples EIS spectra fits at different time points. Any interference between the electrolyte and the metal substrate by adhered gas bubbles would cause a reduction in detected surface area. Hence, an increase in y_0 values would point to an increase in electrolyte contact area on substrate.

With the experiment setup explained above, when the sonicator is activated it causes detachment of the gas bubbles as seen on Figure 5.3. However, with the camera setup used, it was not possible to see microscopic trenches and possible micro bubble generation/adherence within. There were signs of possible uniform gas adhesion across the whole surface of the SAM pattern due to its overall different color compared to non-SAM samples, but this needed to be verified.

All six patterned samples have shown similar corrosion rates. Once the sonicator was turned on at 70-minute mark, all samples' corrosion rates peaked to their maximum, then slowly started decreasing again. This behavior has two possible explanations, first being the bubble adhesion and the corrosion buffering effect that comes with it. However, this explanation is unreasonable for non-SAM samples as they were both hydrophilic therefore not able to immobilize a gas layer within their roughness grooves according to Cassie-Wenzel theory. When y_0 values of non-SAM samples are compared before and after sonication activation (70-minute mark on Figure 5.4), there was no significant difference

which is a sign of consistent electrolyte contact within the grooves at all times. Therefore, the reduced corrosion rates of hydrophilic surfaces are possibly a result of local alkalization within the roughness geometry and not related to possibly entrapped gas. The corrosion rate peaks observed at the 70-minute mark of both non-SAM samples are possibly an effect of electrolyte agitation causing a pH drop within the grooves which is discussed further in section 5.4.2. Interestingly, y_0 curve for hydrophobic SAM sample had a significant peak as soon as the sonicator was initiated showing parallel behavior to its corresponding corrosion rate curve. This is a good indicator of an adhered gas layer inside the trenches acting as a protective layer as intended. As soon as the sonicator was turned off after 30 seconds, the y_0 value along with corrosion rates started to drop and stabilize at a level which is a sign of regeneration of a stable gas layer.
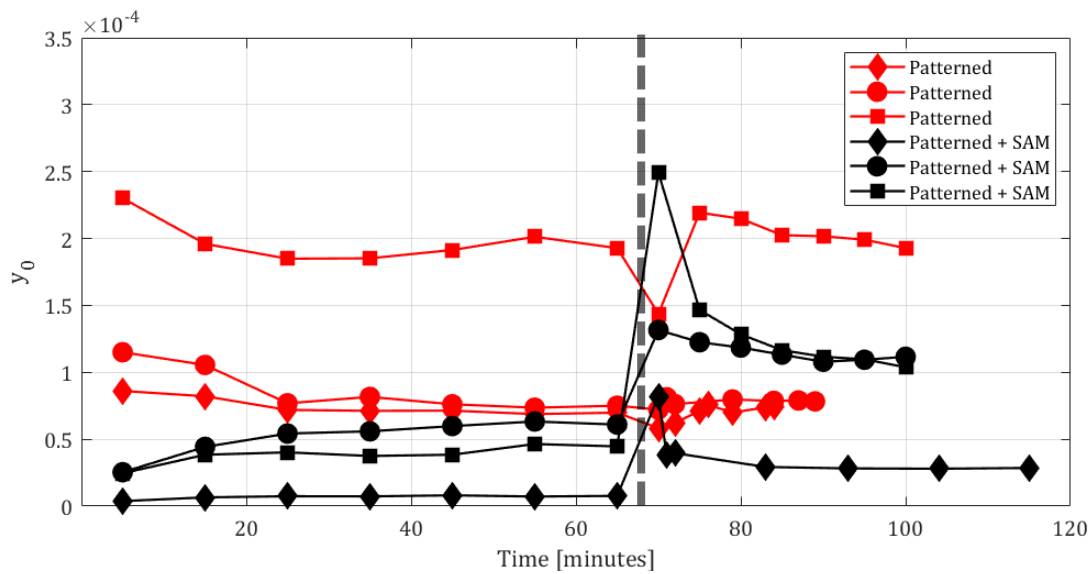
Figure 5.4 The coefficient y_0 that represents the total surface area contact to the electrolyte over time for each sample during EIS experimentations.

The detailed EIS data investigation revealed signs of bubble adhesion on hydrophobic samples. However, prior contact angle measurements (Section 4.3.2) have shown water droplets on hydrophobic patterned samples were in Wenzel state which only allows for a gas

95

www.manaraa.com

blister formation in submerged conditions. While adhered blisters would cause a corrosion inhibiting behavior due to their partial instability, electrolyte infiltration within roughness grooves is likely during submersion. Hence, the possible alkalization effect within roughness grooves on both hydrophilic and hydrophobic samples that would promote oxide layer stabilization in saline is discussed next.

5.4.2 Effect of Alkalinity Near Surfaces

To reiterate section 2.1.2 of Chapter 2, magnesium's corrosion is driven by the stability of formed protective film over the surface. The film is mainly composed of $Mg(OH)_2$ molecules. Stability of this film highly depends on the environment that is in contact. According to Pourbaix diagram for magnesium in aqueous solutions (showing the relation between pH and thermodynamic stability domains), it is not thermodynamically feasible for a $Mg(OH)_2$ layer to exist at pH levels lower than 10.5 as the layer renders unstable and dissolves in the medium [21, 22]. As mentioned earlier in Chapter 2, the dissolution of protective layer causes an increase in the corrosion rate of magnesium. However, in practice, the dissolution rate of the protective layer is slower than the new film formation rate, allowing partial protection against corrosion. This phenomenon is thought to be caused by local alkalinity due to the hydrogen evolution reaction where the reaction byproduct hydroxide ions (OH^-) cause an increase in pH [23]. Local alkalization on polished magnesium surfaces has been experimentally proven by Simaranov et. al [24]. Near the corroding magnesium surface, a pH value of 10 was measured even though the bulk solution was highly acidic at pH 4. Hence, stability of the protective $Mg(OH)_2$ film was promoted by higher pH values in vicinity of the corroding area even though the overall environment in bulk (pH < 10) does not theoretically allow presence of a stable protective film.

Average electrolyte pH for all samples before collecting EIS spectra was approximately 6.2. However, after EIS measurements, pH was measured as 7.1 which is a sign of alkalization that could promote oxide layer's stability. Unfortunately, it was not possible to measure pH levels near or within the surface textures of micropatterned samples at this stage. However, as mentioned above, work done in literature and the behavior of hydrophilic samples in highly corrosive saline solution backed up by EIS data strongly indicate local alkalinity within micro-trenches causing corrosion protection. The increase in corrosion rates when the EIS setup is vibrated with sonicator can be explained with electrolyte agitation within micro-trenches causing a pH drop.

The hydrophilic behavior on untreated patterned surfaces would result in completely electrolyte infiltrated roughness grooves. Due to the high aspect ratio of trench depth profiles (30 μm wide, 40 μm deep between 100 μm plateaus) this is expected to cause a stagnant electrolyte pockets with possibly no circulation. Combined with either laser or wetting induced oxidation on the trench surfaces, pH levels of these electrolyte pockets are expected to consistently stay high relative to bulk solution without external agitation. This will cause passivation of trench walls indefinitely. Similar behavior is possibly partially experienced in SAM hydrophobic roughness grooves since complete gas plastron conditions were not met in submerged state (Section 4.3.2). As a result local alkalinity within grooves is highly likely causing the corrosion inhibition on hydrophilic surfaces and on hydrophobic surfaces we are seeing effects of both alkalinity and gas adhesion according to EIS data interpretation (Figure 5.4) and camera observations (Figure 5.3). These effects could be extending some distance onto the tops of the pillars to increase the range of corrosion protection.

5.5 Conclusion

The corrosion resistance on hydrophilic micro-textures is believed to be caused by increased local alkalinity that comes with hydrogen evolution. Increased alkalinity causes the stability of the oxide layer on the surfaces of micro-grooves. Hydrophilic samples have shown increased corrosion rates when the electrolyte was agitated with sonication. This is taught to be caused by pH drop caused by electrolyte agitation on regions with local alkalization.

The less steep slope of corrosion rate increase of hydrophilic non-SAM samples compared to hydrophobic SAM samples at the moment of sonicator initiation (Figure 5.2) is also an indicator of a different effect than bubble detachment. When the sonicator is turned on, bubbles are detached immediately revealing the substrate and the response in corrosion is observed instantaneously on hydrophobic SAM samples. However, the effects of pH decrease that comes with agitation has a slower effect on hydrophilic non-SAM samples since the dissolution of protective oxide/hydroxide layers in lowered pH environment is not immediate.

On hydrophobic SAM samples, y_0 values of CPE component have shown an increase when the electrolyte is agitated which is a sign of increased electrolyte contact on the substrate. This can only be explained by detached gas layers blocking the electrolyte contact when the solution is not being agitated. As soon as the agitation stops both corrosion rates and the y_0 values have started decreasing then stabilized at a certain level. This effect is also confirmed with visual observations (Figure 5.3). However, since gas bubbles (gas blisters) were not completely contained within roughness grooves in SAM samples, the grooves will experience electrolyte infiltration occasionally until gas blisters are regenerated through

98

hydrogen evolution. This will result in partial corrosion inhibition caused through a combined effect of both alkalinity induced oxide layer stabilization and gas layer buffering.

Chapter 6: Conclusions and Future Work

This dissertation has investigated the corrosion protection of rough hydrophobic surfaces phenomenon which attracts wide interest in literature for different application purposes. The purpose in this case was to create a practical and repeatable method to create hydrophobic surfaces on magnesium for biodegradable medical implant applications while also investigating the exact mechanics behind corrosion protection that comes with hydrophobicity. For this purpose, pure magnesium was chosen for testing due to its highly active degradation characteristics in corrosive environments which can be mitigated further by material science applications (such as alloying and heat treatment) in addition to the method outlined in this research.

The theory of corrosion reduction with hydrophobic rough surfaces rely on entrapment of gas bubbles within roughness grooves. In the case of magnesium corrosion, utilization of this mechanism for corrosion protection attracts interest since degradation of magnesium releases hydrogen gas which in a way renders the process self-regenerative. However, most studies focusing on hydrophobic surfaces rely on surface roughness generation methods such as chemical etching that yield randomized roughness profiles. In order to render repeatability and predictability, laser ablation method was employed to create the micro-structures needed for hydrophobicity and gas entrapment on magnesium. In Chapter 3, a successfully developed method to laser machine magnesium surfaces in order to create any surface roughness profile with pre-determined dimensions based on

100

requirements was documented. With the outcome of this sub-study, hydrophobic surfaces on magnesium were created repeatedly with precision for their corrosion assessment.

In Chapter 4, laser ablated hydrophobic magnesium surfaces' corrosion resistance were tested through submersion tests and electrochemical impedance spectroscopy (EIS). In addition to hydrophobic surfaces, hydrophilic surfaces were also included for controlled testing purposes by skipping the stearic acid modification step on some samples. Through a preliminary submersion test which is practical and requires minimal preparation time, scope of the experiments was narrowed down by picking the most promising micro-pattern type that had the lowest corrosion rate. Compared to polished untreated magnesium surfaces all roughened surfaces have shown improved corrosion protection in all tests. Through visual observation, surface pattern with 100 μm wide square micro-pillars was determined as the most promising micro-pattern for corrosion protection.

Unexpectedly, samples that had no stearic acid modification (which are hydrophilic and expected to have increased corrosion rates according to theory) have also shown similarly improved corrosion resistance. As a first step of investigating the underlying reason behind improved corrosion protection that came with laser micro-patterning, controlled tests were performed through EIS comparing as ablated micro-patterns and micro-patterns that were processed with ASTM procedure that removes the oxide layer induced by laser ablation. Oxide removal process was not as effective on the laser ablated trenches compared to polished sections of the micro-structures due to increased nano-roughness of the trench walls. However, the oxygen content on all surfaces has significantly dropped after oxide removal procedure was done. EIS measurements have shown no significant difference between as ablated and reduced oxide containing micro-patterned

surfaces. As a result, it was concluded oxide layer induced by laser ablation was not hindering corrosion on patterned surfaces. With this information, oxide removal procedure was deemed as an unnecessary step in sample preparation process as it is also introducing contaminants on the substrate which are not desirable for implant applications.

Electrochemical impedance spectroscopy was performed on promising 100 μm wide square pillared patterns with and without stearic acid modification. Oxide removal procedure was skipped during sample preparation, so all patterned samples had oxidation due to laser ablation on surfaces. Similar to preliminary submersion tests, EIS results also have shown reduced corrosion rates that come with micro-patterning. Corrosion rates of polished samples following 1 hour of submersion in EIS electrolyte were 300 mm/year in average and patterned surfaces were degrading with a rate 10 mm/year. There was no significant difference between hydrophobic and hydrophilic identically patterned samples which is also in parallel to what was seen in preliminary submersion tests.

In order to investigate the reason behind the similar corrosion behavior between geometrically identical hydrophilic and hydrophobic patterns, further experimentation was done with a modified EIS setup. The methods and results are documented in Chapter 5. Modified EIS setup included a sonicator that vibrated the system at the end of 1 hour of measurements which removed adhered gas bubbles on sample surfaces. During the initial 1 hour all patterned surfaces regardless of hydrophobic behavior have shown similar corrosion rates to the rates documented in Chapter 4. After 1 hour, sonicator was activated for 30 seconds. All patterned samples' corrosion rates have peaked to their maximum following the sonication and started to drop as measurements proceeded. The increase in corrosion rates in hydrophobic samples were expected since detachment of bubbles would

increase the contact surface area of the electrolyte to the substrate. This was also confirmed with comparing the y_0 values of the fitted CPE element of equivalent circuit. Total rough substrate surface and electrolyte contact area can be qualitatively analyzed by comparing the y_0 values. On hydrophobic surfaces y_0 values have also peaked following the sonicator activation and started to drop down in parallel to their corrosion rate trend. However, on hydrophilic surfaces y_0 values stayed approximately the same at all time points before and after sonication as expected due to complete electrolyte infiltration within roughness grooves with no presence of gas. This was a strong sign of gas layer corrosion buffering on hydrophobic surfaces.

The reason behind corrosion reduction in hydrophilic surfaces was still unclear as all physical corrosion inhibiting barriers (gas or thick oxide layer buffers) were proven to be non-existent through EIS and EDS. However in literature there are multiple documentations for local alkalinity and magnesium corrosion relationship. Oxide layer that is always present on magnesium is not stable at environments with pH levels lower than 10 according to Pourbaix diagrams. The electrolyte pH before EIS testing was measured as 6.2. At the end of EIS measurements electrolyte pH was measured as 7.1. Measurements were done on the bulk solution which means local pH levels could have most probably gone over 10 and caused a corrosion inhibiting effect on all patterned samples. As soon as hydrophilic samples contact the electrolyte oxide layer is generated regardless of pre-existing oxidation on the surfaces. In the light of EIS and EDS data, stabilization of the local oxidation within hydrophilic patterns is the most probable explanation of the improved corrosion resistance.

In conclusion, hydrophobic surface utilization for corrosion reduction in magnesium is possible. The present gas layer within uniformly machined roughness grooves do act as a

103

corrosion barrier. In the cases which the corrosive liquid infiltrates within the grooves, the gas layer can be regenerated due to the hydrogen evolution that comes with magnesium degradation. However, similar corrosion reduction can also be achieved without hydrophobic modifications (stearic acid modification in this case) since micro structures cause high pH zones inside the roughness grooves that allows a stable oxide layer. This is a unique discovery that was not documented in literature before that might result in much more practical and feasible corrosion resisting magnesium surfaces for biodegradable implant applications.

In order to further validate this theory, additional experimentation should be done to eliminate unlikely explanations for the reduced corrosion rates seen on hydrophilic laser ablated patterns. Since laser ablation is a thermal process grain structures of magnesium substrate should be observed in order to confirm there is no phase change was occurring that could change corrosion behavior. In order to confirm local alkalinity within roughness grooves improved EIS tests could be performed using a micro tube that can gather data from micro-cavities.

References

[1]   V. Nutton, *Ancient medicine*: Routledge, 2012.

[2]   J. B. Park and J. D. Bronzino, *Biomaterials: principles and applications*: crc press, 2002.

[3]   J. J. M. a. o. m. Vormann, "Magnesium: nutrition and metabolism," vol. 24, pp. 27-37, 2003.

[4]   L.-D. Hou, Z. Li, Y. Pan, M. Sabir, Y.-F. Zheng, and L. J. F. o. M. S. Li, "A review on biodegradable materials for cardiovascular stent application," vol. 10, pp. 238-259, 2016.

[5]   F. Witte, "Reprint of: The history of biodegradable magnesium implants: A review," *Acta Biomater,* vol. 23 Suppl, pp. S28-40, Sep 2015.

[6]   E. P. DeGarmo, J. T. Black, R. A. Kohser, and B. E. Klamecki, *Materials and process in manufacturing*: Prentice Hall Upper Saddle River, 1997.

[7]   M. P. Staiger, A. M. Pietak, J. Huadmai, and G. J. B. Dias, "Magnesium and its alloys as orthopedic biomaterials: a review," vol. 27, pp. 1728-1734, 2006.

[8]   H. Zreiqat, C. Howlett, A. Zannettino, P. Evans, G. Schulze-Tanzil, C. Knabe*, et al.*, "Mechanisms of magnesium-stimulated adhesion of osteoblastic cells to commonly used orthopaedic implants," vol. 62, pp. 175-184, 2002.

[9]   V. Lespinasse, G. C. FISHER, and J. J. J. o. t. A. M. A. Eisenstaedt, "A practical mechanical method of end-to-end anastomosis of blood-vessels: using absorbable magnesium rings," vol. 55, pp. 1785-1790, 1910.

[10]   M. J. A. o. s. Seelig, "A study of magnesium wire as an absorbable suture and ligature material," vol. 8, pp. 669-680, 1924.

[11]   E. J. S. M. J. McBride, "Magnesium screw and nail transfixion in fractures," vol. 31, pp. 508-514, 1938.

[12]   T. S. Narayanan, I.-S. Park, and M.-H. Lee, *Surface Modification of Magnesium and Its Alloys for Biomedical Applications: Modification and Coating Techniques*: Elsevier, 2015.

[13]   M. Liu, P. J. Uggowitzer, A. V. Nagasekhar, P. Schmutz, M. Easton, G.-L. Song*, et al.*, "Calculated phase diagrams and the corrosion of die-cast Mg–Al alloys," *Corrosion Science,* vol. 51, pp. 602-619, 2009.

[14]   G. Song, A. Atrens, D. St John, X. Wu, and J. Nairn, "The anodic dissolution of magnesium in chloride and sulphate solutions," *Corrosion Science,* vol. 39, pp. 1981-2004, 1997.

[15]   G. L. Song and A. Atrens, "Corrosion Mechanisms of Magnesium Alloys," *Advanced Engineering Materials,* vol. 1, pp. 11-33, 1999.

[16]   D. Panchanathan, "Droplet levitation and underwater plastron restoration using aerophilic surface textures," Massachusetts Institute of Technology, 2018.

[17]   J. H. Nordlien, S. Ono, N. Masuko, and K. Nis,ancioǦlu, "Morphology and Structure of Oxide Films Formed on Magnesium by Exposure to Air and Water," vol. 142, pp. 3320-3322, October 1, 1995 %J Journal of The Electrochemical Society 1995.

[18]   M. Curioni, F. Scenini, T. Monetta, and F. Bellucci, "Correlation between electrochemical impedance measurements and corrosion rate of magnesium investigated by real-time hydrogen measurement and optical imaging," *Electrochimica Acta,* vol. 166, pp. 372-384, 2015.

[19]   G. Song, A. Atrens, D. Stjohn, J. Nairn, and Y. Li, "The electrochemical corrosion of pure magnesium in 1 N NaCl," *Corrosion Science,* vol. 39, pp. 855-875, 1997.

[20]   G. Williams, N. Birbilis, and H. N. McMurray, "The source of hydrogen evolved from a magnesium anode," *Electrochemistry Communications,* vol. 36, pp. 1-5, 2013.

[21]   G. Perrault, "The potential-pH diagram of the magnesium-water system," *Journal of Electroanalytical Chemistry and Interfacial Electrochemistry,* vol. 51, pp. 107-119, 1974.

[22]   M. Pourbaix and J. Burbank, "Atlas D-equilibres electrochimiques," ed: The Electrochemical Society, 1964.

[23]   M.-C. Zhao, M. Liu, G.-L. Song, and A. Atrens, "Influence of pH and chloride ion concentration on the corrosion of Mg alloy ZE41," *Corrosion Science,* vol. 50, pp. 3168-3178, 2008.

[24]   A. Yu Simaranov, I. Sokolova, A. Marshakov, and N. Mikhalovskii, "Stability of oxidation film on magnesium in different pH value," *Protection of Metals,* vol. 27, p. 329, 1992.

[25]   H. Krebs, "Chemical composition of blood plasma and serum," *Annual review of biochemistry,* vol. 19, pp. 409-430, 1950.

[26]   F. Witte, J. Fischer, J. Nellesen, H. A. Crostack, V. Kaese, A. Pisch, *et al.*, "In vitro and in vivo corrosion measurements of magnesium alloys," *Biomaterials,* vol. 27, pp. 1013-8, Mar 2006.

[27]   M. Schinhammer, J. Hofstetter, C. Wegmann, F. Moszner, J. F. Löffler, and P. J. Uggowitzer, "On the Immersion Testing of Degradable Implant Materials in Simulated Body Fluid: Active pH Regulation Using CO2," *Advanced Engineering Materials,* vol. 15, pp. 434-441, 2013.

[28]   Z. Wang, Q. Li, Z. She, F. Chen, L. Li, X. Zhang, *et al.*, "Facile and fast fabrication of superhydrophobic surface on magnesium alloy," *Applied Surface Science,* vol. 271, pp. 182-192, 2013.

[29]   A. Standard, "Standard practice for preparing, cleaning, and evaluating corrosion test specimens," *American Society for Testing and Materials G1-03,* 2011.

[30]   Y. E. Yayoglu, "Corrosion Characteristics of Magnesium under Varying Surface Roughness Conditions," 2016.

[31]   L. Lucas, P. Dale, R. Buchanan, Y. Gill, D. Griffin, and J. Lemons, "In vitro vs in vivo corrosion analyses of two alloys," *Journal of Investigative Surgery,* vol. 4, pp. 13-21, 1991.

[32]   H. Y. S. Mraied, "Effects of Microstructure and Alloy Concentration on the Corrosion and Tribocorrosion Resistance of Al-Mn and WE43 Mg Alloys," 2017.

[33]   T. Ishizaki, Y. Masuda, and M. Sakamoto, "Corrosion resistance and durability of superhydrophobic surface formed on magnesium alloy coated with nanostructured cerium oxide film and fluoroalkylsilane molecules in corrosive NaCl aqueous solution," *Langmuir,* vol. 27, pp. 4780-8, Apr 19 2011.

[34]   G. L. Song, "Corrosion behavior and prevention strategies for magnesium (Mg) alloys," pp. 3-37, 2013.

[35]   G.-L. Song, "Corrosion behavior and prevention strategies for magnesium (Mg) alloys," in *Corrosion prevention of magnesium alloys*, ed: Elsevier, 2013, pp. 3-37.

[36]   J. Meng, W. Sun, Z. Tian, X. Qiu, and D. Zhang, "Corrosion performance of magnesium (Mg) alloys containing rare-earth (RE) elements," in *Corrosion Prevention of Magnesium Alloys*, ed: Elsevier, 2013, pp. 38-60.

[37]   D. Chen, Y. He, H. Tao, Y. Zhang, Y. Jiang, X. Zhang, *et al.*, "Biocompatibility of magnesium-zinc alloy in biodegradable orthopedic implants," vol. 28, pp. 343-348, 2011.

[38] J. Li, Q. Jiang, H. Sun, and Y. Li, "Effect of heat treatment on corrosion behavior of AZ63 magnesium alloy in 3.5 wt.% sodium chloride solution," *Corrosion Science,* vol. 111, pp. 288-301, 2016.

[39] N.-g. WANG, R.-c. WANG, C.-q. PENG, Y. FENG, K. SHI, and H.-x. J. J. o. C. S. U. JIN, "Effect of solid solution treatment on discharge activity of AP65 magnesium alloy anode," vol. 6, 2012.

[40] J. Gray and B. Luan, "Protective coatings on magnesium and its alloys—a critical review," *Journal of alloys and compounds,* vol. 336, pp. 88-113, 2002.

[41] X. B. Chen, M. A. Easton, N. Birbilis, H. Y. Yang, and T. B. Abbott, "Corrosion-resistant coatings for magnesium (Mg) alloys," pp. 282-312, 2013.

[42] J. Waterman, N. Birbilis, G. Dias, T. Woodfield, M. J. C. E. Staiger, Science, and Technology, "Improving in vitro corrosion resistance of biomimetic calcium phosphate coatings for Mg substrates using calcium hydroxide layer," vol. 47, pp. 340-345, 2012.

[43] C. F. Dunne, G. K. Levy, O. Hakimi, E. Aghion, B. Twomey, K. T. J. S. Stanton*, et al.*, "Corrosion behaviour of biodegradable magnesium alloys with hydroxyapatite coatings," vol. 289, pp. 37-44, 2016.

[44] W. F. Ng, M. H. Wong, and F. T. Cheng, "Stearic acid coating on magnesium for enhancing corrosion resistance in Hanks' solution," *Surface and Coatings Technology,* vol. 204, pp. 1823-1830, 2010.

[45] E. J. Falde, S. T. Yohe, Y. L. Colson, and M. W. Grinstaff, "Superhydrophobic materials for biomedical applications," *Biomaterials,* vol. 104, pp. 87-103, Oct 2016.

[46] R. N. Wenzel, "Resistance of solid surfaces to wetting by water," *Industrial & Engineering Chemistry,* vol. 28, pp. 988-994, 1936.

[47] A. Cassie and S. Baxter, "Wettability of porous surfaces," *Transactions of the Faraday society,* vol. 40, pp. 546-551, 1944.

[48] T. J. P. t. o. t. r. s. o. L. Young, "III. An essay on the cohesion of fluids," pp. 65-87, 1805.

[49] R. Poetes, K. Holtzmann, K. Franze, and U. Steiner, "Metastable underwater superhydrophobicity," *Phys Rev Lett,* vol. 105, p. 166104, Oct 15 2010.

[50] R.-D. Schulze, W. Possart, H. Kamusewitz, and C. Bischof, "Young's equilibrium contact angle on rough solid surfaces. Part I. An empirical determination," *Journal of adhesion science and technology,* vol. 3, pp. 39-48, 1989.

[51]   H. Zhao, K. Y. Law, and V. Sambhy, "Fabrication, surface properties, and origin of superoleophobicity for a model textured surface," *Langmuir,* vol. 27, pp. 5927-35, May 17 2011.

[52]   H. Wang, J. Yu, Y. Wu, W. Shao, and X. J. J. o. M. C. A. Xu, "A facile two-step approach to prepare superhydrophobic surfaces on copper substrates," vol. 2, pp. 5010-5017, 2014.

[53]   C. Sun, X.-W. Zhao, Y.-H. Han, and Z.-Z. Gu, "Control of water droplet motion by alteration of roughness gradient on silicon wafer by laser surface treatment," *Thin Solid Films,* vol. 516, pp. 4059-4063, 2008.

[54]   B. H. Luo, P. W. Shum, Z. F. Zhou, and K. Y. Li, "Preparation of hydrophobic surface on steel by patterning using laser ablation process," *Surface and Coatings Technology,* vol. 204, pp. 1180-1185, 2010.

[55]   Y. E. Yayoglu, N. D. Gallant, R. Toomey, and N. B. Crane, "Effects of Laser Ablation Parameters to Pattern High Purity Magnesium Surfaces," in *ASME 2019 International Mechanical Engineering Congress and Exposition*, 2019.

[56]   A. T. Abdulhussein, G. K. Kannarpady, A. B. Wright, A. Ghosh, and A. S. Biris, "Current trend in fabrication of complex morphologically tunable superhydrophobic nano scale surfaces," *Applied Surface Science,* vol. 384, pp. 311-332, 2016.

[57]   B. Bhushan, "Biomimetics: lessons from nature--an overview," *Philos Trans A Math Phys Eng Sci,* vol. 367, pp. 1445-86, Apr 28 2009.

[58]   B. Wu, M. Zhou, J. Li, X. Ye, G. Li, and L. Cai, "Superhydrophobic surfaces fabricated by microstructuring of stainless steel using a femtosecond laser," *Applied Surface Science,* vol. 256, pp. 61-66, 2009.

[59]   M. Ma and R. M. Hill, "Superhydrophobic surfaces," *Current Opinion in Colloid & Interface Science,* vol. 11, pp. 193-202, 2006.

[60]   F. Zhang, L. Zhao, H. Chen, S. Xu, D. G. Evans, and X. Duan, "Corrosion resistance of superhydrophobic layered double hydroxide films on aluminum," *Angew Chem Int Ed Engl,* vol. 47, pp. 2466-9, 2008.

[61]   A. M. A. Mohamed, A. M. Abdullah, and N. A. Younan, "Corrosion behavior of superhydrophobic surfaces: A review," *Arabian Journal of Chemistry,* vol. 8, pp. 749-765, 2015.

[62]   Y. Liu, X. Yin, J. Zhang, Y. Wang, Z. Han, and L. Ren, "Biomimetic hydrophobic surface fabricated by chemical etching method from hierarchically structured magnesium alloy substrate," *Applied Surface Science,* vol. 280, pp. 845-849, 2013.

[63]   M.-H. Han, S.-C. Go, and Y.-H. Ahn, "Fabrication of Superhydrophobic Surface on Magnesium Substrate by Chemical Etching," *Bulletin of the Korean Chemical Society,* vol. 33, pp. 1363-1366, 2012.

[64]   N. B. Dahotre and S. Harimkar, *Laser fabrication and machining of materials*: Springer Science & Business Media, 2008.

[65]   T. Chen, H. Liu, H. Yang, W. Yan, W. Zhu, and H. Liu, "Biomimetic fabrication of robust self-assembly superhydrophobic surfaces with corrosion resistance properties on stainless steel substrate," *RSC Advances,* vol. 6, pp. 43937-43949, 2016.

[66]   U. Trdan, M. Hočevar, and P. Gregorčič, "Transition from superhydrophilic to superhydrophobic state of laser textured stainless steel surface and its effect on corrosion resistance," *Corrosion Science,* vol. 123, pp. 21-26, 2017.

[67]   C. Wang, F. Tang, Q. Li, Y. Zhang, and X. Wang, "Spray-coated superhydrophobic surfaces with wear-resistance, drag-reduction and anti-corrosion properties," *Colloids and Surfaces A: Physicochemical and Engineering Aspects,* vol. 514, pp. 236-242, 2017.

[68]   L. Feng, Y. Zhu, W. Fan, Y. Wang, X. Qiang, and Y. Liu, "Fabrication and corrosion resistance of superhydrophobic magnesium alloy," *Applied Physics A,* vol. 120, pp. 561-570, 2015.

[69]   D. Li, H. Wang, D. Luo, Y. Liu, Z. Han, and L. Ren, "Corrosion resistance controllable of biomimetic superhydrophobic microstructured magnesium alloy by controlled adhesion," *Surface and Coatings Technology,* vol. 347, pp. 173-180, 2018.

[70]   W. Xu, J. Song, J. Sun, Y. Lu, and Z. Yu, "Rapid fabrication of large-area, corrosion-resistant superhydrophobic Mg alloy surfaces," *ACS Appl Mater Interfaces,* vol. 3, pp. 4404-14, Nov 2011.

[71]   G. G. J. T. A. N. Scott, "The evolutionary significance of the osmotic pressure of the blood," vol. 50, pp. 641-663, 1916.

[72]   A. International, "ASTM G102-89 (2010) Standard Practice for Calculation of Corrosion Rates and Related Information from Electrochemical Measurements," *Annual Book of ASTM Standards,* vol. 89, pp. 1-7, 2010.

[73]   M. S. Bobji, S. V. Kumar, A. Asthana, and R. N. Govardhan, "Underwater sustainability of the "Cassie" state of wetting," *Langmuir,* vol. 25, pp. 12120-6, Oct 20 2009.

[74]   Y. E. Yayoglu, N. D. Gallant, R. Toomey, and N. B. Crane, "Effects of Laser Ablation Parameters to Pattern High Purity Magnesium Surfaces," in *ASME 2019 International Mechanical Engineering Congress and Exposition*.

[75]   W. Haiss, P. Raisch, L. Bitsch, R. J. Nichols, X. Xia, J. J. Kelly, *et al.*, "Surface termination and hydrogen bubble adhesion on Si(100) surfaces during anisotropic dissolution in aqueous KOH," *Journal of Electroanalytical Chemistry,* vol. 597, pp. 1-12, 2006.

111

Appendix A: Copyright Permissions

The permission below is for the use of Figure 2.1.

JOHN WILEY AND SONS LICENSE
TERMS AND CONDITIONS

Apr 16, 2020

This Agreement between Yahya E Yayoglu ("You") and John Wiley and Sons ("John Wiley and Sons") consists of your license details and the terms and conditions provided by John Wiley and Sons and Copyright Clearance Center.

License Number	4810980854669
License date	Apr 16, 2020
Licensed Content Publisher	John Wiley and Sons
Licensed Content Publication	Advanced Engineering Materials
Licensed Content Title	Corrosion Mechanisms of Magnesium Alloys
Licensed Content Author	G. L. Song, A. Atrens
Licensed Content Date	Feb 2, 2000
Licensed Content Volume	1
Licensed Content Issue	1
Licensed Content Pages	23
Type of use	Dissertation/Thesis
Requestor type	University/Academic
Format	Electronic
Portion	Figure/table

Number of figures/tables	1
Will you be translating?	No
Title	Laser Micropatterning Effects on Corrosion Resistance of Pure Magnesium Surfaces
Institution name	University of South Florida
Expected presentation date	May 2020
Portions	Fig. 7
Requestor Location	Yahya E Yayoglu 18153 Canal Pointe St TAMPA, FL 33647 United States Attn: Yahya E Yayoglu
Publisher Tax ID	EU826007151
Total	0.00 USD

The permission below is for the use of Figure 2.2.

Licensed Content Date	Jan 28, 2013
Licensed Content Volume	15
Licensed Content Issue	6
Licensed Content Pages	8
Type of use	Dissertation/Thesis
Requestor type	University/Academic
Format	Electronic
Portion	Figure/table
Number of figures/tables	1
Will you be translating?	No
Title	Laser Micropatterning Effects on Corrosion Resistance of Pure Magnesium Surfaces
Institution name	University of South Florida
Expected presentation date	May 2020
Portions	Figure 3
Requestor Location	Yahya E Yayoglu 14511 Prism Circle Apt 208 TAMPA, FL 33613 United States Attn: Yahya E Yayoglu
Publisher Tax ID	EU826007151
Total	0.00 USD

The permission below is for the use of Figure 2.7.

ELSEVIER LICENSE
TERMS AND CONDITIONS

Apr 16, 2020

This Agreement between Yahya E Yayoglu ("You") and Elsevier ("Elsevier") consists of your license details and the terms and conditions provided by Elsevier and Copyright Clearance Center.

License Number	4810990386627
License date	Apr 16, 2020
Licensed Content Publisher	Elsevier
Licensed Content Publication	Corrosion Science
Licensed Content Title	Effect of heat treatment on corrosion behavior of AZ63 magnesium alloy in 3.5wt.% sodium chloride solution
Licensed Content Author	Jiarun Li,Quantong Jiang,Huyuan Sun,Yantao Li
Licensed Content Date	Oct 1, 2016
Licensed Content Volume	111
Licensed Content Issue	n/a
Licensed Content Pages	14
Start Page	288
End Page	301
Type of Use	reuse in a thesis/dissertation
Portion	figures/tables/illustrations
Number of figures/tables/illustrations	1
Format	electronic
Are you the author of this Elsevier article?	No

Will you be translating?	No
Title	Laser Micropatterning Effects on Corrosion Resistance of Pure Magnesium Surfaces
Institution name	University of South Florida
Expected presentation date	May 2020
Portions	Figure 4
Requestor Location	Yahya E Yayoglu 14511 Prism Circle Apt 208 TAMPA, FL 33613 United States Attn: Yahya E Yayoglu
Publisher Tax ID	98-0397604
Total	0.00 USD

The permission below is for the use of Figure 2.8.

ELSEVIER LICENSE
TERMS AND CONDITIONS

Apr 16, 2020

This Agreement between Yahya E Yayoglu ("You") and Elsevier ("Elsevier") consists of your license details and the terms and conditions provided by Elsevier and Copyright Clearance Center.

License Number	4810990589804
License date	Apr 16, 2020
Licensed Content Publisher	Elsevier
Licensed Content Publication	Surface and Coatings Technology
Licensed Content Title	Corrosion behaviour of biodegradable magnesium alloys with hydroxyapatite coatings
Licensed Content Author	Conor F. Dunne,Galit Katarivas Levy,Orly Hakimi,Eli Aghion,Barry Twomey,Kenneth T. Stanton

Licensed Content Date	Mar 15, 2016
Licensed Content Volume	289
Licensed Content Issue	n/a
Licensed Content Pages	8
Start Page	37
End Page	44
Type of Use	reuse in a thesis/dissertation
Portion	figures/tables/illustrations
Number of figures/tables/illustrations	1
Format	electronic
Are you the author of this Elsevier article?	No
Will you be translating?	No
Title	Laser Micropatterning Effects on Corrosion Resistance of Pure Magnesium Surfaces
Institution name	University of South Florida
Expected presentation date	May 2020
Portions	Figure 10
Requestor Location	Yahya E Yayoglu 14511 Prism Circle Apt 208 TAMPA, FL 33613 United States Attn: Yahya E Yayoglu
Publisher Tax ID	98-0397604
Total	0.00 USD

The permission below is for the use of Figure 2.12.

ELSEVIER LICENSE
TERMS AND CONDITIONS

Apr 16, 2020

This Agreement between Yahya E Yayoglu ("You") and Elsevier ("Elsevier") consists of your license details and the terms and conditions provided by Elsevier and Copyright Clearance Center.

License Number	4811011420179
License date	Apr 16, 2020
Licensed Content Publisher	Elsevier
Licensed Content Publication	Thin Solid Films
Licensed Content Title	Control of water droplet motion by alteration of roughness gradient on silicon wafer by laser surface treatment
Licensed Content Author	Cheng Sun,Xiang-Wei Zhao,Yong-Hao Han,Zhong-Ze Gu
Licensed Content Date	Apr 30, 2008
Licensed Content Volume	516
Licensed Content Issue	12
Licensed Content Pages	5
Start Page	4059
End Page	4063
Type of Use	reuse in a thesis/dissertation
Portion	figures/tables/illustrations
Number of figures/tables/illustrations	1
Format	electronic
Are you the author of this Elsevier article?	No

Will you be translating?	No
Title	Laser Micropatterning Effects on Corrosion Resistance of Pure Magnesium Surfaces
Institution name	University of South Florida
Expected presentation date	May 2020
Portions	Figure 7
Requestor Location	Yahya E Yayoglu 14511 Prism Circle Apt 208 TAMPA, FL 33613 United States Attn: Yahya E Yayoglu
Publisher Tax ID	98-0397604
Total	0.00 USD

Appendix B: Micro-textured Sample Names and Definitions

Table B.1 Micro-patterned samples tested in saline solution.

Sample Name	Pillar Width - P [μm]	Trench Width – T [μm]	Trench Depth [μm]
P030-T25-D20	30	25	20
P100-T25-D20	100	25	20
P100-T35-D20	100	35	20
P100-T35-D20-SAM	100	35	20
P100-T35-D30-A	100	35	30
P050-T35-D30	50	35	30
P025-T35-D30	25	35	30
P100-T35-D30-B	100	35	30

Table B.2 Micro-patterned samples tested with EIS.

Sample Name	Pillar Width - P [μm]	Trench Width – T [μm]	Trench Depth [μm]
P100-T35-D30	100	35	30
P100-T30-D40-A	100	30	40
P100-T30-D40 -B	100	30	40
P100-T30-D40 -C	100	30	40
P100-T30-D40-A	100	30	40
P100-T30-D40-B	100	30	40
P100-T30-D40-C	100	30	40
P100-T30-D40 -SAM-A	100	30	40
P100-T30-D40 -SAM-B	100	30	40
P100-T30-D40 -SAM-C	100	30	40

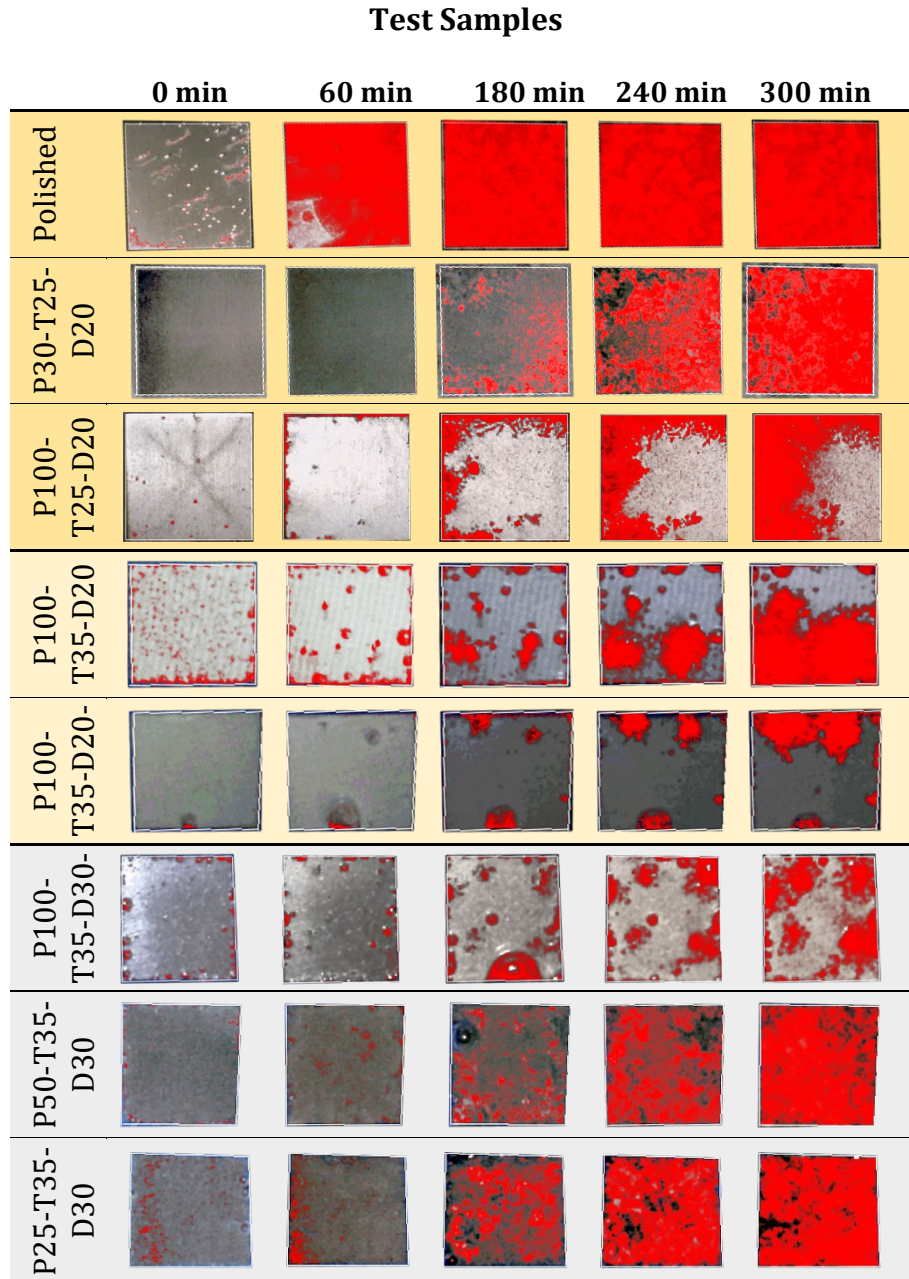# Appendix C: Highlighted Corroded Areas of Submersion

Test Samples

Figure C.1 Marked corroded surface areas of samples in submersion test.

Table C.1 Percentage of the sample surfaces covered with corrosion products as a function of submersion time.

	0 min	**60 min**	**180 min**	**240 min**	**300 min**
Polished	0.88	87.81	98.41	99.40	99.24
P30-T25-D20	0.01	0.05	13.23	39.24	78.24
P100-T25-D20	0.22	3.40	18.80	42.51	56.90
P100-T35-D20	5.29	10.36	13.16	28.38	61.19
P100-T35-D20-SAM	0.16	0.60	5.73	10.71	27.23
P100-T35-D30-A	1.85	2.26	10.35	18.31	34.71
P50-T35-D30	0.86	0.97	10.41	49.95	85.67
P25-T35-D30	1.30	3.45	37.51	82.36	89.94

Appendix D: Corrosion Rates of Polished Samples

Determined by Gravimetric and EIS Methods

Table D.1 Mass loss measurements on gravimetric samples.

	Mass before immersion.	**Mass after immersion for 60 minutes**	**Mass loss rate (g/hour)**
Sample 1	0.313 g	0.274	-0.039 g
Sample 2	0.272 g	0.236	-0.036 g
Sample 3	0.262 g	0.230	-0.032 g

Table D.2 EIS Corrosion rates measured on polished samples 60 minutes after immersion in EIS cell.

	Corrosion Rate (mm/year)	**Corrosion rate (mm/hour)**	**Converted mass loss rate (g/hour)**
Sample 1	266.316	0.030	0.054
Sample 2	191.167	0.022	0.039
Sample 3	218.070	0.025	0.044

Appendix E: SEM Images of Patterned Samples Tested with
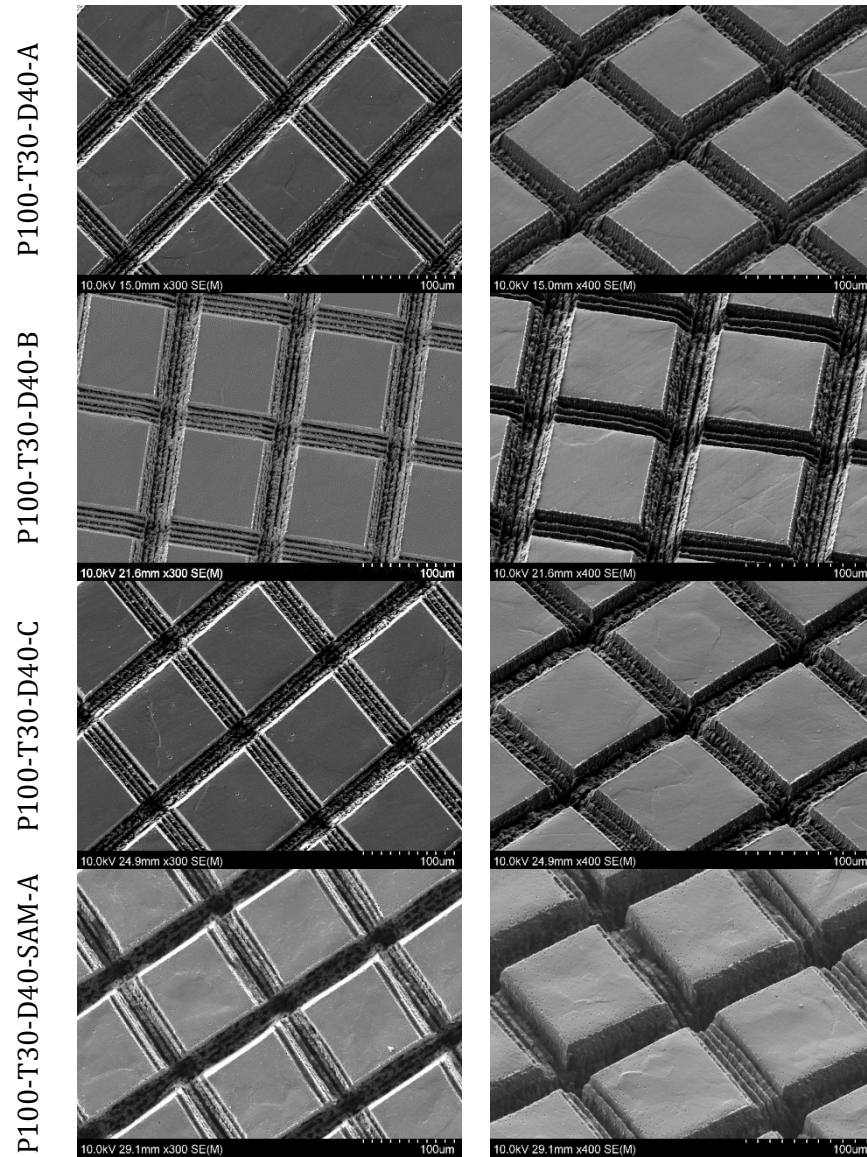
EIS in Chapter 4

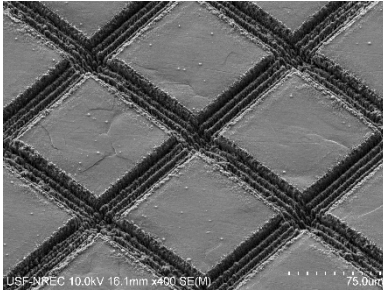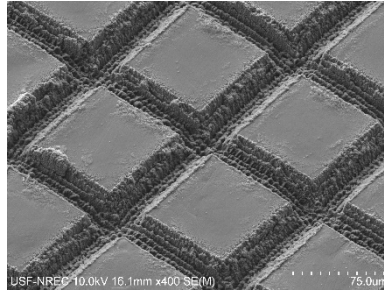Figure E.1 SEM images of samples tested with EIS in Chapter 4.
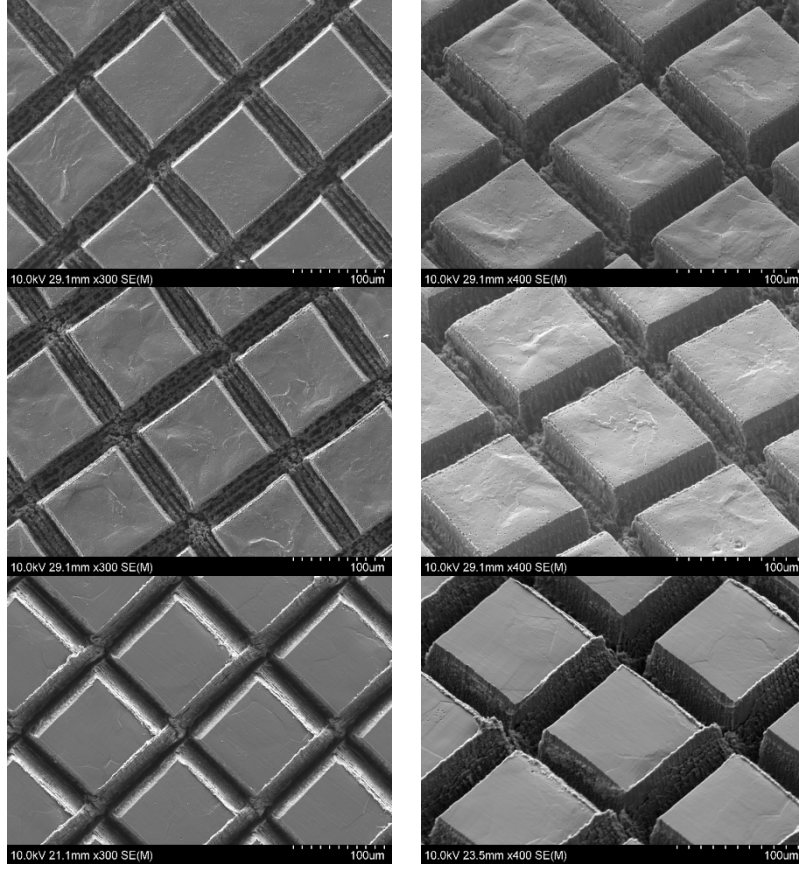
Figure E.2 (Continued)

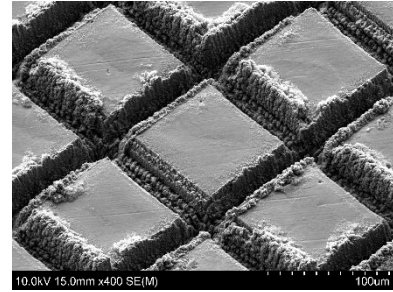# Appendix F: SEM Images of Patterned Samples Tested in

Chapter 5
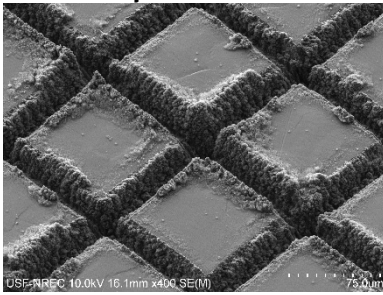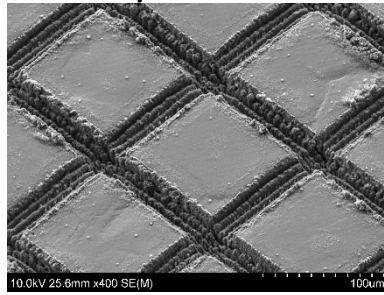

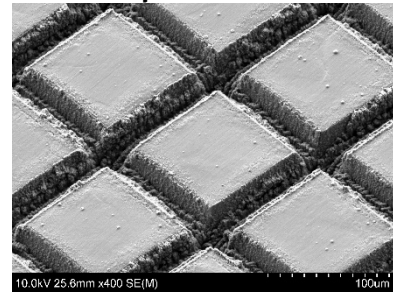**100 μm Pattern 1**   **100 μm Pattern 2**   **100 μm Pattern 3**

100 μm Pattern 4 w/ SAM   **100 μm Pattern 5 w/ SAM**   **100 μm Pattern 6 w/ SAM**

Figure F.1 Samples tested with EIS to verify bubble adhesion's positive effect on corrosion resistance.